Experimental investigation on the effect of dimple-protrusion surfaces in a counter flow heat exchanger

Sakina Tinwala

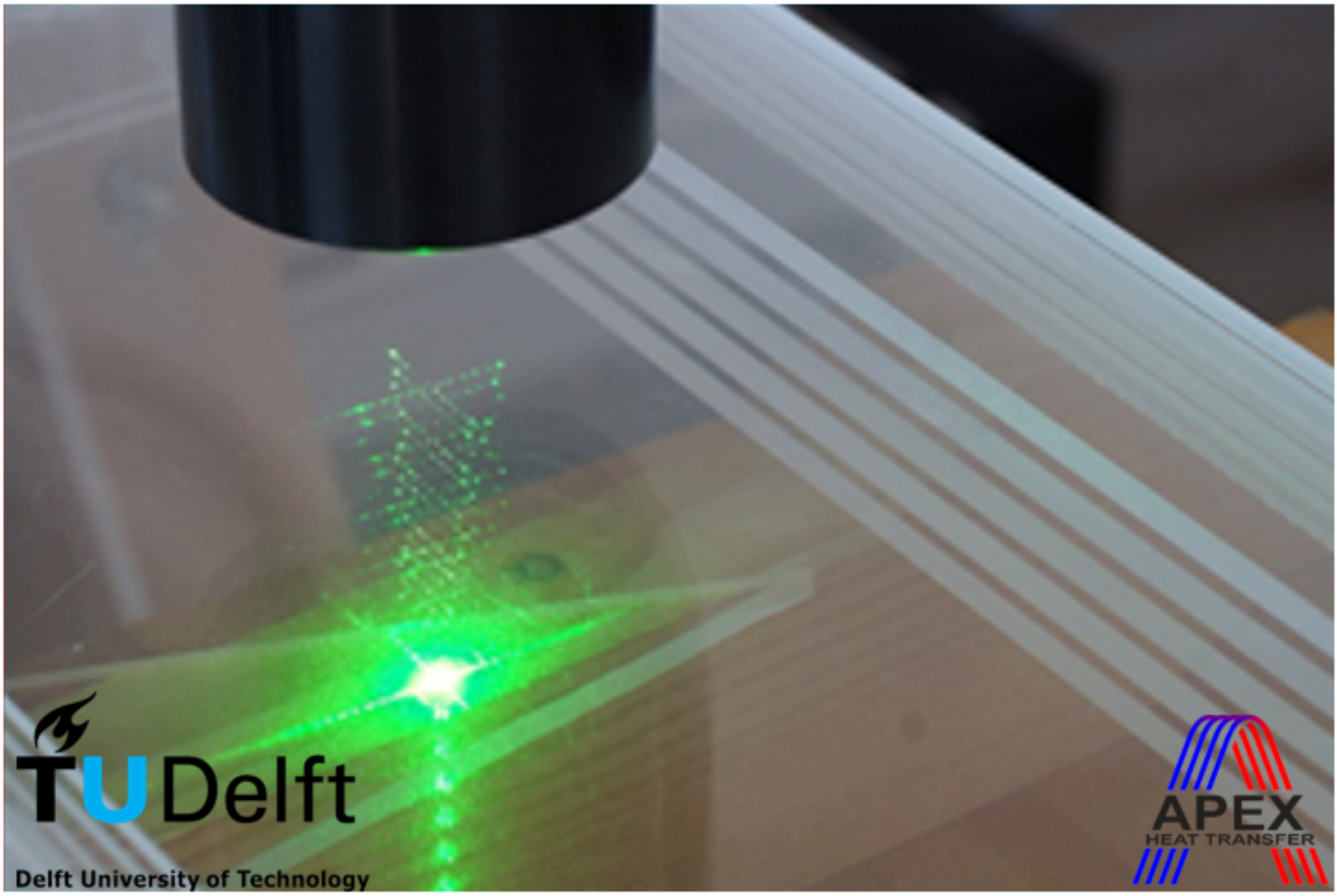

Experimental investigation on the effect of dimple-protrusion surfaces in a counter flow heat exchanger

by

Sakina Tinwala

to obtain the degree of Master of Science
at the Delft University of Technology,
to be defended publicly on Friday May 29, 2020 at 10:00 AM.

P & E report number: 3025

Student number:	4815327	
Project duration:	October 15, 2019 – May 29, 2020	
Thesis committee:	Dr. René Delfos,	TU Delft, supervisor
	Dr. ir. J.W.R. Peeters,	TU Delft, supervisor
	Dr. ir. M.J. Tummers,	TU Delft
	Dr. ir. I. Akkerman,	TU Delft
	Dr. -Ing. Jens Kitzhofer,	APEX Group

Abstract

Flat plate heat exchangers are widely used in industrial and domestic applications. Industrial plate type heat exchangers generally operate in the turbulent flow regime. Although, increase in flow speeds leads to higher transport of heat, it also causes a rise in the pressure loss which is undesirable. Therefore, to combat the problem of high pressure drop, this thesis explores the use of a passive enhancement technique to improve heat transfer. The aim of this thesis is to experimentally investigate the effect of dimple-protrusion surfaces in a counter flow type heat exchanger. The flow behaviour is studied using Laser Doppler Anemometry and the local heat transfer characteristics are investigated with the help of Infrared thermography. The average Nusselt number and friction factor data is compared with those of a flat plate and it is found that the use of dimple-protrusion surfaces provide maximum improvement in the performance of the heat exchanger by 21% in the laminar-to-turbulent transition regime, at Reynolds number $\approx$ 2900.

Sakina Tinwala
Delft, May 2020

Acknowledgement

Foremost, I would like to express my deep gratitude to dr. René Delfos and dr. Jurriaan Peeters, my direct supervisors from TU Delft for their continuous guidance, encouragement and useful critiques during my M.Sc. thesis study. Under their supervision I developed a new perspective for tackling problems and also enriched my research skills. They provided me with sufficient creative freedom to explore on my own while at the same time steered me back on track when I wandered off too far. It was an absolute pleasure to work with them and a privilege to learn from them.

My research would have been impossible without the support of APEX Group. I am profoundly grateful to dr. Jens Kitzhofer to provide me with the opportunity to do my Master thesis with APEX Group. He not only supervised me during the course of my thesis, but also encouraged me and is a source of motivation and inspiration. His support and constant feedback helped me during my experimentation. Moreover, his unconditional faith in my abilities made this experience even more delightful. I thank him for being a part of this journey and walking all the miles with me till the very end. My sincere thanks to Mircea Dinulescu, Laurentiu Moruz, Roelof Schra and the entire team of APEX Group for their constant support, advice and insightful comments.

I acknowledge the contribution of all my peers and friends. At this juncture, I would also like to extend my gratitude to dr. Mark Tummers and dr. Ido Akkerman for taking time off their busy schedules to be a part of my thesis committee.

I am very thankful to Avishek, Anand and Shrinjay who started this journey at TU Delft with me. They were not only present with me during my moments of joy but also at my hardest times. Their encouragement boosted my self-confidence and reassured me of my abilities. I would also like to thank Mihir, Nilay, Neel, Reshma, Debadrita and Sukanya to make me feel at home and organize amazing potlucks.

I feel very fortunate to have Husain in my life. I would like to thank him for his unconditional love, care and support. His trust in my abilities gives me the confidence to perform at my best. Finally, I would like to thank my parents and grand parents for their unconditional love and concern throughout my life. This work would not have been possible without their constant encouragement and support.

Sakina Tinwala
Delft, May 2020

Contents

List of Symbols

Abbreviations

DNS	Direct numerical simulation
IR	Infrared
LDA	Laser Doppler Anemometry
LMTD	Logarithmic mean temperature difference
PF	Performance factor
TLC	Thermochromic liquid crystal

Symbols

α	Aspect ratio of the channel	
ΔT^+	Temperature wall roughness function	
ΔU^+	Momentum wall roughness function	
$\mathcal{P}$	Perimeter of heat transfer	m
ρ	Density of the fluid	kg/m^3
$\underline{f}$	Body force	
$\underline{u}$	Velocity of the fluid	m/s
b	Half channel height	m
c	Chord length of the guiding vanes	m
D_h	Hydraulic diameter	m
f	Darcy friction factor	
k_s	Equivalent sand grain roughness height	m
L_e	Entry length	m
Nu	Nusselt number	
Pr	Prandtl number	
Re	Reynolds number	
s	Distance between two guiding vanes	m
Tu	Turbulence intensity	
ν	Kinematic viscosity of the fluid	m^2/s
A	Cross sectional area	m^2
C_f	Skin friction coefficient	
c_p	Specific heat at constant pressure	J/kg K

g	Heat transfer function	
H	Height of the channel	m
h	Heat transfer coefficient	$W/m^2 K$
k^+	Roughness Reynolds number	
k_f	Thermal conductivity of the fluid	W/m K
L	Length of the channel	m
p	Static pressure	Pa
Q_u	Useful heat loss	J
q	Heat flux	W/m^2
Re^+	Friction similarity function	
St	Stanton number	
T	Temperature	K
U	Overall heat transfer coefficient	$W/m^2 K$
u	U component of the velocity of the fluid	m/s
W	Width of the channel	m
y	Distance from the centerline of the channel	m
z	Distance from the wall of the channel	m

List of Figures

List of Tables

1 Inception

The depletion of fossil fuels and increase in the consumption of energy all over the world is seen to have major economic and environmental consequences. There is an urgent need for the development of efficient thermal energy systems to combat the impact of climate change. To avert the effect of global warming, it is compelling to reduce carbon emissions. The use of efficient heat exchangers in air handling units, heat recovery systems, combustion air pre-heaters and other thermal systems not only significantly lower the heating or cooling costs but also reduce the carbon emissions in the environment. Thus, heat transfer augmentation techniques are essential to improve the thermal performance of heat exchangers.

This chapter consists of four sections. Firstly, the motivation behind this study is described in section 1.1. This is followed by section 1.2 which discusses the state of the art research to improve the heat transfer in various heating devices. Next, the objective and goals of this thesis are described in section 1.3. Thereafter, an overview of the entire thesis is provided in section 1.4 which briefly explains the contents within the subsequent chapters.

1.1. Motivation

Heat exchangers are widely used in industrial and domestic applications including space heating, power plants, reactors, refrigeration systems, petrochemical plants to name a few. The scarcity of resources and increasing urgency for saving energy has prompted the need for efficient heat transfer equipment at low cost to minimize the carbon footprints and reduce harmful emissions.

It is found that the performance factor of flat plate type heat exchangers is poor at low Reynolds number constituting the transitional and early turbulent flow regime. Increase in flow speeds leads to better heat transfer however, it also causes an increase in pressure loss and pumping costs. Pressure drop is a critical design parameter and is desired to be small for various applications like combustion air preheaters, SCR units (DeNOX,SNOX) , gas turbine exhaust recovery, heat recovery for incinerators and furnaces. Thus, a large number of active and passive inserts have been integrated in the heat exchangers to improve its heat transfer performance. Kiran et al. [2014] states that active techniques such as mechanical aids, surface vibration, fluid vibration, electrostatic field, injection and suction are widely used to cause the desired flow modification and improvement in the heat transfer. However, the use of active inserts often requires higher maintenance and external energy supply. Thus, a passive enhancement method such as dimple and protrusion surfaces could provide a high rate of heat transfer with a low pressure drop penalty. This serves as the fundamental motivation for the current study, which aims to sufficiently understand the mechanisms to improve the performance of a plate type heat exchanger.

1.2. State of the art: literature review

A number of active and passive enhancement techniques have been studied extensively in the past couple of decades for a variety of energy systems. However, recently the focus of the research community has shifted towards passive enhancement techniques as these methods are found to be cost

effective and reliable due to the absence of moving parts. Various vortex generators such as grooves, fins, winglets, ribs, twisted tapes, holes, baffles and blocks are commonly found in literature. A few examples of passive enhancement techniques are shown in Figure 1.1. These turbulence promoters are found to improve the heat transfer in heat exchangers, solar thermal energy systems, two phase flow systems, mini/micro energy systems, etc.

Caliskan [2014] performed experiments to investigate the convective heat transfer performance of punched triangular vortex generators (PTVGs) and punched rectangular vortex generators (PRTGs). They found that the thermal enhancement factor $\eta = \frac{Nu/Nu_0}{(f/f_0)^{1/3}}$ for PTVGs was the best with a value of 2.92. Similarly, Promvonge and Skullong [2019] experimentally studied the effect of winglets in a rectangular duct. Furthermore, they showed that the performance of the heat exchanger duct can be improved by reducing pressure drop by punching holes in the winglets. Meanwhile, Rao and Zhang [2019] have experimentally shown that for turbulent flows the Reynolds analogy factor $RAF = \frac{Nu/Nu_0}{(f/f_0)}$ of V-rib dimple surface decreases with an increase in Reynolds number. They conclude that the V rib-dimple with lower rib height shows higher RAF. Although, V-ribs showed a better heat transfer, the RAF was lower than that for pure dimples surfaces.

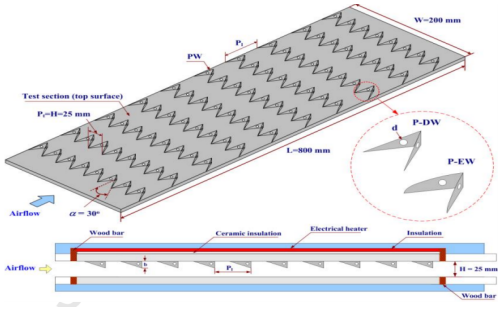

(a) Effect of punched winglets in a rectangular channel flow studied by Promvonge and Skullong [2019].

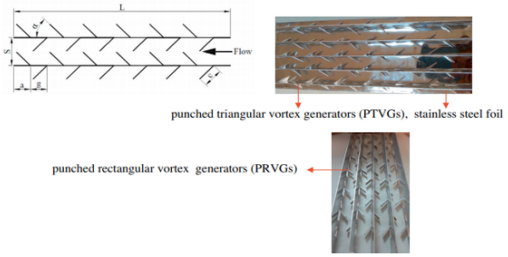

(b) Effect of punched vortex generators in a rectangular channel flow studied by Caliskan [2014].

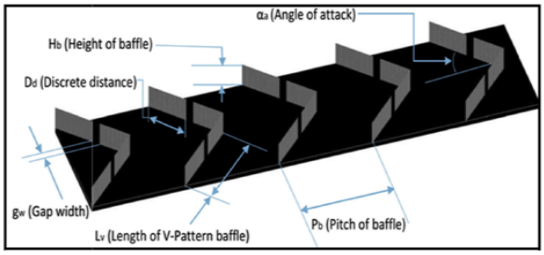

(c) Effect of discretized broken V-pattern baffles studied by Kumar et al. [2017b].

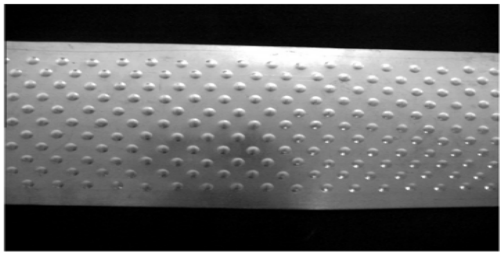

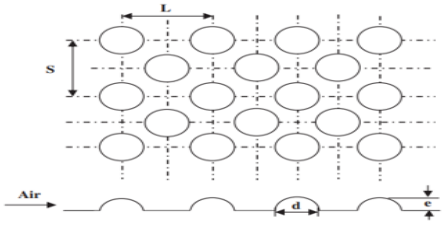

(d) Effect of protruded roughness geometry on absorber plate studied by Bhushan and Singh [2011]

Figure 1.1: Some examples of passive enhancement techniques used to improve the heat transfer performance of a channel flow.

The work of Abdulhameed et al. [2019] compares different baffle geometries aligned along the upper or lower wall of a rectangular duct. Trapezoidal baffles attached on the lower wall were found to

have the best performance with η = 2.26. The performance of discretized V-pattern baffles in solar air channel was investigated by Kumar et al. [2017b]. They examined the effect of geometrical parameters predominantly the gap width and gap location and found the maximum value of the thermal hydraulic performance parameter to be η = 3.14 for relative gap width $g_w/H_b = 1$ and relative baffle height $H_b/H = 0.5$. The experimental model developed by Yadav et al. [2013] provided an opportunity to investigate the effect of protrusions as roughness elements on absorber plate in turbulent flows for solar air heater ducts. Additionally, they developed a correlation to predict the Nusselt number and friction factor with dependency on geometrical parameters. Ma et al. [2010] conducted an experimental investigation on heat transfer enhancement with rectangular blocks as longitudinal vortex generators in water for a 3 mm narrow gap rectangular channel. They showed that not only heat transfer is enhanced but also the transition from laminar to turbulent flow is advanced with the help of rectangular blocks when Reynolds numbers vary between 310 and 4220.

The Nusselt number variations with different inserts have been calculated, both within the domain of experimental analysis and numerical framework. A good understanding of the underlying physics is necessary to match experimental analysis with numerical methods. Experimental and computational model have been developed by Rao et al. [2015, 2012] to determine the pressure loss and heat transfer characteristics in various different shapes of dimple channels. Nazari et al. [2018] conducted a numerical study in STAR CCM to compare the experimental results obtained by Hwang et al. [2008] for a staggered array dimple surface at Re= 10,000 as shown in Figure 1.2. In addition, they performed 10 simulations with staggered, square and triangular arrangements and found the most appreciable improvement for a dimple depth to diameter ratio of h/d = 0.25 at Re = 50,000.

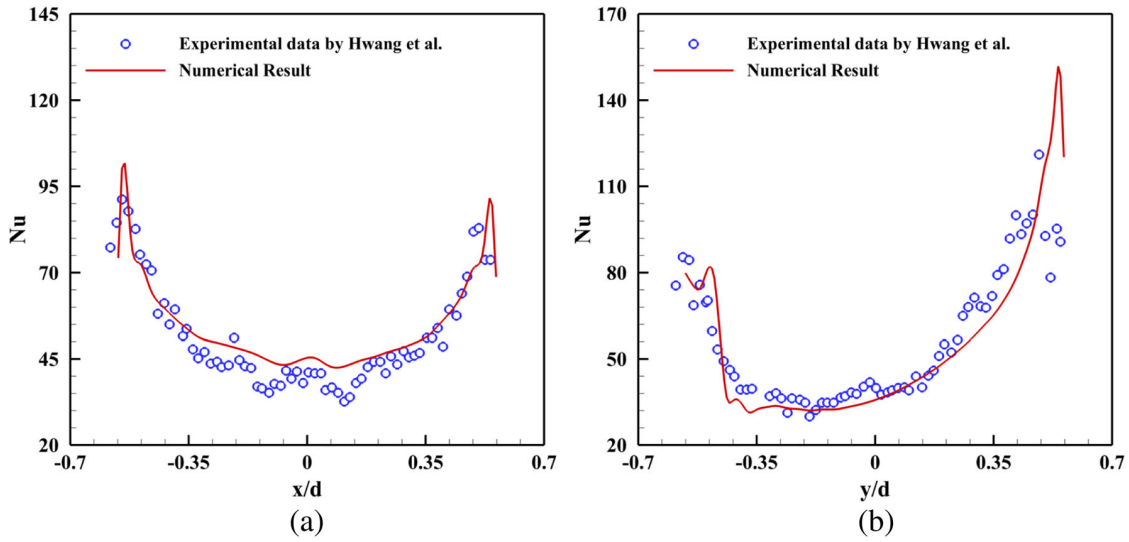

Figure 1.2: Distributed Nusselt number comparison of numerical data by Nazari et al. [2018] and experimental data by Hwang et al. [2008] along (a) span-wise and (b) stream wise direction in the case of d = 15 mm, dimple depth to diameter ratio of 0.25 at Re = 10,000 with staggered arrangement.

Ingole and Shelke [2016] and Rashidi et al. [2019] reviewed the pros and cons of dimpled surfaces in thermal energy systems. In fact, they acknowledged the dimpled surface technology as one of the promising technique to considerably augment the heat transfer rate with a low pressure drop penalty. Chen et al. [2012] conducted a numerical investigation for asymmetrical and symmetrical dimpled surfaces. They suggested that skewing the centre of the dimple to the downstream side can be a feasible way to enhance heat transfer with pressure loss similar to symmetrical dimpled surface. Meanwhile Xie et al. [2013] obtained heat transfer performance for four square channels with different internally protruded dimple geometries. The study was conducted using the $k-\epsilon$ RNG turbulence model with inlet Reynolds numbers ranging from 7500 to 27500. They have shown that internally protruded dimple greatly improve the overall thermal performance when compared with the conventional spherical dimple. Although heat transfer characteristics are ameliorated, it is difficult to fabricate such profiles for large scale production. Later, Chen et al. [2014] conducted a numerical study using Detached Eddy Simulation (DES) to determine the heat transfer characteristics and flow structures over periodically

dimple-protrusion patterned walls in a turbulent flow. An array of spherical dimple-protrusions were arranged on the bottom wall of a heated channel, while the upper wall was smooth and flat. The results obtained for the distribution of normalized Nusselt number Nu/Nu_0 on the bottom wall for different height to hydraulic diameter ratio h/D is shown in Figure 1.3. It was found that the highest local Nusselt number is located at the upstream portion of the protrusions and downstream portion of dimples.

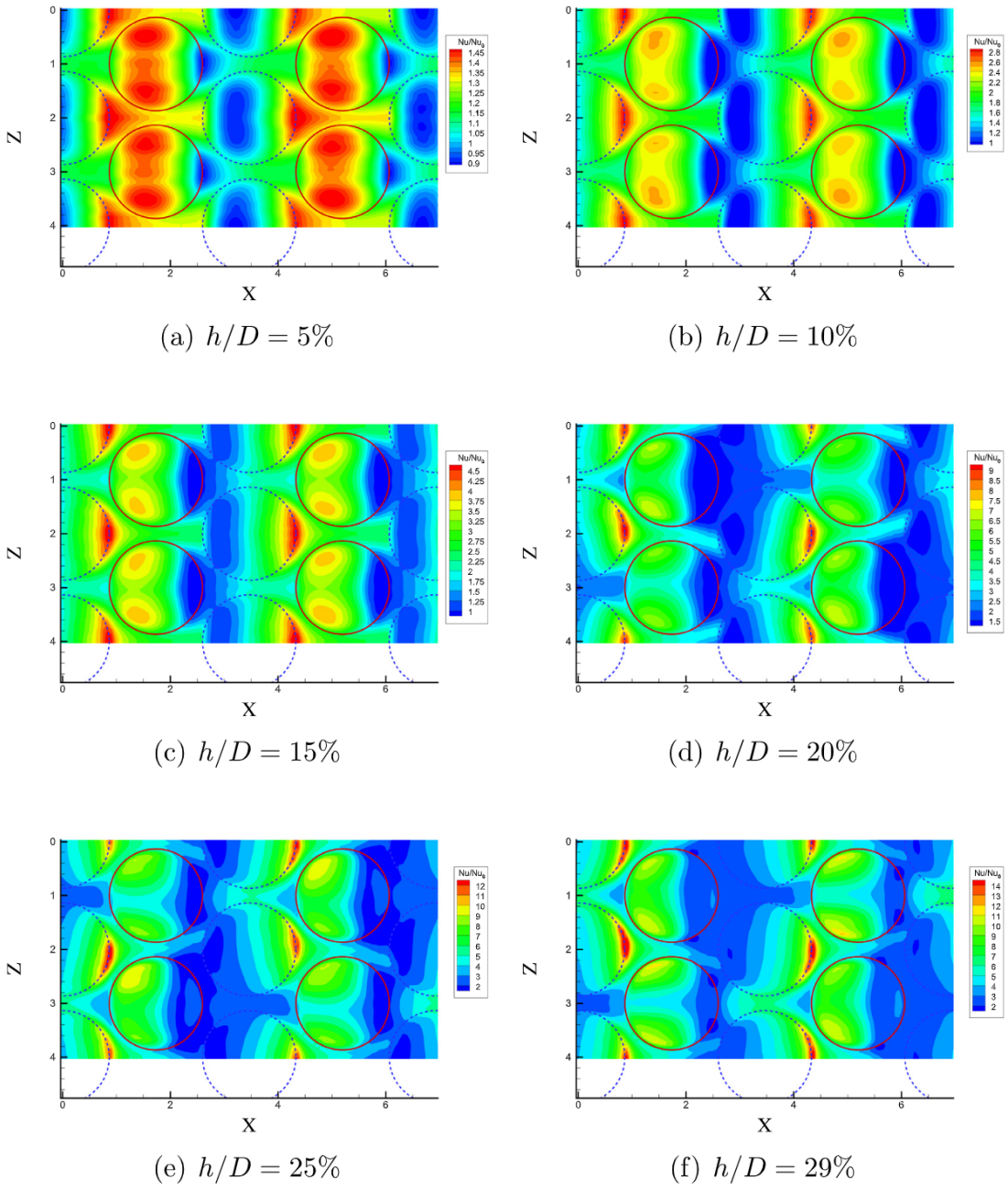

(a) $h/D = 5\%$ (b) $h/D = 10\%$

(c) $h/D = 15\%$ (d) $h/D = 20\%$

(e) $h/D = 25\%$ (f) $h/D = 29\%$

Figure 1.3: Results obtained by Chen et al. [2014] for the distribution of normalized Nusselt number Nu/Nu_0 on the bottom wall for different height to diameter ratio h/D. Dotted blue circle refers to dimples and solid red circle refers to protrusions. The fluid flows from left to right.

Ligrani et al. [2001] and Mahmood et al. [2000] state that the mechanism responsible for the improvement in heat transfer by dimples and protrusions is due to formation of vortices and secondary flows. With the help of smoke flow visualization, Won and Ligrani [2007] showed that for the dimple surface, the flow is separated and a recirculation region is formed in the upstream half of the dimple

which leads to a low heat transfer zone. In the downstream half of the dimple the heat transfer is enhanced due to flow impingement, reattachment, vortex shedding and up wash flow. In the case of the protrusion surface, a high heat transfer zone is formed at the upstream half of the protrusion due to the main flow impingement and formation of vortex legs at both the sides. The flow separates in the downstream half of the protrusion which creates a low heat transfer zone.

Numerous researchers have also aimed to account for the irregular wall roughness in turbulent channel flows. The velocity and temperature profile of surfaces with irregular roughness is computed by calculating the wall roughness functions ΔU^+ and ΔT^+. These functions parametrise the downward shift in velocity and temperature profile scaled with friction velocity and friction temperature respectively. Flack et al. [2016] conducted an experimental investigation to determine the skin friction coefficient for surfaces generated by grit blasting. Furthermore, they suggested a correlation for determining the equivalent sand grain roughness height k_s based upon roughness parameters. The model developed by Thakkar et al. [2018] has shown that DNS of transitionally rough regime flow over 17 industrially relevant rough surfaces yield results close to the results reported by Nikuradse et al. [1950]. However, they have obtained a wide range of the momentum wall roughness functions ΔU^+, despite all samples being scaled to the same roughness height. Thus, making it clear that the roughness effect depends not only on the roughness height but also on the detailed roughness topography. The work of Chedevergne [2018], Aupoix [2015] and Chedevergne and Aupoix [2017] can be used to determine which topological characteristics should be used to predict the wall roughness function ΔU^+. Recently, Peeters and Sandham [2019] showed that DNS of turbulent flow can be used to determine the heat and momentum transfer characteristics with grit blasted roughness in a channel. An estimate for the temperature wall roughness function ΔT^+ is calculated, which is substantially smaller than ΔU^+ at $Pr = 1$. This difference stems from the fact that rough surfaces affect the thermal and velocity fields differently. They also state that the difference between ΔT^+ and ΔU^+ accounts directly for the failure of the Reynolds analogy for fully rough conditions. Thus, it is quite evident that considerable amount of research already exists for surfaces with irregular roughness. However, the current models still need to be extended for surfaces with dimples and protrusions.

The behaviour of flow in a channel has been widely studied using various experimental techniques. Research is mostly conducted using contact sensors and measurement devices. Nevertheless, in the recent years several non contact measurement techniques have also been investigated to improve the accuracy of the measurement. Bhushan and Singh [2011] studied the influence of protrusions on an absorber plate while Kumar et al. [2017a] investigated the effect of V-pattern dimple surfaces in a solar air passage. Both, Bhushan and Singh [2011] and Kumar et al. [2017a] independently proposed correlations for the Nusselt number and friction factor for solar air heater ducts using contact measurement techniques. An experimental and numerical investigation was conducted by Tauscher and Mayinger [1999] for forced convection heat transfer in a rectangular channel with various rib roughened surfaces. They obtained the local heat transfer coefficient using holographic interferometry while the hydrodynamic parameters of the flow were determined using laser doppler velocimetry (LDV).

Singh et al. [2017] has explored the enhancement in heat transfer, for a two pass square duct with ribs and cylindrical dimples, using Transient Liquid Crystal (TLC) thermography. Similarly, Rao and Zhang [2019] used TLC technique to calculate the Reynolds analogy factor for V-rib dimple hybrid structures. The work of Hwang et al. [2008, 2010] provided an opportunity to investigate for different Reynolds number using TLC thermography the local heat transfer performance on dimple walls and protrusion walls. More recently, Chang et al. [2018, 2019] explored the use of infrared thermography to determine the local heat transfer performance for detached S-ribs in a twin pass parallelogram channel. Meanwhile Caliskan et al. [2019] used infrared thermography to study the effect of hexagonal pin fins and cylindrical pin fins in a rectangular channel. They concluded that the best heat transfer performance was obtained by using hexagonal pin fins. Also, Amalfi and Thome [2016a,b] studied the performance of a compact plate type heat exchanger with corrugated plates using infrared (IR) thermography.

However, a multitude of experimental investigations determine the overall Nusselt number by considering the wall temperature as the mean of the temperatures measured at diverse locations on the test surface. These setups do not account for the study of variations in the local Nusselt number. Apart from this, it is noteworthy that most of the current setups make use of smooth channels to hydrodynamically develop the flow and consist of a test section for measurement only after the calming

section. Moreover, these experimental setups make use of electrical heaters which only heats the test section. With such conditions, the flow can not be thermally developed in the measurement domain and these conditions differ from those in an actual heat exchanger. Furthermore, most researchers estimate the bulk fluid temperature as the mean of the inlet and outlet centerline temperature. Such an approach deviates from the true definition of bulk fluid temperature. Also, most of the study in literature deals with measurement in a single rectangular channel. Not much research has been conducted to study the thermal performance in a counter current or parallel flow configuration. These research gaps are a reminder of the fact that the state of the art is still under development and the present study aims to bridge this gap.

1.3. Research objective

This study sheds light on the enhancement of heat transfer characteristics for heat exchangers using dimple and protrusion surfaces. While studies on such systems are available, there is still a lot to be explored, as highlighted by the presence of research gap in section 1.2. This research gap serves as inspiration in defining the goals and objectives of the current study.

One of the main focus of this study is to experimentally determine the local heat transfer coefficients on the dimple-protrusion plates to identify the regions of low and high heat transfer. Thus, one of the goals of this study is to develop Nusselt number and friction factor correlations to predict the performance of a heat exchanger with dimples and protrusions as roughness geometry. Another facet of this study is to determine the onset of transitional and turbulent flow regime for dimple and protrusion plates.

Having established the state of the art and identified the research gap, the following objectives of this study are introduced:

- Design and construct a laboratory scale counter current flow setup.
- Implement measurement techniques to quantitatively determine the local Nusselt number and friction factor.
- Perform analysis to determine the Nusselt number and friction factor for flat plate and dimple-protrusion plate type heat exchanger.
- Identify the onset of transitional and turbulent flow regime for a channel with dimple and protrusion surface.

1.4. Outline of the report

Chapter 2, titled *theoretical background* provides the available theoretical knowledge to understand the underlying physics involved in smooth and rough surfaces. Chapter 3 titled *experimental setup design*, deals with the details for fabrication of the laboratory scale flow setup and an overview of the flow measurement techniques. Chapter 4 provides the methodology for data reduction. Chapter 5 presents the validation of the experimental setup and explicates the performance of the dimple and protrusion surfaces for a heat exchanger. Chapter 6 consolidates the *conclusions* derived from the present work, in an endeavour to achieve the research objectives. Lastly, chapter 7 offers an *outlook* and future recommendations that can be undertaken in this line of research.

2

Theoretical background

This chapter lays down the physics governing the heat transfer for a heat exchanger with counter flow configuration. The theory as described in section 2.1 and 2.3 offers insight into determination of the friction factor and the Nusselt number for fully developed laminar and turbulent flows in a smooth channel. While section 2.2 and 2.4 discusses the momentum and heat transfer for rough channels respectively.

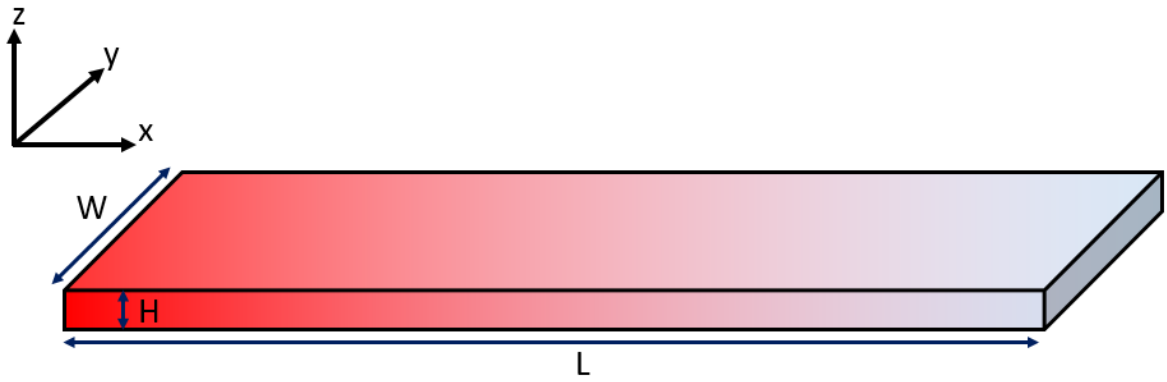

Figure 2.1: Nomenclature used for the experimental channel.

Figure 2.1 shows the nomenclature used for the experimental channel. The x axis is aligned with the stream-wise direction of the flow, the y axis is aligned with the span wise direction of the flow and the z axis is aligned with the height of the channel.

2.1. Momentum transfer in smooth ducts

For fully developed laminar flow between parallel plates, the velocity profile can be determined from the force balance on an elemental control volume of the fluid of unit depth in the y direction as shown in Figure 2.2.

Using the force balance for an infinitesimal control volume with the origin at the centre of the channel and in the limit of $\Delta x, \Delta z \rightarrow 0$, it is found that

$$\mu \frac{d^2u}{dz^2} = \frac{dp}{dx} \tag{2.1}$$

where u is the u-component of velocity, μ is the dynamic viscosity of the fluid and p is the pressure inside the channel. Integrating equation 2.1 with symmetry boundary condition at the centerline $\frac{du}{dz} = 0$

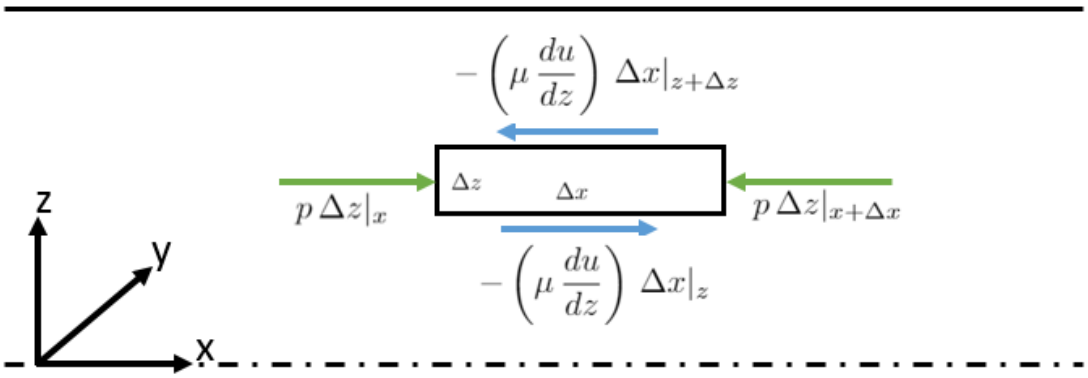

Figure 2.2: Force balance on a fluid element for fully developed laminar flow in a channel.

at $z = 0$ and no slip boundary condition at the wall $u = 0$ at $z = H/2$ gives the velocity profile as shown in equation. 2.2

$$u = \frac{H^2}{8\mu}\left[-\frac{dp}{dx}\right]\left[1 - \left(\frac{z}{H/2}\right)^2\right] \tag{2.2}$$

where, H refers to the channel depth and z is the distance from the centerline of the channel.

Bulk velocity

Since the velocity profile is symmetrical, the bulk velocity can be determined as $u_b = \frac{2}{H}\int_0^{H/2} u dz$. Thereby, the bulk velocity can be related to the velocity at any point by equation. 2.3

$$\frac{u}{u_b} = \frac{3}{2}\left[1 - \left(\frac{z}{H/2}\right)^2\right] \tag{2.3}$$

Friction factor

Thus, the theoretical Darcy friction factor (f) can be calculated in terms of the hydraulic diameter $D_h = 4A/\mathcal{P} \approx 2H$ as shown in equation 2.4 where A is the area and $\mathcal{P}$ is the perimeter of the flow in the channel.

$$f = \frac{(-dp/dx)\,D_h}{\frac{1}{2}\rho\, u_b^2} = \frac{3\mu u_b}{(H/2)^2}\frac{D_h}{\frac{1}{2}\rho\, u_b^2} = \frac{96\mu}{\rho\, u_b\, D_h} = \frac{96}{Re} \tag{2.4}$$

For fully developed turbulent duct flows, Darcy friction factor can be calculated using the empirical correlations based on Reynolds number (Re), developed by Blasius and Petukhov as stated in Mills [1999].

$$\text{Blasius equation} \quad f = 0.316\, Re^{-0.25} \qquad Re \leqslant 10^5 \tag{2.5}$$

$$\text{Petukhov equation} \quad f = (0.790 \ln Re - 1.64)^{-2} \qquad 3000 \leqslant Re \leqslant 5 \times 10^6 \tag{2.6}$$

In addition, Troniewski and Ulbrich [1984] numerically studied the Darcy friction factor for a single phase flow in a rectangular channel with aspect ratio α and suggested equation 2.7 and equation 2.8 to calculate the friction factor in fully developed laminar and turbulent flow respectively.

$$f = \frac{64}{Re^*} \qquad \text{where, } Re^* = \frac{Re}{(2\,\alpha)^{0.16}} \tag{2.7}$$

$$f = 0.3164\, Re^{*-0.25} \qquad Re > 2100 \tag{2.8}$$

2.2. Momentum transfer in rough ducts

Mills [1999] states that surface roughness has little effect on skin friction and heat transfer in laminar flows and this effect is more significant in the turbulent flow regime. However, the effect of surface roughness should be accounted if the mean roughness height is greater than the viscous sub layer. Having discussed the momentum transfer of a fluid in a smooth duct in section 2.1, it is noteworthy to illustrate the momentum transfer in rough ducts. Therefore, theoretical approaches to the problem of momentum transfer in rough ducts are based on similarity considerations and momentum wall roughness function.

2.2.1. Friction similarity law

The friction similarity law is proposed by Nikuradse et al. [1950] for geometrically similar close-packed sand grain roughness surface represented by a single length parameter k which is the height of the surface roughness. The basic assumptions for the friction similarity law is the principle of Reynolds number similarity and law of the wall similarity. The first postulate implies, that for turbulent flow in the region away from the immediate vicinity of the wall the effect of viscosity is negligible on the mean flow. The second postulate states the existence of a region close to the wall where the velocity distribution exclusively depends on the local conditions. Thus, combining the above mentioned assumptions gives the velocity distribution as shown in equation. 2.9

$$u^+ = \frac{u}{u_\tau} = 2.5 \ln\left(\frac{z}{k}\right) + Re^+\,(k^+) \tag{2.9}$$

where u is the u-component of velocity, u_τ is the friction velocity, z is the distance from the wall, Re^+ is the roughness function and k is the surface roughness. Based on this analysis, Nikuradse et al. [1950] developed the friction similarity law as shown in equation. 2.10

$$\sqrt{\frac{2}{C_f}} = -2.5 \ln\left(\frac{2\,k}{D_h}\right) + Re^+\,(k^+) - 3.75 \tag{2.10}$$

where, C_f is the skin friction coefficient and can be computed by the Darcy friction factor as $C_f = \frac{f}{4}$. The roughness Reynolds number $k^+ = \frac{k\,u_\tau}{\nu}$ can be identified as $k^+ = Re\sqrt{\frac{C_f}{2}}\frac{k}{D_h}$ and $Re^+\,(k^+)$ is a general function determined empirically for each type of geometrically similar roughness. Figure 2.3 shows the experimental results by Dipprey and Sabersky [1963] and Ahn and Son [2002] for roughened tubes and ducts respectively.

2.2.2. Momentum wall roughness function

For turbulent forced convective flows, surface roughness is found to increase the drag force on the wall when compared to smooth wall and is often evaluated by the momentum wall roughness function Δu^+. This quantity corresponds to the retardation of the mean stream wise flow for a rough wall when compared with a smooth wall.

Nikuradse et al. [1950] pointed out that above the roughness sub-layer the logarithmic law is shifted and is represented by equation. 2.11

$$u^+ = \frac{1}{\kappa_m}\ln z^+ + A_m - \Delta u^+ \tag{2.11}$$

where $\kappa_m \approx 0.4$ is the von Karman constant and $z^+ = \frac{z\,u_\tau}{\nu}$. Flack et al. [2016] and MacDonald et al. [2019] state that, at matched friction Reynolds number $Re_\tau = Re_H\,(C_f)^{1/2}$, the momentum wall roughness function Δu^+ is related to skin friction coefficients of smooth and rough wall.

$$\Delta u^+ = \sqrt{\frac{2}{C_f}}_{smooth} - \sqrt{\frac{2}{C_f}}_{rough} \tag{2.12}$$

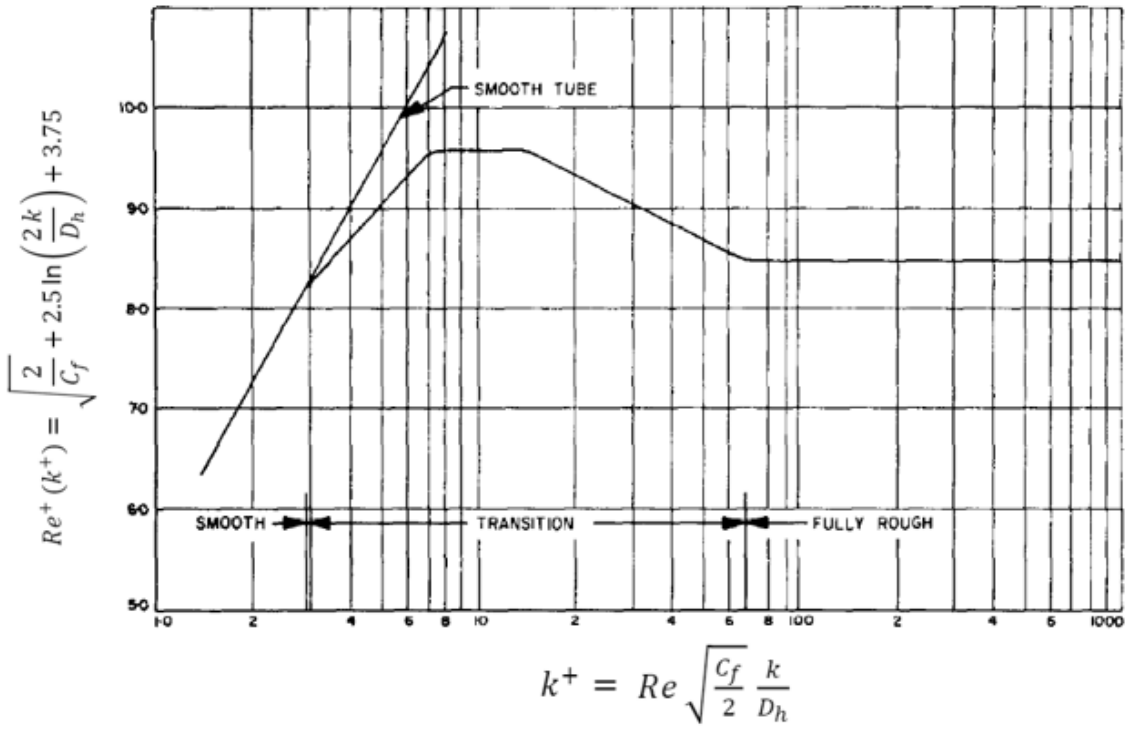

(a) Friction similarity function reproduced by Dipprey and Sabersky [1963] for Nikuradse's close packed sand grain roughness.

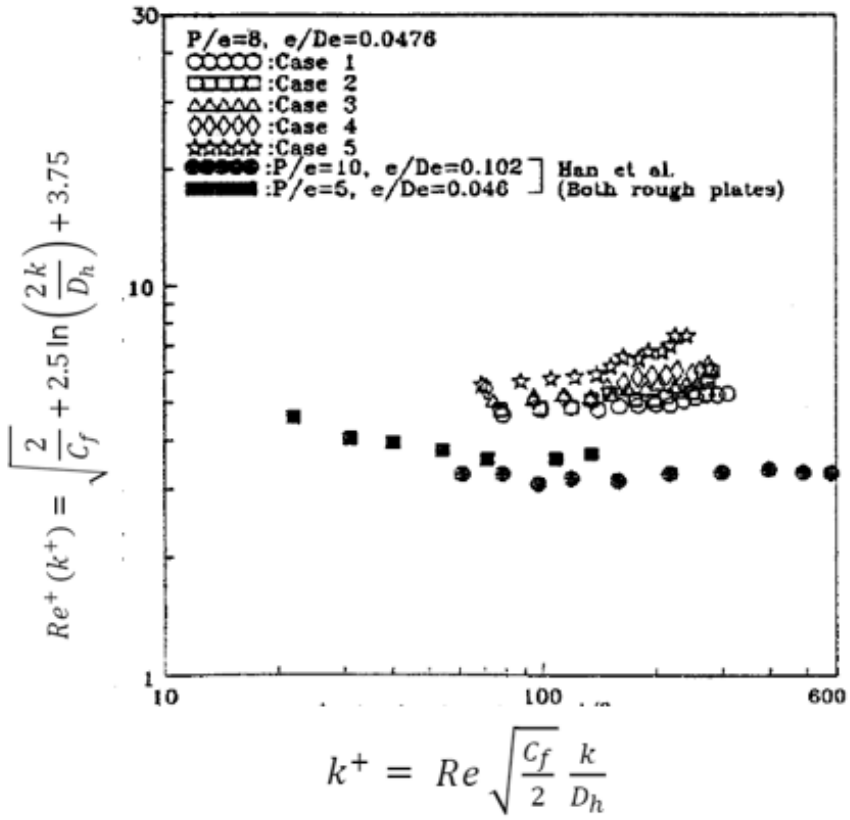

(b) Friction similarity function for rib roughened duct experiments conducted by Ahn and Son [2002].

Figure 2.3: Friction similarity law for round tubes and rectangular channels.

MacDonald et al. [2019] also expresses the relation between the bulk velocity and the skin friction coefficient as shown in equation. 2.13

$$C_f = \frac{2}{u_b^{+2}} \tag{2.13}$$

$$\text{where} \quad u_b^+ = \frac{1}{H}\int_0^H u^+ dz \tag{2.14}$$

2.3. Heat transfer in smooth ducts

The temperature profile for a fully developed laminar flow can be derived using the steady state energy balance on an fluid element as shown in Figure 2.4.

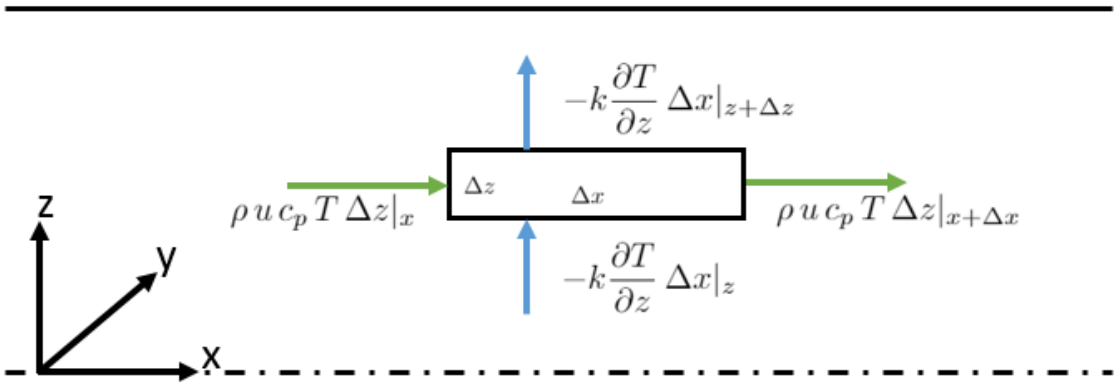

Figure 2.4: The first law of thermodynamics applied to an elemental control volume for fully developed heat transfer in a channel.

In the limit of $\Delta x, \Delta z \to 0$, the fist law of thermodynamics on an elemental control volume can be written as:

$$\rho\, u\, c_p \frac{\partial T}{\partial x} = k\frac{\partial^2 T}{\partial z^2} \tag{2.15}$$

where, ρ is the density of the fluid, c_p is the specific heat of the fluid at constant pressure and T is the temperature.

Also, the energy balance for the channel with heat flux q applied on the surface and with unit depth in the y direction and length Δx can be written as:

$$2\, q\, \Delta x = \rho\, u_b\, c_p\, H\, T_b|_{x+\Delta x} - \rho\, u_b\, c_p\, H\, T_b|_x \tag{2.16}$$

For fully developed flow conditions and in the limit $\Delta x \to 0$ and $T - T_b = \mathcal{Y}(z)$, equation 2.16 can be written as:

$$\frac{2\, q}{\rho\, u_b\, c_p\, H} = \frac{dT_b}{dx} = \frac{\partial T}{\partial x} \tag{2.17}$$

Thus, substituting equation 2.3 and 2.17 in equation 2.15 gives the temperature profile for fully developed laminar flow regime. Integrating with the boundary conditions $\frac{d(T-T_b)}{dz} = 0$ at $z = 0$ and $T = T_s$ at $z = H/2$ gives the temperature profile as follows:

$$T = T_s + \frac{q\, H}{2\, k}\left[-\frac{5}{8} + \frac{3}{4}\left(\frac{z}{H/2}\right)^2 - \frac{1}{8}\left(\frac{z}{H/2}\right)^4\right] \tag{2.18}$$

where, q is the heat flux on the surface of the channel, k is the thermal conductivity of the fluid and z is the distance from the centerline of the channel.

Bulk temperature

The bulk fluid temperature can be determined using the velocity and temperature profile as shown below:

$$T_b = \frac{\int_0^H u\,T dz}{H\,u_b} = T_s - \frac{17}{70}\frac{q\,H}{k} \tag{2.19}$$

Convective heat transfer coefficient

The convective heat transfer coefficient can be computed from Newton's law of cooling as:

$$h = \frac{q}{T_b - T_s} = \frac{70}{17}\frac{k}{H} \tag{2.20}$$

Nusselt number

The Nusselt number is defined as the ratio of convection heat transfer to fluid conduction heat transfer under the same conditions and can be represented as:

$$Nu = \frac{h\,D_h}{k} \tag{2.21}$$

Thus, for fully developed laminar flow between parallel plates, the theoretical Nusselt number is computed as:

$$Nu = \frac{h\,(2H)}{k} = \frac{140}{17} = 8.24$$

Mills [1999] states that in the case of laminar flows the thermal boundary layer extends up to the centerline of a channel and its thickness is independent of the velocity. Thus the heat transfer coefficient has a constant value. Whereas, in the case of turbulent flows an increase in velocity produces vigorous turbulent mixing in the core of the flow resulting in thinning of the viscous sub-layer adjacent to the wall which leads to an increase in the heat transfer coefficient.

For fully developed turbulent duct flows, Nusselt number can be calculated using the empirical correlations of Dittus-Boelter and Gnielinski.

Dittus-Boelter equation $$Nu = 0.023\,Re^{0.8}\,Pr^n \qquad Re \geqslant 10^4 \tag{2.22}$$

where, n = 0.4 for heating when $T_s > T_b$ and n = 0.3 for cooling when $T_s < T_b$.

Gnielinski equation $$Nu = \frac{(f/8)\,(Re - 1000)\,Pr}{1 + 12.7\,(f/8)^{1/2}\,(Pr^{2/3} - 1)} \qquad 3000 \leqslant Re \leqslant 10^6 \tag{2.23}$$

2.4. Heat transfer in rough ducts

Akin to the analysis of momentum transfer in rough ducts as described in section 2.2, this section discusses the heat transfer similarity law and the equivalence of Stanton number with the temperature wall roughness function ΔT^+.

2.4.1. Heat transfer similarity law

Analogous to friction similarity law, Dipprey and Sabersky [1963] developed the heat transfer similarity law for smooth as well as rough round tubes subjected to the following considerations:

- Fully turbulent steady pipe flow (Re > 2000).
- Hydro dynamically and thermally fully developed flow.
- Constant fluid properties.

- Surface roughness patterns statistically independent of circumferential or axial positions.
- Roughness patterns are statistically geometrically similar from tube to tube with only a geometrical scale factor being different.
- Constant heat transfer rate at the surface.

Keeping in mind the above mentioned assumptions, the heat transfer similarity law can be written as shown in equation 2.24:

$$\frac{\frac{C_f}{2\,St} - 1}{\sqrt{\frac{C_f}{2}}} + Re^+ = g\,(k^+, Pr) \tag{2.24}$$

where St is the Stanton number and can be represented as the ratio of Nusselt number to Reynolds number and Prandtl number $St = \frac{Nu}{Re\,Pr}$, Pr is the Prandtl number $Pr = 0.7$ and g is the heat transfer function. Figure 2.24 shows the experimental results obtained by Dipprey and Sabersky [1963] and Ahn and Son [2002] for roughened round tubes and rib roughened rectangular ducts respectively.

2.4.2. Temperature wall roughness function

Similar to the velocity profile, the temperature profile for forced convection flows over a smooth surface exhibits a logarithmic dependence away from the wall. Surface roughness is found to enhance the heat transfer through the wall, thereby resulting in a downward temperature shift in the logarithmic temperature profile. Therefore, the temperature profile can be expressed in terms of the temperature wall roughness function as shown in equation. 2.25

$$\frac{T - T_s}{T_\tau} = \frac{1}{\kappa_\theta} \ln z^+ + A_\theta - \Delta T^+ \tag{2.25}$$

where $\kappa_\theta \approx 0.46$, A_θ is the smooth wall offset and the temperature is relative to the wall temperature which is then normalized by the friction temperature $T_\tau = \frac{q}{\rho\, c_p\, u_\tau}$. Peeters and Sandham [2019] showed that the heat transfer analogue to skin friction coefficient, Stanton number can be expressed as $St = \frac{\sqrt{C_f/2}}{T_b^+}$. Stanton number can also be written in an equivalent form, $St = \frac{1}{u_b^+\, T_b^+}$ as shown by MacDonald et al. [2019]. When the Stanton number is defined using the bulk temperature of the fluid, the temperature wall roughness is expressed as:

$$\Delta T^+ = \sqrt{\frac{C_f}{2}}_{smooth} \left(\frac{1}{St_{smooth}} - \frac{1}{\kappa_m\, \kappa_\theta} \right) - \sqrt{\frac{C_f}{2}}_{rough} \left(\frac{1}{St_{rough}} - \frac{1}{\kappa_m\, \kappa_\theta} \right) \tag{2.26}$$

Instead when the Stanton number is defined using the arithmetic mean temperatures the temperature wall roughness function can be estimated as presented by Aupoix [2015] in equation. 2.27

$$\Delta T^+ = \frac{\sqrt{\frac{C_f}{2}}}{St}_{smooth} - \frac{\sqrt{\frac{C_f}{2}}}{St}_{rough} \qquad \text{with } St = \frac{-q}{\rho\, u_{mean}\, c_p\, (T_s - T_c)} \tag{2.27}$$

Therefore, the Stanton number for rough surfaces can be estimated if the temperature wall function from the temperature profiles and the skin friction coefficient is known for smooth and rough surfaces.

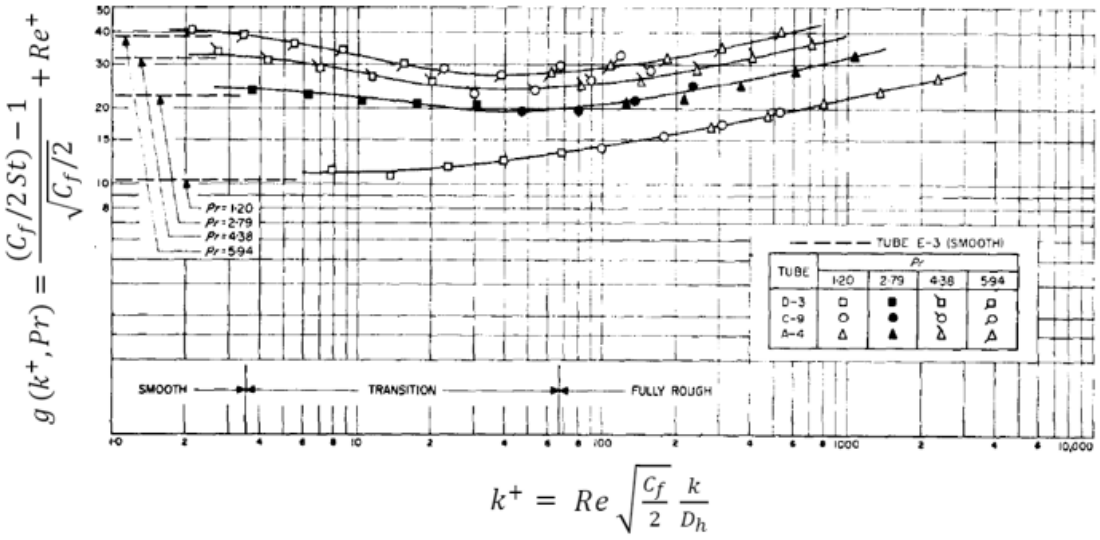

(a) Heat transfer function for the experimental results obtained by Dipprey and Sabersky [1963] for round roughened tubes.

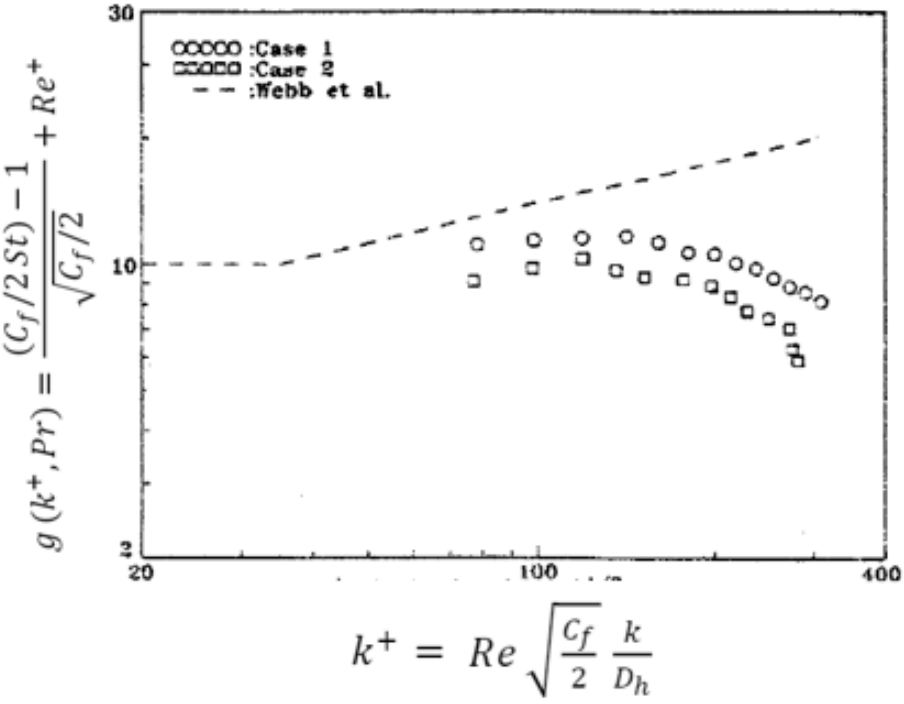

(b) Heat transfer function for the experimental results obtained by Ahn and Son [2002] for rib roughened rectangular duct.

Figure 2.5: Heat transfer similarity law for round tubes and rectangular channels.

Concluding Remarks

This chapter has laid down the theory governing the momentum and heat transfer in smooth and rough channel flows. An analytical solution is derived to determine the Darcy friction factor and the Nusselt number for fully developed laminar flow between parallel plates. On the other hand, experimental correlations are provided to estimate the Darcy friction factor and the Nusselt number for fully developed turbulent flow. Having established the correlations for smooth channels, a brief discussion is provided on the friction similarity law and the heat transfer similarity law based on the roughness Reynolds number for rough ducts. In case of turbulent forced convective flows, the introduction of roughness

leads to reduction in the flow velocity. This shift in velocity is known as the momentum wall roughness function Δu^+ and is related to the skin friction coefficient for smooth and rough walls. Similarly, a downward shift is observed in the temperature logarithmic profile. This shift is called the temperature wall roughness function ΔT^+ which depends on the Stanton number and skin friction coefficient for smooth and rough walls.

3

Experimental setup design

Having defined the research objective and the theoretical background in the previous chapters, the current chapter begins with an overview of the experimental setup in section 3.1. Next, the calibration process of the pressure transducers and thermocouples is explained in section 3.2. It is followed by a brief discussion on two non contact measurement techniques, namely Laser Doppler Anemometry (LDA) and Infrared thermography (IRT) in section 3.3. Finally, section 3.4 describes the procedure followed to conduct the experiments.

3.1. Overview of the experimental setup

The experiments were conducted at the Research and Development department of APEX Group. The schematic and actual experimental facility for the measurement of heat transfer performance is shown in Figure 3.1 and 3.2 respectively. The experimental system comprises of the counter flow channel, an electric heater, two fans, thermocouples, pressure transducer, IR camera, LDA system and inspection window.

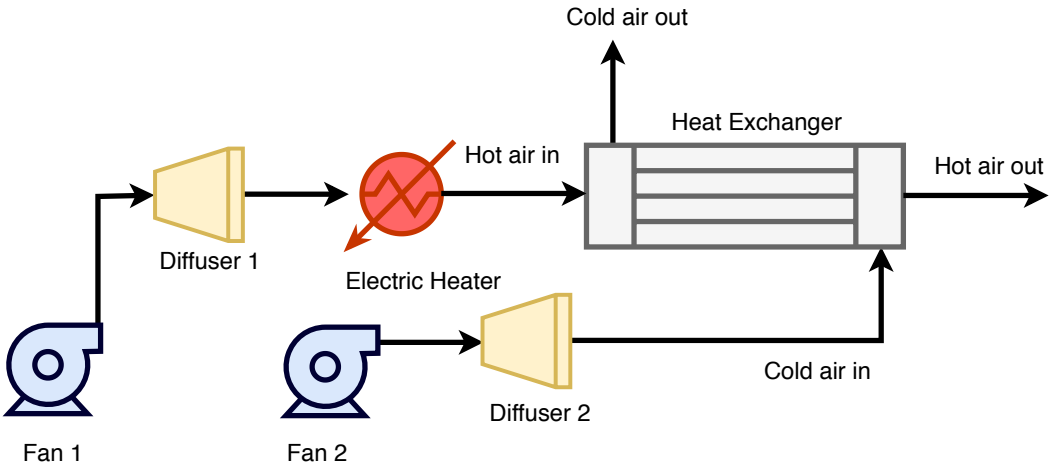

Figure 3.1: Schematic diagram of the experimental facility.

It is seen from Figure 3.1 that the experimental facility is open loop. The required volume flow rate is provided by two single inlet centrifugal fans with curved impellers and have the following specifications: Fan 1 - Casals AA 47T2, 1.1 kW and Fan 2 - Casals AAVG/N 502, 4 kW. The frequency of the fans is controlled to specify the desired flow rate. Air from fan 1 passes through diffuser 1 and contraction 1, followed by a honeycomb screen to straighten the flow. After that it flows through the heating section where its temperature is increased with the help of an electric heating mat, such that the temperature at the start of the experimental channel is not more than 85 °C . Next, this hot air enters the centre passage

Figure 3.2: Experimental facility built at the research and development department of APEX Group.

which has a saw tooth inlet geometry to trigger early transition to turbulent flow. From the other side, ambient air from fan 2, passes through diffuser 2 followed by a perforated plate before entering the top and bottom passage of the experimental channel. The frequency of fan 2 is maintained at a constant value of $f = 10$ Hz to ensure fully developed turbulent flow in the top and bottom passages.

Heat is exchanged through aluminium sheets between the centre passage and the top and bottom passage. The surface temperature of the top aluminium sheet is measured with the help of the IR camera and K-type surface thermocouples. The centre line temperature of the air is measured using K-type thermocouples. The static pressure is measured at 3 points upstream and 4 points downstream of the inspection window by Omega pressure transducers. The location of the pressure transducers and the thermocouples is shown in Figure 3.3

In order to reduce stray reflections from being captured, a protective covering from glass wool and thick cloth is built around the IR camera as shown in Figure 3.4. Table 3.1 shows the technical specifications of each component used for the experimentation.

3.1.1. Experimental channel

Figure 3.5 shows a schematic diagram of the experimental channel for determination of the heat transfer performance with dimple and protrusion surfaces. The configuration of the channel is counter current with air as the working fluid. The air is heated to a maximum temperature of 85 °C by using an electric heater. This hot air enters the channel straight through the centre passage and ambient cold air enters

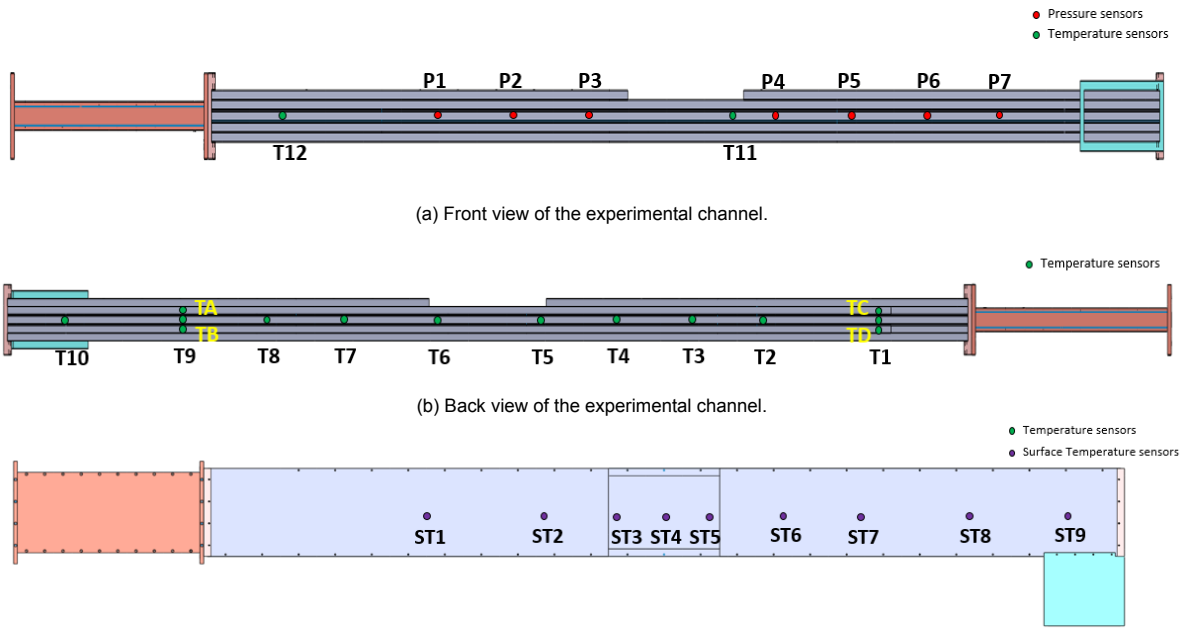

(a) Front view of the experimental channel.

(b) Back view of the experimental channel.

(c) Top view of the experimental channel.

Figure 3.3: Location of the pressure transducers, K type air thermocouples and K type surface thermocouples.

Figure 3.4: Protective covering from glass wool and thick cloth built around the IR camera to reduce capturing of stray signals.

the channel from the side into the top and bottom passage. The experimental test rig is manufactured from 10 mm and 20 mm thickness laser cut Plexiglas by company Stout Perspex [1], while the dimple-protrusion plates are punched on aluminium sheets of thickness 1.5 mm by Apex-Supply. Each passage

[1] Supplier of Plexiglas:
http://www.stoutperspex.nl/

Table 3.1: Technical Specifications of the measurement instruments.

Sr. No	Type of Sensor	Manufacturer	Model
1	IR camera	Testo	Testo 885
2	LDA	Dantec Dynamics	Flow Explorer
3	Thermocouples	RS components	K-type
4	Surface thermocouples	THERMA	K-type Self adhesive
5	Pressure transducers	Omega	PXM409 - 025 HGV
6	Data Acquisition	Omega	iNET 400 system
7	IR inspection window	FLIR	IRW-12PC Large Format
8	Temperature regulator	hillesheim	HT 40

has a width of $W = 200$ mm and height of $H = 10$ mm such that the aspect ratio is $W/H = 20$ and the hydraulic diameter is $D_h \approx 20$ mm . The length of the heat exchanger is $L = 2500$ mm. The velocity measurements using LDA are conducted from the side wall of the centre passage and the IR measurements are conducted through an inspection window in the centre of the top passage.

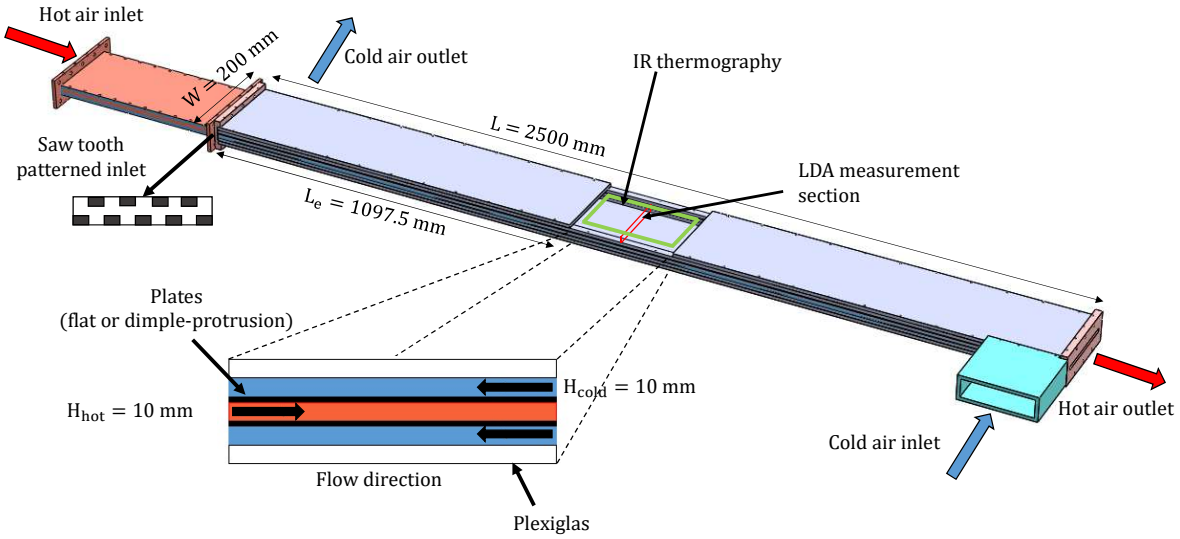

Figure 3.5: Schematic diagram of the experimental channel for calculation of heat transfer performance.

3.1.2. Entry length of the channel

The heat transfer performance of the channel with dimple-protrusion surfaces can be predicted rightly when the working fluid is thermally and hydro-dynamically fully developed. As stated by Incropera et al. [2007], for laminar flows fully developed condition in smooth ducts is achieved when $L_e/D_h \approx 0.05\, Re_{D_h} Pr$. There is no general expression for turbulent flows however, the entry length is hardly dependent on Reynolds number and it is assumed that the flow is fully developed for $L_e/D_h > 10$.

Since the region of interest is in the transitional and turbulent flow regime, the length of the entry section is $L_e \approx 1100$ mm or $L_e/D_h \approx 55$ to ensure thermal and hydro-dynamically fully developed flow at the start of the inspection region.

3.1.3. Guiding vanes

To guide the cold air flow smoothly into and out of the channel, guiding vanes are installed at the inlet and outlet of the top and bottom passages. The vanes have an aerodynamic NACA 16-005 profile with an extended trailing edge. Figure 3.6 shows the placement of the guiding vanes at the inlet and outlet of the cold air passages. They have a space to chord ratio s/c of 0.24 to prevent jet separation at the walls and formation of eddies as suggested by Lindgren et al. [1998] and Johl et al. [2007].

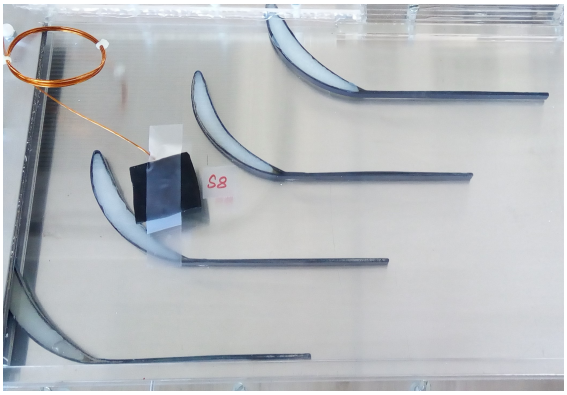

(a) Guiding vanes at the inlet to the cold air passage.

(b) Guiding vanes at the outlet to the cold air passage.

Figure 3.6: Placement of the guiding vanes at the inlet and outlet of the cold air passage to smoothen the flow.

A numerical simulation with and without guiding vanes is carried out for flat plate in FloEFD FE2019.1.0 at a Reynolds number of 5000. It is seen from Figure 3.7 that there is non uniform distribution and a high pressure loss at the top and bottom passages of the experimental channel without guiding vanes. This is due to a sharp change in the direction of the flow.

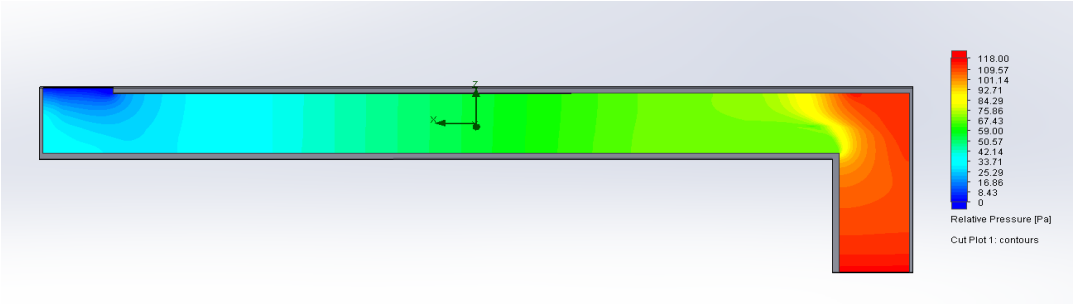

(a) Relative pressure contour without guiding vanes.

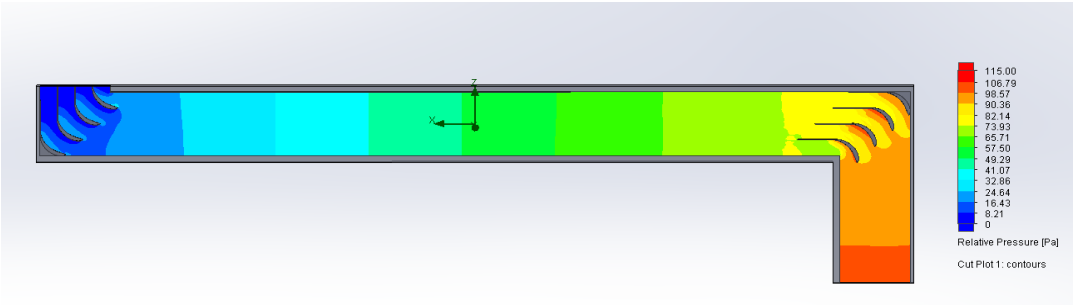

(b) Relative pressure contour with guiding vanes.

Figure 3.7: Comparison of pressure drop with and without guiding vanes at the inlet and outlet of the top and bottom passages in the experimental channel.

Also, as seen from Figure 3.8 the velocity profile at the centre of the passages without guiding vanes is sporadic. The introduction of guiding vanes drastically reduces zones of recirculating flows. It also helps to smoothen the flow and retain uniform flow characteristics at the centre of the channel as seen from Figure 3.9.

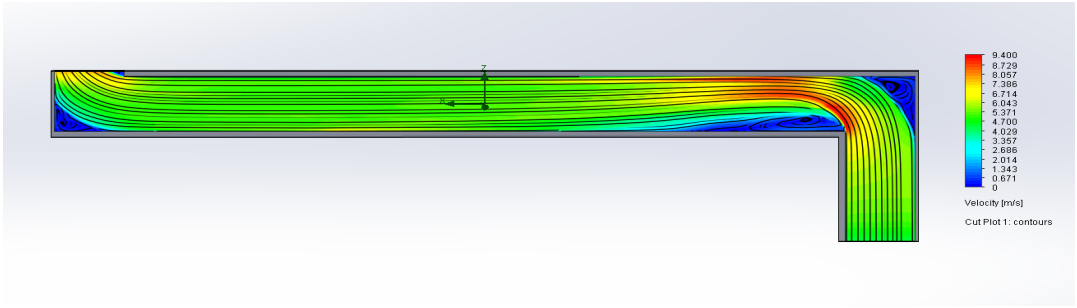

(a) Velocity contour and streamlines without guiding vanes.

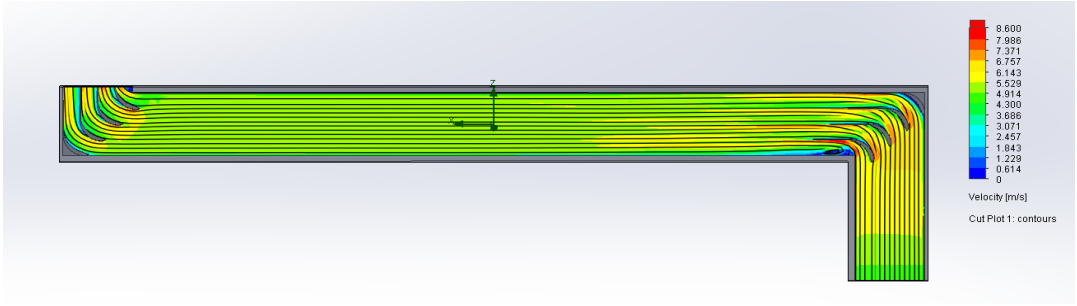

(b) Velocity contour and streamlines with guiding vanes.

Figure 3.8: Comparison of velocity contours and streamlines with and without guiding vanes at the inlet and outlet of the top and bottom passages in the experimental channel.

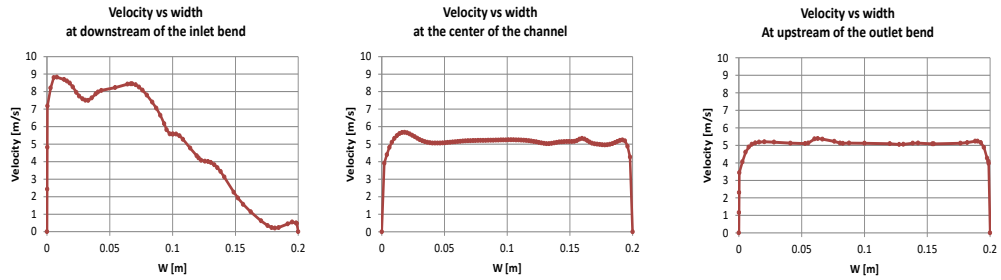

(a) Velocity profile without guiding vanes.

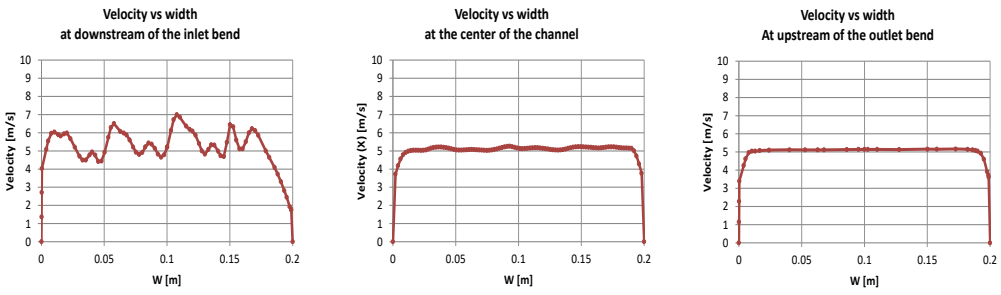

(b) Velocity profile with guiding vanes.

Figure 3.9: Comparison of velocity profile with and without guiding vanes at the downstream of the inlet bend x = 450 mm, centre x = 1250 mm and upstream of the outlet bend x = 2050 mm of the experimental channel.

3.1.4. Details of dimple and protrusion plates

To develop a good correlation for the prediction of the Nusselt number and friction factor for surfaces with dimples and protrusions, measurements need to be conducted on plates with varying geometrical parameters. Thus, the dimple-protrusion plates are designed in staggered and inline configuration as shown in Figure 3.10.

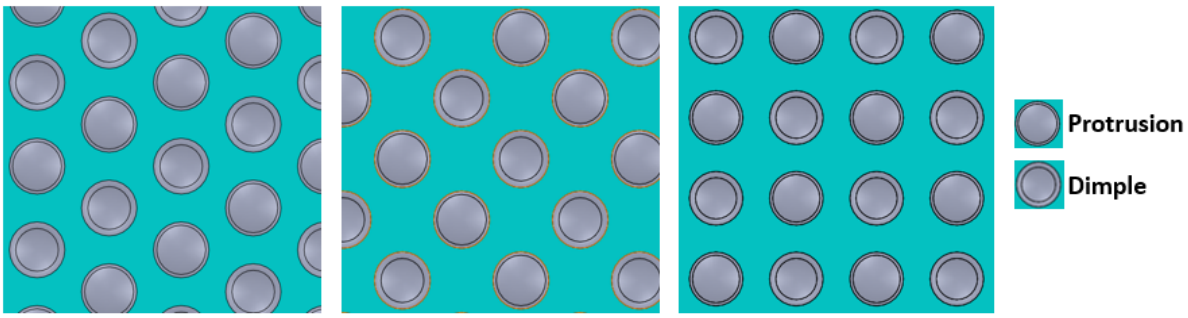

Figure 3.10: Configuration of the dimple-protrusion plate for the development of Nusselt number and friction factor correlations. Left and centre image have staggered orientation and the right image shows an inline configuration.

The range of parameters for the dimple and protrusion plates, to develop a correlation for the prediction of the Nusselt number and friction factor are shown in Table 3.2.

Table 3.2: Parameter of the dimple and protrusion plates.

Sr. No	Parameter	Value
1	Relative pitch (S/h)	15, 20, 25
2	Angle (α)	30°, 45°, 90°
3	Relative print diameter (d/D_h)	*0.368, 0.525, 0.735*
4	Relative roughness height (h/H)	*0.07, 0.1, 0.14*
5	Roughness height to print diameter (h/d)	*0.1*

However, due to a long time period required to manufacture and deliver these plates, experiments were performed on a set of flat plates and one staggered orientation dimple-protrusion plates. Figure 3.11 shows the configuration of the dimple-protrusion plate on which the experiment is performed.

In order to reduce reflection during optical flow measurement and to increase the infrared emissivity of the aluminium surface, the sheets are painted black using Rust-Oleum Hard Hat Heat-resistant Spray. This spray paint can withstand a continuous load of up to 650 °C. [2]Table 3.3 shows the parameter of the staggered orientation dimple-protrusion plate on which the measurements were performed.

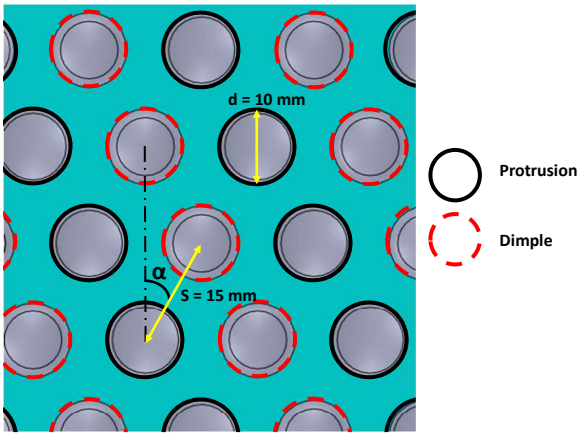

Figure 3.11: Configuration of the dimple-protrusion plate with staggered arrangement.

[2]Specifications of Rust-Oleum Hard Hat Heat-resistant Spray:
https://www.verfwinkel.nl/rust-oleum-hard-hat-hittebestendig.html

Table 3.3: Parameter of the staggered orientation dimple-protrusion plate.

Sr. No	Parameter	Value
1	Relative pitch (S/h)	15
2	Angle (α)	30°
3	Relative print diameter (d/D_h)	0.525
4	Relative roughness height (h/H)	0.1
5	Roughness height to print diameter (h/d)	0.1

3.2. Contact measurements

Before the beginning of the experimentation, the pressure sensors and the air thermocouples were calibrated in the Fluid mechanics lab at TU Delft. This section briefly describes the procedure of calibration for the pressure transducers and the thermocouples.

3.2.1. Calibration of pressure transducer

The static pressure inside the channel is measured using Omega PXM409 Pressure Transducers. These pressure transducers are calibrated using a Betz manometer, which can accurately measure small pressure differences. The setup for the calibration of the pressure transducers is shown in Figure 3.12a. The Betz manometer has a resolution of 0.1 mm of water column with the fluid density equal to 998 kg/m^3. The procedure for obtaining the calibration curves of the pressure transducers is summarized in appendix A.1.

3.2.2. Calibration of thermocouples

Air temperature is measured using K-type thermocouples with probe length and diameter equal to 150 mm and 1.5 mm respectively. These thermocouples are calibrated for the operating range, using an accurate temperature controlled water bath (type: Julabo 5014) as shown in Figure 3.12b. The temperature controller has a resolution of 0.01 °C and an absolute accuracy of 0.04 °C. The calibration curves for the thermocouples is shown in appendix A.2

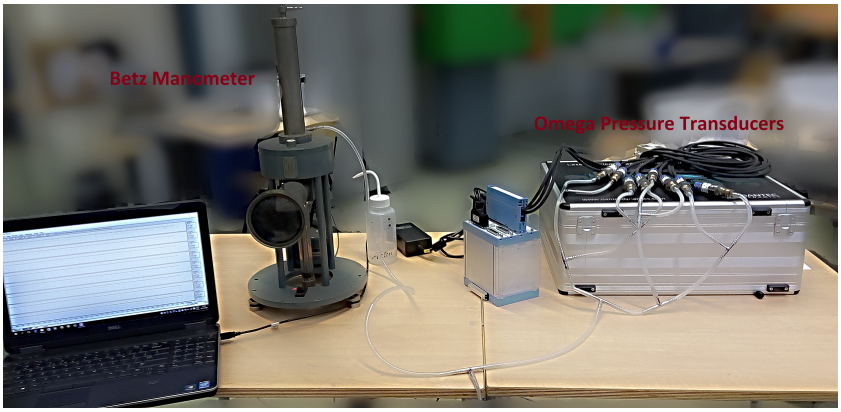

(a) Betz manometer

(b) Water bath

Figure 3.12: (a) Calibration of Omega Pressure Transducers using a Betz Manometer with optical reading system for low pressure difference measurements, (b) Calibration of K type Thermocouples using an accurate temperature controlled water bath for 18 - 60 °C.

3.3. Non-contact measurements

Over the last few decades contactless techniques have been investigated extensively to improve the accuracy of measurements. In this study, two non intrusive methods are selected namely Laser Doppler Anemometry (LDA) and Infrared (IR) thermography. LDA is used to measure the stream-wise velocity component of the flow, while IR thermography is used to determine the wall temperature distribution on the aluminium plates of the heat exchanger.

3.3.1. Laser doppler anemometry

The stream-wise velocity profile of air in the centre channel with flat or dimple-protrusion aluminium sheets is investigated using point wise non invasive optical LDA technique from the top wall to the bottom wall of the hot passage. The major advantage of LDA is that the measurement technique is non intrusive and has the ability to cope with extremely low velocities as well as turbulent flows due to its high spatial and temporal resolution. Besides the time averaged velocity, LDA allows the analysis of temporal fluctuations u' and consequently the calculation of turbulence intensity of the flow.

Seeding and measurement volume

LDA measures the velocity of tracer particles in the air and not directly of the air flow itself. Thus, the rate of measurement depends on the seeding concentration. Di-Ethyl-Hexyl-Sebacat (DEHS) is used as seeding particle for velocity measurements and the particles resulting from the Laskin nozzle used to create them have a size of around $1\,\mu$m.

The measurement volume should be small for good spatial resolution. LDA measurements are conducted using a monochromatic yellow laser with wavelength 561 nm to achieve high signal to noise ratio. The position of the intersection of the laser beams is accurately controlled with the help of a 3D Dantec traverse system and the measurement volume size is $0.083 \times 0.082 \times 0.83\,\text{mm}^3$.

3.3.2. Infrared thermography

Infrared radiation is emitted by all objects, and the intensity of radiation increases with rise in temperature. Capturing part of the emitted radiation can provide relative comparison of surface temperatures over a wide area without any contact. Thus, the temperature at the surface of the aluminium sheet is measured using infrared thermography.

Calibration of IR Inspection window

In order to obtain an accurate measure of the surface temperature, the IR inspection window is calibrated using a homogeneous aluminium block. A sample black painted aluminium sheet is attached to the block which is uniformly heated with the help of a hot plate with a regulated power supply. A calibration adhesive tape (by FLIR) of known emissivity $\epsilon = 0.95$ is pasted on the sample sheet and temperature readings are recorded by the IR camera with and without the inspection window. Figure 3.14 displays the thermal image of the sample aluminium sheet with and without the FLIR IR window which is processed using the software IRSoft to determine the transmissivity of the inspection window.

It is observed that the emissivity of the black paint is $\epsilon = 0.91$ and the transmissivity τ of the FLIR IR inspection window is 0.55 when the temperature of the aluminium block is 27.8 °C. The temperature of the aluminium block is raised to 43.3 °C and 52 °C, for which the transmissivity of the inspection window is found to be 0.53 and 0.5 respectively. Thus, it is established that the transmissivity of the IR window is not a constant value and needs to be determined explicitly while performing the experiments. Therefore, it is determined for each measurement with the help of the surface thermocouples ST3, ST4 and ST5 as shown in Figure 3.3c while performing the experiments. The value of transmissivity for the measurement with uniformly heated aluminium block, smooth flat surface and dimple-protrusion surface at different surface temperatures is shown in appendix A.3.

3.4. Experimental procedure

In order to determine the friction factor and the local heat transfer coefficient, the experimental procedure adopted for all test cases is as follows:

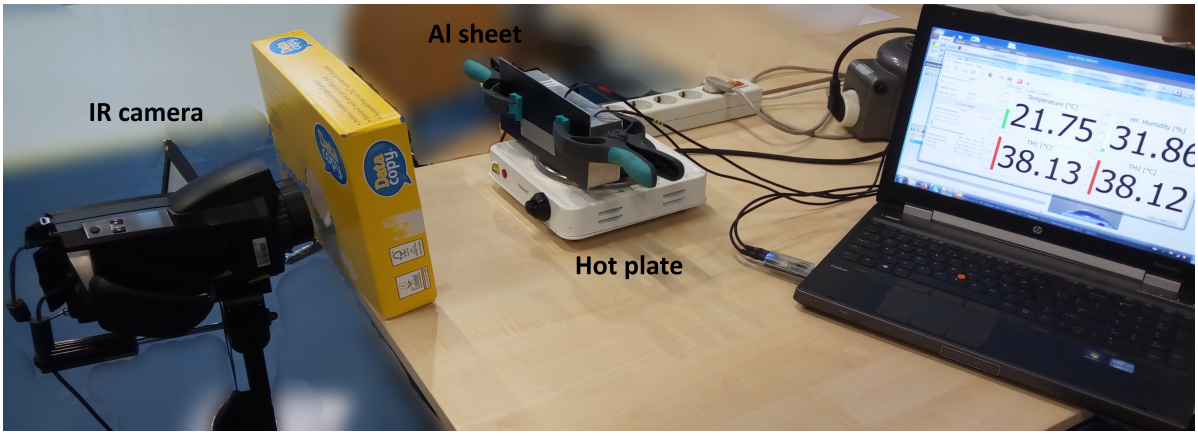

Figure 3.13: Setup for the calibration of FLIR IR inspection window with a uniformly heated aluminium block.

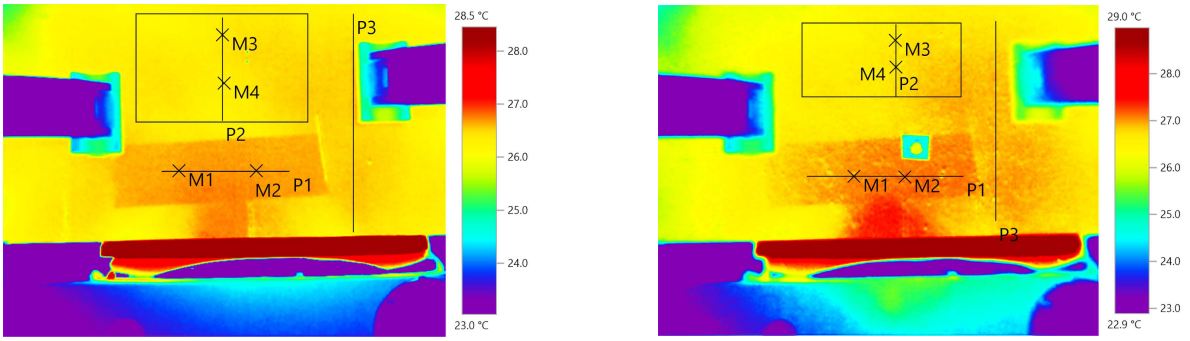

(a) Aluminium sheet with reference tape

(b) Aluminium sheet with FLIR window and reference tape

Figure 3.14: Calibration of FLIR window with a sample aluminium sheet using a uniformly heated aluminium block at surface temperature of 27.8 °C and a reference tape with known emissivity $\epsilon = 0.95$.

1. To conduct the experiments, the electric mat is first heated to a temperature of 275 °C without the flow of air in the channels. It is followed by measurement of pressure inside the channel to correct for zero error.

2. Next, the mass flow rate for hot air is controlled by changing the frequency of the fan 1. The flow rate of cold air is maintained constant with the frequency of fan 2, $f = 10$ Hz to ensure a fully developed turbulent flow field in the cold passage. Up to 1 hour is required to reach steady state from cold conditions and measurements are conducted after temperature variations inside the channel are less than 0.1 °C over 10 - 15 minutes.

3. After that 3 images are taken with the IR camera to measure the surface temperature of the aluminium plates.

4. This is followed by conducting LDA and pressure measurements inside the hot channel.

5. After which, the surface and air temperature are measured at the locations shown in Figure 3.3. The temperature profile of the hot air is carefully measured by recording the temperature across the hot passage at z = 0 mm, 2.5 mm, 5 mm, 7.5 mm and 10 mm.

6. Finally, again 3 images are taken with the IR camera to measure the surface temperature of the aluminium plates.

Concluding Remarks

This chapter discusses in detail the design and building of the setup to analyze the performance of dimple-protrusion surface in a counter flow heat exchanger. The experiments are conducted using calibrated contact and non-contact measuring techniques.

4

Data reduction

This chapter details the methodology of post processing the data obtained from the measurements as described in section 4.1. Section 4.1.3 and 4.1.4 presents the method to calculate the global Darcy friction factor and the local and average Nusselt number respectively. It is followed by an uncertainty analysis in section 4.2 for the measurement of essential parameters.

4.1. Post processing

The methodology for data reduction further helps in the post processing of the measured data. The pressure measurements yield the Darcy friction factor and the temperature measurements using IR thermography help to determine the local Nusselt number.

4.1.1. Mean velocity calculations

The rate of heat transfer between the hot and cold channels in a heat exchanger rises as the velocity of air increases. Thus, it is essential to determine the velocity profile inside the hot channel. The velocity profile is studied inside the centre passage of the channel for laminar, transitional and turbulent flow fields. LDA measurements are conducted at 13 positions along the width at half channel depth and the centerline velocity profile is obtained with 21 points across the height of the channel as shown in Figure 4.1. To ensure sufficient signal bursts, the measurement is conducted with the limit of 100,000 samples or 20 seconds measurement time. Thus, the average data rate for measurements is ensured to be around 2 kHz.

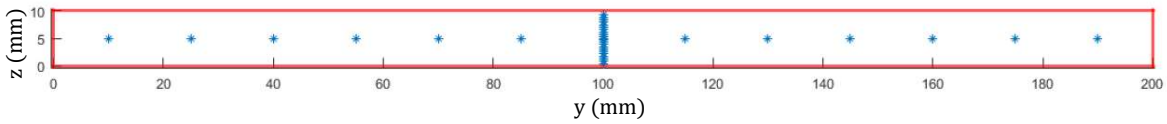

Figure 4.1: Location of LDA measurements.

In case of laminar channel flow, the velocity has a parabolic profile while for turbulent flows it follows a power law profile as shown in equation 4.1 and 4.2 respectively.

$$\text{Laminar velocity profile} : u = u_{max}\left[1 - \left(\frac{H/2 - z}{H/2}\right)^2\right] \tag{4.1}$$

$$\text{Turbulent velocity profile} : u = u_{max}\left(\frac{z}{H/2}\right)^{\frac{1}{n}} \tag{4.2}$$

where, z is the distance from the wall of the channel. In the transitional flow regime the velocity profile is determined by using a 6^{th} order polynomial curve fitting of the measured data points at the centre width y = 100 mm.

Using the centerline velocity profiles obtained from the measured data points at y = 100 mm, the u-velocity component is calculated at the remaining 12 locations along the width with a step of 0.1 mm across the height of the channel under the assumption that the same velocity profile holds at all y positions.

Thereafter, the mean velocity in the channel is determined by area averaging the interpolated data points. The mean velocity provides for the calculation of the volume flow rate and the dynamic pressure inside the channel.

$$u_{mean} = \frac{1}{A_f} \iint_{CS} \underline{u} \cdot n \, dS \tag{4.3}$$

where, $\underline{u}$ is the velocity vector, n is the unit vector and A_f is the area of the flow inside the hot channel.

4.1.2. Turbulence intensity

In addition to the mean velocity profile, LDA data enables us to analyze the temporal velocity fluctuations (u') and consequently the turbulence intensity based on the mean velocity.

$$u_{rms}(z) = \sqrt{u'(z)^2} \tag{4.4}$$

$$Tu(z) = \frac{u_{rms}(z)}{u_{mean}} \tag{4.5}$$

4.1.3. Darcy friction factor

The pressure gradient in the stream-wise direction is a major characteristic of the flow field to determine the performance of a heat exchanger. The change in pressure occurs due to two phenomena. Firstly, the loss in pressure due to friction from the surface of the channel and secondly an increase in pressure due to the change in temperature of the air inside the channel.

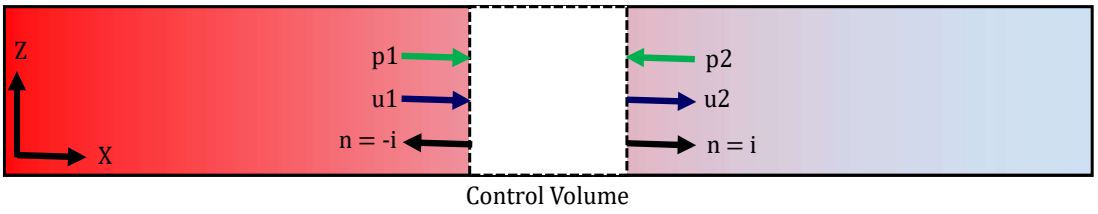

Figure 4.2: Control volume in the centre passage of the experimental channel with the flow direction from left to right.

The principle of conservation of mass states that the rate of change of mass in a control volume is equal to the net mass flow rate through the control surface coming outside of the control volume.

$$\frac{d}{dt} \iiint_{CV} \rho \, dV = - \iint_{CS} \rho \, \underline{u} \cdot n \, dS \tag{4.6}$$

The difference in static pressure due to the change in density of the air inside the channel is computed from the integral momentum balance in an inertial frame of reference with body force represented as $\underline{f}$. The conservation of momentum for a fluid is described by equation. 4.7

$$\frac{d}{dt} \iiint_{CV} \rho \, \underline{u} \, dV = - \iint_{CS} \rho \, \underline{u} (\underline{u} \cdot n) \, dS + \iint_{CS} - p \, n \, dS + \iiint_{CV} \underline{f} \, dV \tag{4.7}$$

For steady state and flat velocity profiles,

$$m = \rho_1 \, u_1 \, A = \rho_2 \, u_2 \, A \tag{4.8}$$

$$-\rho_1 \, {u_1}^2 A + \rho_2 \, {u_2}^2 A = p_1 \, A - p_2 \, A \tag{4.9}$$

By combining the conservation of mass and momentum in the x-direction for steady state as shown in equation 4.8 and 4.9 respectively, it is found that the difference in static pressure due to change in the density can be expressed as shown in equation. 4.10

$$(p_1 - p_2)_{cons} = \frac{m^2}{A^2}\Big(-\frac{1}{\rho_1} + \frac{1}{\rho_2}\Big) \tag{4.10}$$

In order to reduce the uncertainty in the experimentation, the pressure data is measured at 7 locations in the hot channel as shown in Figure 3.3a. The measured pressure drop is calculated with the help of the slope of the line fit between the pressure and x-location.

$$(p_1 - p_2)_{measured} = \frac{dp}{dx} \times (x_2 - x_1) \tag{4.11}$$

Figure 4.3 shows an example of the first order linear fit applied to the pressure data in order to calculate the measured pressure drop inside the hot channel.

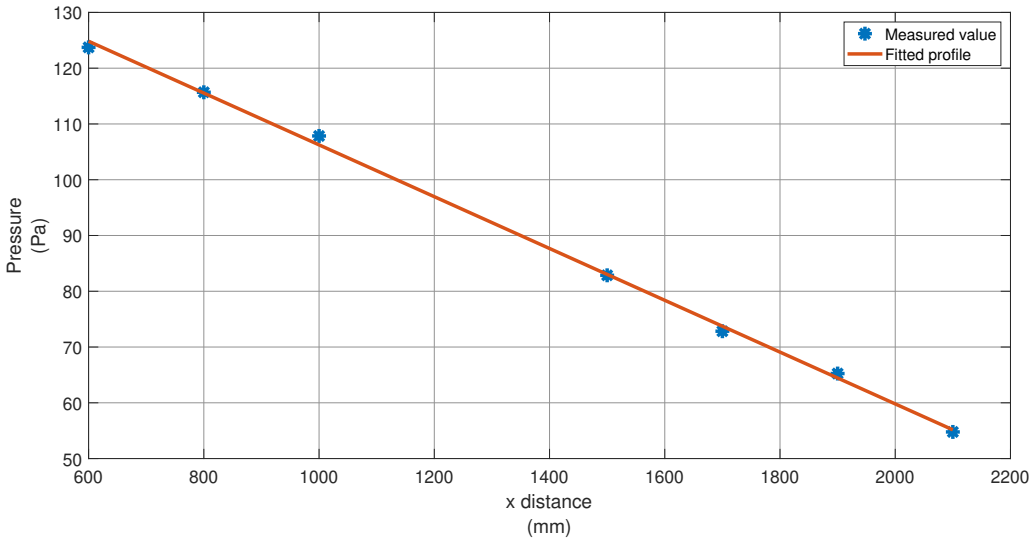

Figure 4.3: An example of the 1^{st} order linear fit applied to the measured pressure data.

Therefore, the pressure drop due to friction from the surface of the channel is as follows:

$$(p_1 - p_2)_{friction} = (p_1 - p_2)_{measured} - (p_1 - p_2)_{cons} \tag{4.12}$$

Thus, for incompressible flows, the Darcy friction factor f_b evaluated at bulk properties between two locations in the channel is characterized as :

$$f_b = \frac{(p_1 - p_2)_{friction}}{x_2 - x_1} \times \frac{2\,D_h}{\rho\,u^2{}_{mean}} \tag{4.13}$$

Wall shear stress

Using the integral force balance the mean wall shear stress can be computed in terms of the hydraulic diameter and pressure gradient as follows:

$$\tau_w = -\frac{D_h}{4} \times \left(\frac{dp}{dx}\right)_{friction} \tag{4.14}$$

Variable property effect

As large temperature gradients are expected, it is likely that the variable property effects will be significant. The Darcy friction factor can be computed after correcting for the variable property effect in a

cooling duct by applying a temperature correction ratio for gases as proposed by Mills [1999]. A further complication for internal flows is that both the wall and bulk temperature vary along the channel as heat is removed. Thus, for all the experiments the temperature correction ratio is evaluated by using the arithmetic average temperature of the surface thermocouple and the bulk air temperature.

$$\text{Laminar flows} : f = f_b \left(\frac{T_s}{T_b}\right) \tag{4.15}$$

$$\text{Turbulent flows} : f = f_b \left(\frac{T_s}{T_b}\right)^{-0.1} \tag{4.16}$$

4.1.4. Nusselt number

The Nusselt number is referred as the dimensionless heat transfer coefficient. In order to determine the heat transfer coefficient it is essential to calculate the heat flux, the surface temperature and the bulk air temperature.

Heat Flux

For a counter flow heat exchanger with air as the fluid obeying ideal gas laws, the steady state energy equation can be written as:

$$Q_u = m\, c_p\, (T_{hot_{in}} - T_{hot_{out}}) = m\, c_p\, (T_{c_2} - T_{c_9}) \tag{4.17}$$

where, m is the mass flow rate of air, $T_{hot_{in}}$ and $T_{hot_{out}}$ are the centerline temperatures measured at location T2 and T9 respectively as shown in Figure 3.3b and c_p is the specific heat at constant pressure determined at the temperature at the location of the LDA measurements. Using the useful heat loss, the overall heat flux is calculated as shown in equation. 4.18

$$q = \frac{Q_u}{2\,(W+H)\,L} = \frac{Q_u}{2\,(W+H)\,(x_9 - x_2)} \tag{4.18}$$

Surface temperature

The surface temperature of aluminium at the hot air side is calculated by considering a thermal circuit as shown in Figure 4.4. The surface temperature of the aluminium plate near the cold air side is measured using the IR camera. An average of 6 thermal images is taken to improve the signal to noise ratio.

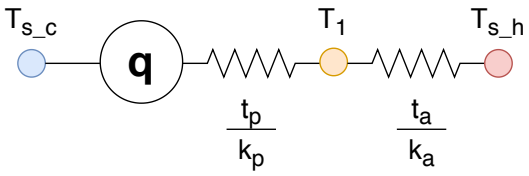

Figure 4.4: Thermal circuit to determine the surface temperature of aluminium at the hot air side.

Assuming the thickness of the black paint layer t_p = 0.2 mm the thermal conductivity k_p = 0.5 W/m K. While the thickness of the aluminium plate is t_a = 1.5 mm and the thermal conductivity is k_a = 205 W/m K. Therefore, the thermal resistance of the paint layer and aluminium plates is found to be:

$$\text{Thermal resistance of paint } R_p = \frac{t_p}{k_p} = \frac{0.2 \times 10^{-3}}{0.5} = 4 \times 10^{-4}\ \text{K m}^2/\text{W}$$

$$\text{Thermal resistance of Al plate } R_a = \frac{t_a}{k_a} = \frac{1.5 \times 10^{-3}}{205} = 7.3 \times 10^{-6}\ \text{K m}^2/\text{W}$$

It is found that the thermal resistance due to black paint and aluminum plate is small compared to the typical resistances due to the flow, that are of $\mathcal{O}(10^{-1}$ K m^2/W), as seen later. Therefore the surface temperature of aluminium at the hot air side can be expressed as:

$$T_{s_h} \approx T_{s_c} = T_s$$

Bulk air temperature

The bulk air temperature can be calculated using the velocity and temperature profile. In the turbulent flow regime the temperature profile can be expressed as explained in section 2.3:

$$\frac{T_s - T}{T_\tau} = T^+ \tag{4.19}$$

$$T_\tau = \frac{-q}{\rho\, c_p\, u_\tau} \tag{4.20}$$

where, T_τ is the friction temperature based upon the wall heat flux, friction velocity and specific heat capacity. The friction velocity u_τ is based upon the wall shear drag and density which can be expressed as $\tau_w = \rho u_\tau^2$.

For smooth plates the logarithmic law provides a good estimate of the temperature profile.

$$\text{In the log law regime}: T^+ = \frac{1}{\kappa_\theta} \ln z^+ + A_\theta \qquad \text{with } z^+ = \frac{z\, u_\tau}{\nu} \tag{4.21}$$

$$\text{In the viscous sub layer}: T^+ = Pr\, z^+ \tag{4.22}$$

where κ_θ is the von Karman constant with $\kappa_\theta \approx \kappa_m / Pr_t \approx 0.46$ and A_θ is an additive constant which is determined from the hot air temperature measurements across the height of he channel.

In the laminar and transitional flow regime, the temperature profile is determined by using a 4^{th} order polynomial curve fitting of the measured data at z = 0 mm, 2.5 mm, 5 mm, 7.5 mm and 10 mm. Figure 4.5 shows an example of the 4^{th} order polynomial curve fit applied to the measured temperature data for transitional and laminar flows.

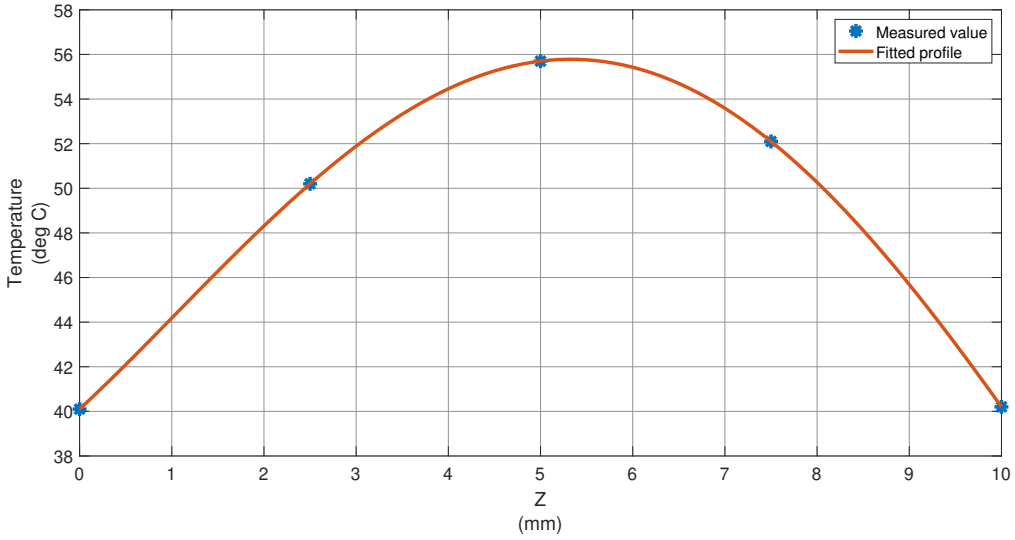

Figure 4.5: An example of the 4^{th} order polynomial curve fit applied to the measured temperature data for transitional and laminar flows.

For dimple-protrusion surfaces, the turbulent temperature profile is corrected with a temperature shift ΔT^+ as discussed in section 2.4.

$$\text{In the log law regime}: T^+ = \frac{1}{\kappa_\theta}\ln z^+ + A_\theta - \Delta T^+ \tag{4.23}$$

Thus, the bulk air temperature near the inlet and outlet of the IR window can be determined using the velocity and temperature profile as:

$$T_b = \frac{\int u\,T\,dz}{\int u\,dz} \tag{4.24}$$

Starting from the measured bulk temperature near the inlet of the IR window T_{b_5}, the downstream T_b values along the stream wise direction with an interval of Δx is evaluated as:

$$T_b(x_{i+1}) = T_b(x_i) - \frac{(T_{b_5} - T_{b_6})\,\Delta x}{x_6 - x_5} \tag{4.25}$$

Local heat transfer coefficient

To determine the local heat transfer coefficient, it is required to calculate the local heat flux (q_{local}). First, the centerline temperature at z = 5 mm is determined for the entire length of the channel by using an exponential curve fit of the measured data at the locations shown in Figure 3.3b. An example of the exponential fit for the measured centerline temperature data is shown in Figure 4.6.

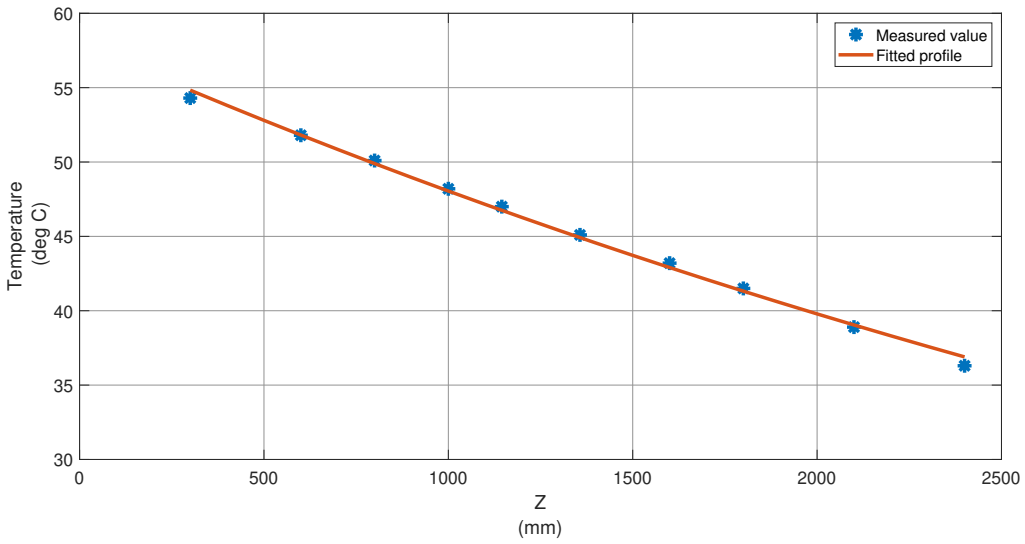

Figure 4.6: An example of the exponential curve fit applied to the measured centerline temperature data.

After that, the local heat flux is evaluated, with the fluid properties at the reference temperature, as shown in equation 4.26. The local heat transfer coefficient inside the hot channel is then determined using Newton's law of cooling as shown in equation 4.27, with T_c evaluated from the exponential curve fit.

$$q_{local} = \frac{m\,c_{p_i}\,[T_c(x_i) - T_c(x_{i+1})]}{2\,W\,(x_{i+1} - x_i)} \tag{4.26}$$

$$h_l = \frac{q_{local}}{T_b - T_s} \tag{4.27}$$

Local Nusselt number

The fluid properties to determine the local Nusselt number are evaluated, using REFPROP version 9.0, at the reference temperature T_r which is the mean of the surface and bulk air temperature. Thereby, the dimensionless Nusselt number is calculated as shown in equation 4.29:

$$T_r = \frac{T_s + T_b}{2} \tag{4.28}$$

$$Nu_l = \frac{h_l\, D_h}{k_f} \tag{4.29}$$

Average Nusselt number

The overall average Nusselt number is obtained by the following numerical integration as shown in equation. 4.30

$$Nu = \frac{\iint Nu_l\, dxdy}{\iint dxdy} \tag{4.30}$$

4.1.5. Overall heat transfer coefficient

The total heat transfer in a heat exchanger can be written as:

$$Q_u = U\, \mathcal{P}\, L\, \Delta T_{lm} \tag{4.31}$$

where, U is the overall heat transfer coefficient, $\mathcal{P}$ is the perimeter of heat transfer and ΔT_{lm} is the logarithmic mean temperature difference.

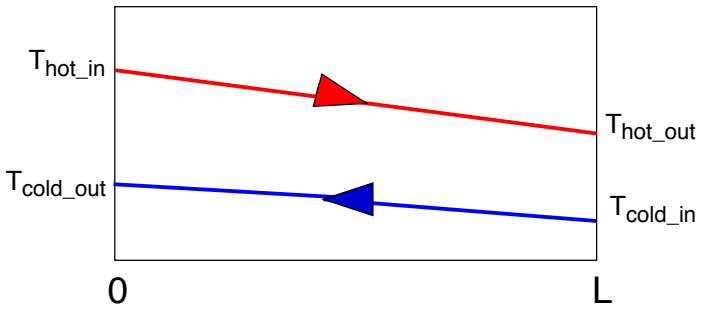

Figure 4.7: Fluid temperature variation along a counter flow heat exchanger.

For a counter flow heat exchanger, the logarithmic mean temperature difference is expressed as shown in equation 4.32:

$$\Delta T_{lm} = \frac{(T_{hot_{in}} - T_{cold_{out}}) - (T_{hot_{out}} - T_{cold_{in}})}{\ln\left(\frac{T_{hot_{in}} - T_{cold_{out}}}{T_{hot_{out}} - T_{cold_{in}}}\right)} \tag{4.32}$$

$$\text{where,} \quad T_{cold_{in}} = \frac{T_A + T_B}{2} \qquad T_{cold_{out}} = \frac{T_C + T_D}{2}$$

4.1.6. Performance factor

The performance factor (PF) is obtained by considering both the heat transfer enhancement and the pressure loss increment based on constant power condition. It is defined as a ratio of the volume goodness factor for dimple-protrusion plate to that of flat plate.

$$\text{Volume goodness factor } = \frac{St}{f^{1/3}} \tag{4.33}$$

$$\text{Performance factor } \eta = \frac{Nu/Nu_0}{(f/f_0)^{1/3}} \tag{4.34}$$

where, Nu_0 and f_0 are the Nusselt number and the friction factor for the hot channel with smooth surfaces.

4.2. Measurement uncertainty

The experimental data obtained may differ from its true value due to the presence of different factors while evaluation and recordings. Thus, an uncertainty analysis has been carried out to estimate the errors involved in the experimental data measurement. The relative uncertainty of various important quantities has been evaluated by the method described by Moffat [1988]. The procedure for computation of relative uncertainty is discussed in Appendix B. Table 4.1 shows the maximum uncertainty in the measurement of essential parameters.

Table 4.1: Uncertainty in the measurement of essential parameters.

Sr. No	Parameters	Maximum Error %
1	Mass flow rate (m)	5.11
2	Useful Heat Loss (Q_u)	5.12
3	Heat transfer coefficient (h)	5.18
4	Reynolds number (Re)	4.87
5	Nusselt number (Nu)	7.04
6	Friction factor (f)	5.45
7	Stanton number (St)	8.56
8	Volume goodness factor (VGF)	8.75
9	Performance factor (η)	10.28

5

Results and analysis

The methodology to determine the Darcy friction factor and local Nusselt number is described in the previous chapter. Having laid down the groundwork, this chapter focuses on the results obtained from the experiments. Firstly, a validation test is conducted without and with heating in the experimental channel with flat plates as described in section 5.1. It is followed by measurement and analysis of the friction factor and Nusselt number with dimple-protrusion plates in section 5.2. Lastly, a comparison is made between the dimple-protrusion plate and smooth flat plate in section 5.3.

5.1. Validation of the experimental setup - smooth flat plate

To ensure the reliability of the experiments, the obtained data for a smooth rectangular channel are verified by comparing them with empirical correlations in cold and heated conditions. This comparison provides a general basis for evaluating the experimental methods employed and serves as a reference for the results obtained with dimple-protrusion surfaces. The performance of the experimental setup is assessed first by measuring the mean velocity profiles. It is followed by friction factor measurements. Lastly, the accuracy of the Nusselt number data in heated channel is verified for the smooth flat-plate heat exchanger.

5.1.1. Velocity measurements

Figure 5.1 shows an example of the measured data and the fitted velocity profile for the test conducted in hot conditions at y = 100 mm. It is seen that the flow follows a parabolic profile for low Reynolds number and a power law profile with index $n = 11$ for the highest Reynolds number as discussed in section 4.1.1. The velocity fluctuations in the central channel in hot conditions at y = 100 mm is shown in Figure 5.2. It is observed that the laminar flow has the lowest fluctuations and it increases with the increase in flow speeds. Also, the u_{rms} profile indicates an increase in unintended reflections near the walls. Figure 5.3 shows the normalized u-component of velocity for laminar, transitional and turbulent flow regimes. It is seen that the velocity profile becomes flat as the velocity increases.

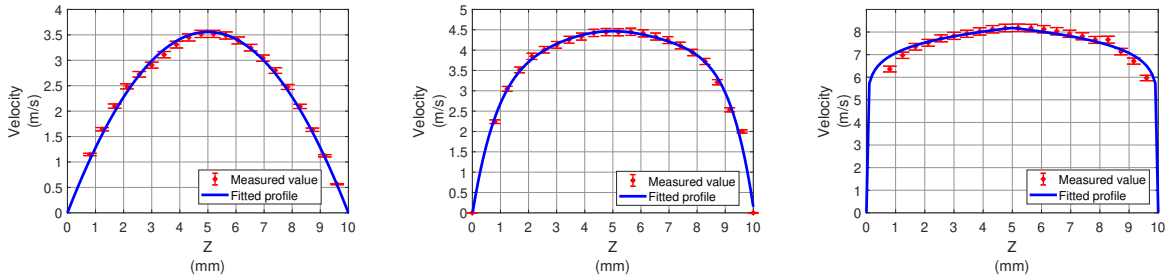

(a) Laminar flow Re = 2341. (b) Transitional flow Re = 3535. (c) Turbulent flow Re = 7924.

Figure 5.1: u-velocity profile for flat plates in a rectangular channel for (a) Laminar flow (b) Transitional flow and (c) Turbulent flow.

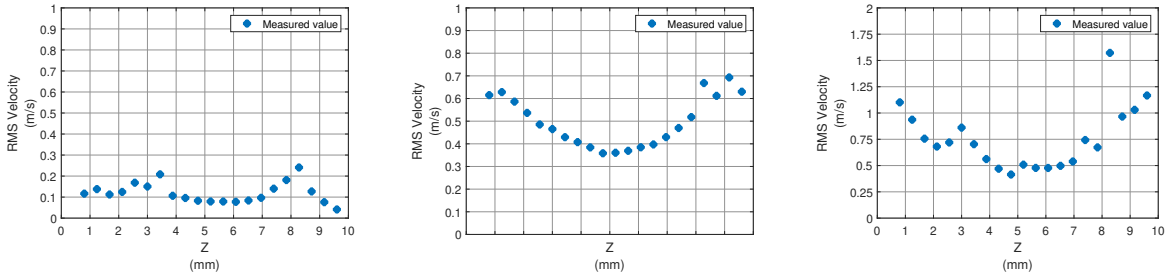

(a) Laminar flow Re = 2341. (b) Transitional flow Re = 3535. (c) Turbulent flow Re = 7924.

Figure 5.2: u_{rms} profile for flat plates in a rectangular channel for (a) Laminar flow (b) Transitional flow and (c) Turbulent flow.

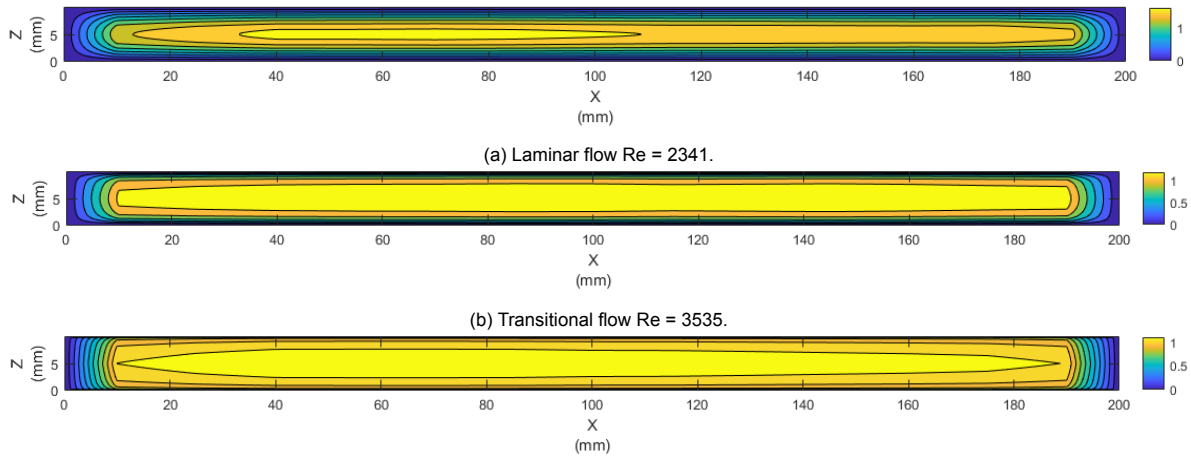

(a) Laminar flow Re = 2341.

(b) Transitional flow Re = 3535.

(c) Turbulent flow Re = 7924.

Figure 5.3: Normalized u-component of velocity u/u_{mean} for flat plates in a rectangular channel for (a) Laminar flow (b) Transitional flow and (c) Turbulent flow.

5.1.2. Turbulence intensity

Turbulence intensity represents the intensity of velocity fluctuations and indicates the turbulent mixing in the flow which helps in improving the heat transfer rate. The onset of transitional and turbulent flow can be determined through the measurement of the turbulence intensity in the flow at z = 5 mm.

It is seen from Figure 5.4 for smooth flat surfaces, the flow is in the laminar regime up to Reynolds number of 2775 in cold conditions and 2847 in hot condition. After which the temporal fluctuations increase in the transitional zone up to Reynolds number equal to 3953 with a peak at Re = 3535 for both conditions. After Re = 3953, the turbulence intensity starts to decrease gradually in the turbulent flow regime as the fluctuation in the flow with respect to the mean velocity reduce with the increase in flow speed. Slight differences are observed in the cold and heated conditions in the laminar and transitional flow regime. This is because for constant velocity in the cold channels, the temperature of air rises in the hot channel from turbulent to laminar flow regime. This leads to a decrease in the density of air and an increase in vortices for better mixing of the fluid within the hot channel. Thereby, causing an increase in the velocity fluctuations.

Figure 5.5 shows the turbulence intensity across the height of the centre passage with flat plates in heated condition at y = 100 mm for laminar, transitional and turbulent flow regime. The highest turbulence intensity is seen in the transitional flow regime due to intermittent occurrence of laminar and turbulent flow state which shows larger temporal and spatial irregular fluctuations.

5.1.3. Friction factor measurements

The uncertainty of the friction factor data collected is assessed in cold and heated environment with the correlations mentioned in section 2.1. It is found from Figure 5.6, that the friction factor results are close to the Blasius equation and the theoretical laminar limit for the hot conditions. It is also seen that

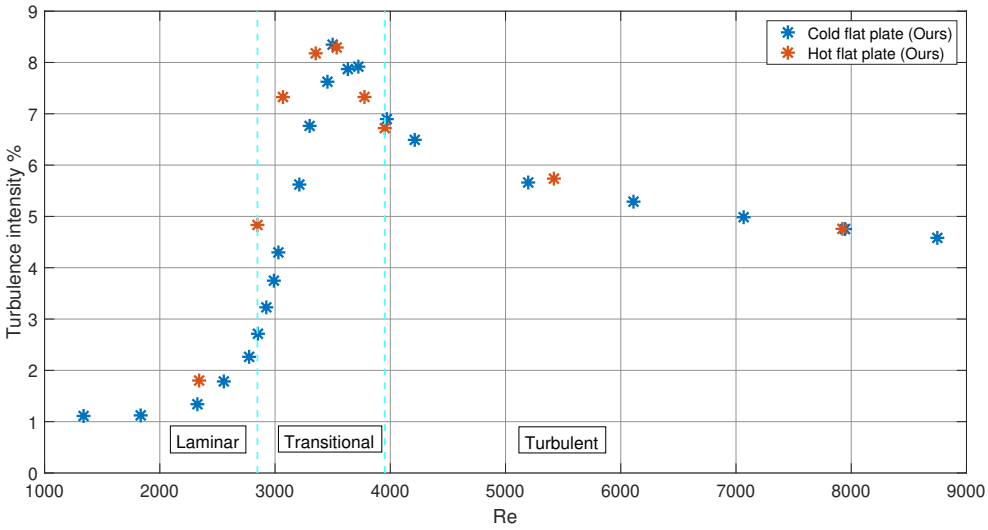

Figure 5.4: Turbulence intensity with respect to Reynolds number for smooth flat surface in cold and hot conditions.

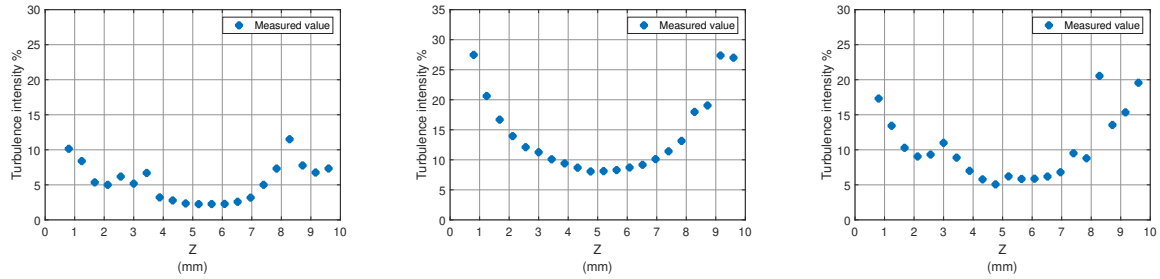

(a) Laminar flow Re = 2341. (b) Transitional flow Re = 3535. (c) Turbulent flow Re = 7924.

Figure 5.5: Turbulence intensity for flat plates in heated condition in the rectangular channel at y = 100 mm for (a) Laminar flow (b) Transitional flow and (c) Turbulent flow.

the resistance to the air flow reduces in the heated condition. Thereby, reducing the friction factor when compared to the cold state. The comparison shows that the measured data does not deviate more than 6.5% when compared to the Blasius correlation for the Reynolds number range.

5.1.4. Nusselt number measurements

The correctness of the Nusselt number data is analysed in the heated state for the smooth flat plate channel and compared with the correlations as detailed in section 2.3. It is found from Figure 5.7 that the results obtained are in the limits of the Nusselt number correlation proposed by Gnielinski up to Reynolds number equal to 3068 and then approaches the theoretical limit of 8.24 as the flow becomes laminar. The comparison shows that the measured data does not deviate more than 6.3%, which is within the uncertainty limits, when compared to the Gnielinski correlation for the Reynolds number range.

A sudden increase in observed in the Nusselt number at the transition from laminar to transitional flow regime. This is due to the increase in turbulence intensity at the onset of transitional flow regime as shown in Figure 5.4. A good agreement between the experimental and predicted data is seen from Figure 5.6 and 5.7, thus ensuring the reliability of the data collected by the experimental setup.

5.2. Dimple-protrusion plate

The agreement of the present results of smooth plate with most reliable correlations gives confidence for the reliability of the experimental method and therefore the results obtained for the staggered dimple-

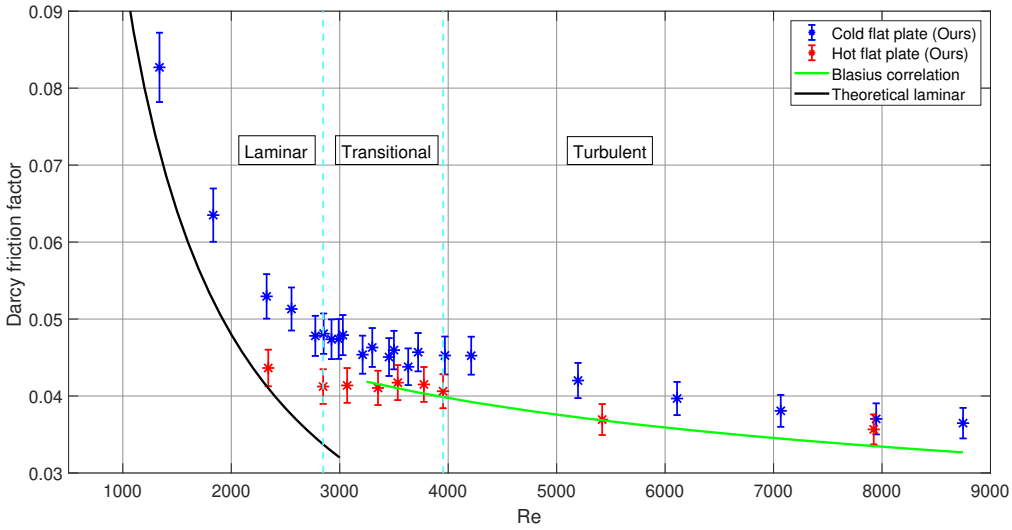

Figure 5.6: Comparison of experimental and predicted data of friction factor with respect to Reynolds number for smooth flat plates.

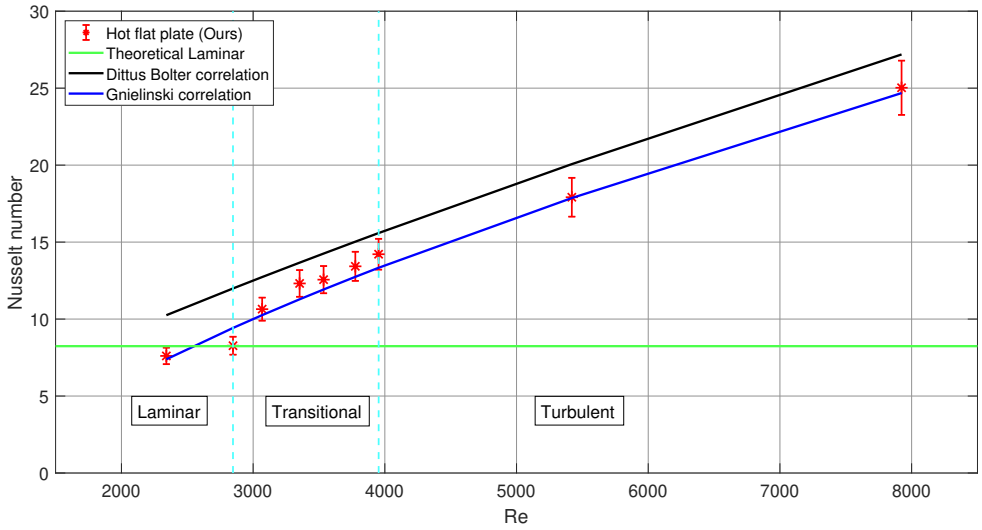

Figure 5.7: Comparison of experimental and predicted data of Nusselt number with respect to Reynolds number for smooth flat plates.

protrusion plate. After performing the experiments with smooth plates, staggered dimple-protrusion plates of thickness t = 1.5 mm were installed in the experimental channel.

5.2.1. Velocity measurements

Figure 5.8 displays the velocity profile for laminar, transitional and turbulent flow regime for the dimple-protrusion plates installed in the channel. The flow follows a parabolic profile in the laminar state and a power law profile with index $n = 7$ for the highest Reynolds number. For the same fan frequency as that for the flat plate, a retardation in the velocity profile is found for the turbulent flow in the channel with dimple-protrusion roughness. The root mean square u-component of the velocity in the centre channel is shown in Figure 5.9. A similar trend is observed as that in the case of flat plates with the lowest fluctuations for laminar flow regime.

Figure 5.10 shows the normalized u component of velocity for the dimple-protrusion plates in the

laminar, transitional and turbulent flow regimes. The velocity profile becomes flat as the velocity of flow increases from laminar to turbulent flow regime. Also, due to conservation of mass, the flow velocity at z = 5 mm is seen to increase in between opposite dimples and decreases in between opposite protrusions. These fluctuations in velocity in the stream-wise and span-wise direction leads to better mixing which in turn helps in improving the rate of heat transfer.

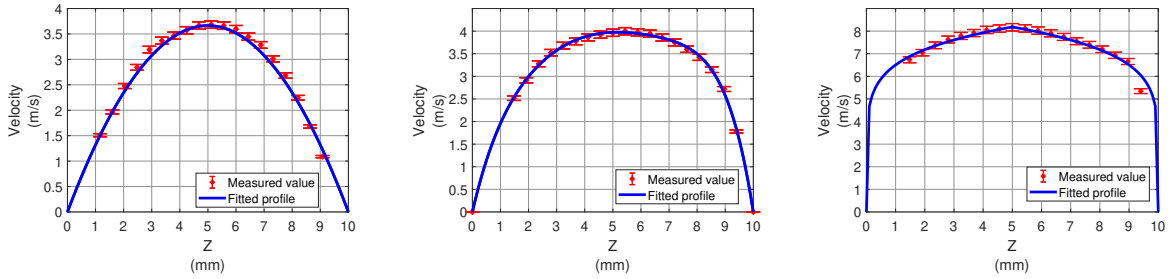

(a) Laminar flow Re = 2418. (b) Transitional flow Re = 3210. (c) Turbulent flow Re = 7626.

Figure 5.8: u-velocity profile for dimple-protrusion plates in a rectangular channel for (a) Laminar flow (b) Transitional flow and (c) Turbulent flow.

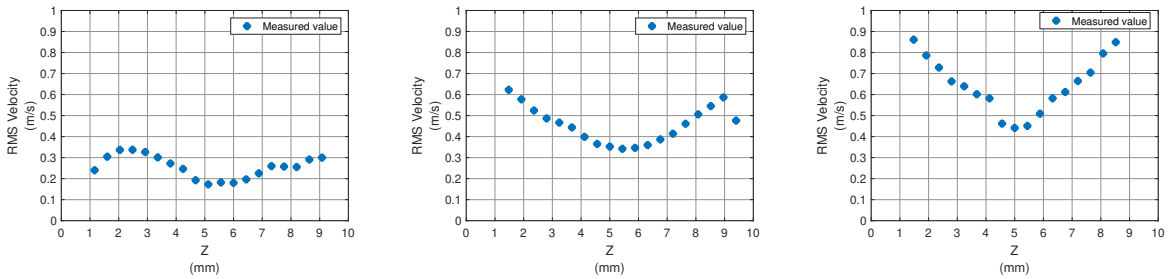

(a) Laminar flow Re = 2418. (b) Transitional flow Re = 3210. (c) Turbulent flow Re = 7626.

Figure 5.9: u_{rms} profile for dimple-protrusion plates in a rectangular channel for (a) Laminar flow (b) Transitional flow and (c) Turbulent flow.

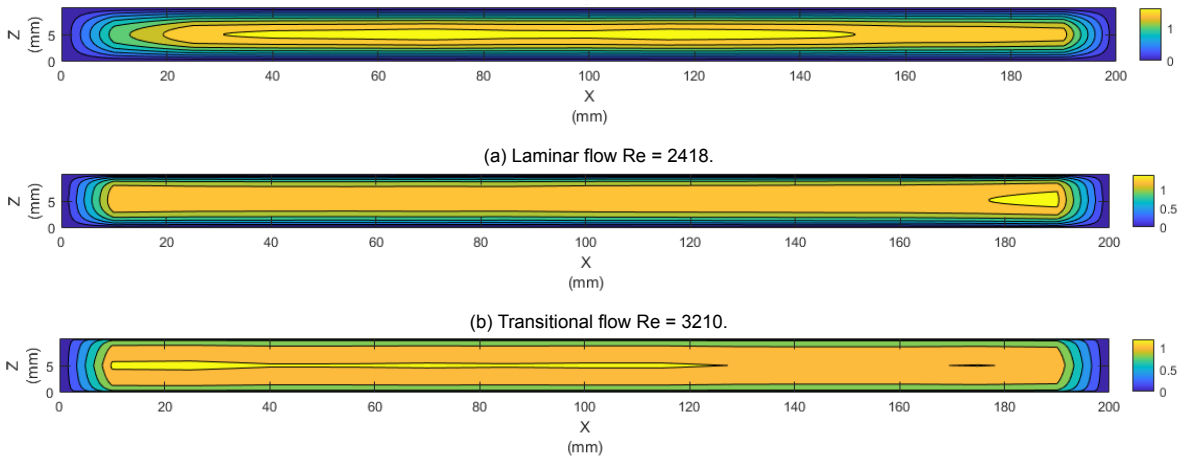

(a) Laminar flow Re = 2418.

(b) Transitional flow Re = 3210.

(c) Turbulent flow Re = 7626.

Figure 5.10: Normalized u-component of velocity u/u_{mean} for dimple-protrusion plates in a rectangular channel for (a) Laminar flow (b) Transitional flow and (c) Turbulent flow.

5.2.2. Turbulence intensity

For surface with dimples and protrusions the onset of transitional and turbulent flow shifts to lower Reynolds numbers as seen from Figure 5.11. The flow is in the laminar regime up to Re = 2586 after that it enters the transition zone with a peak at Re = 3210. It is followed by a decline in the turbulence intensity at Re = 3911 which marks the beginning of turbulent flow. It is also observed that the turbulence intensity of the flow is higher with dimple-protrusion surfaces when compared to smooth flat surfaces. The most increase is observed in the transitional and laminar zone. This implies formation of large number of vortices in the transitional and laminar flow which enhance mixing thereby helps in improving the heat transfer within the fluid.

Figure 5.12 shows the comparison of turbulence intensity across the height of the centre passage for dimple-protrusion surfaces and smooth flat surfaces at y = 100 mm for laminar, transitional and turbulent flow regime. It is seen that the turbulence intensity is lowest at the centre of the passage and increases close to the boundary layer near the walls. The highest difference is observed in the laminar flow regime which is also seen from Figure 5.11.

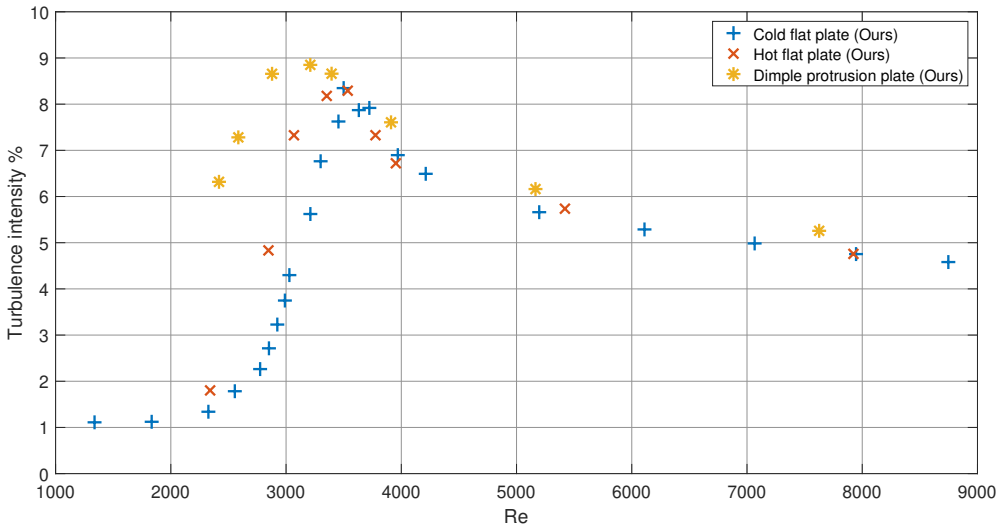

Figure 5.11: Turbulence intensity with respect to Reynolds number for smooth flat surface and dimple-protrusion surface.

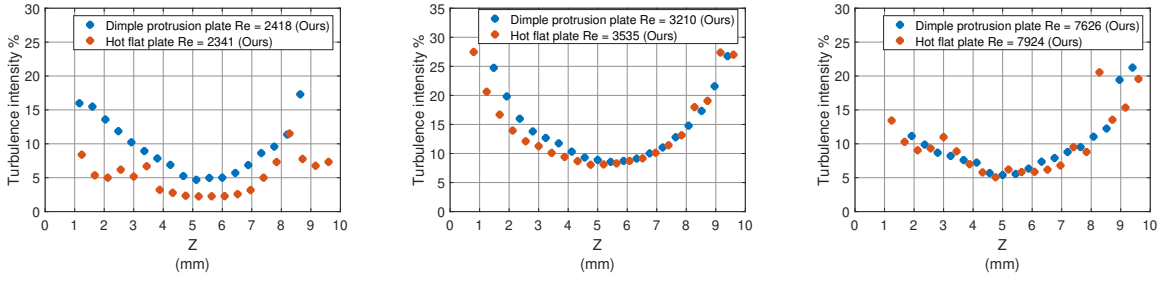

(a) Laminar flow (b) Transitional flow (c) Turbulent flow

Figure 5.12: Comparison of turbulence intensity for dimple-protrusion plates and smooth flat plates in a rectangular channel at y = 100 mm for (a) Laminar flow (b) Transitional flow and (c) Turbulent flow.

5.2.3. Friction factor measurements

Figure 5.13 illustrates the friction factor versus Reynolds number for surface with dimples and protrusions. It is observed that the friction factor decreases with an increase in Reynolds number as expected for fully developed turbulent flows through a channel. It is seen that the introduction of dimple-protrusion

roughness leads to an increase in the pressure loss within the channel which thereby increases the friction factor. This results in an increment in the pumping power required to operate the heat exchanger.

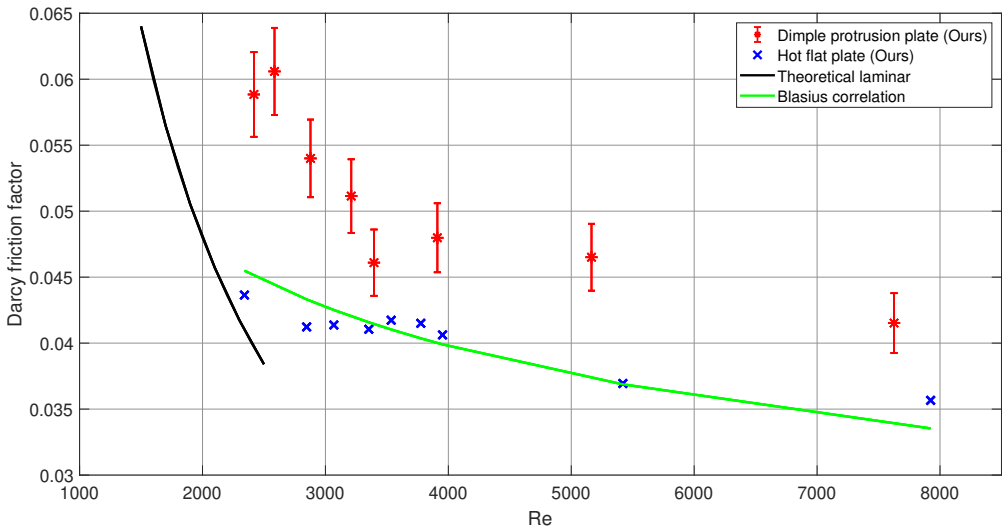

Figure 5.13: Friction factor versus Reynolds number for smooth flat surface and dimple-protrusion surface (heated).

Nikuradse et al. [1950] performed an experimental investigation for turbulent flow of water in pipes with various degrees of relative roughness and proposed the friction similarity law as discussed in section 2.2.1. Figure 5.14 shows the variations in the friction roughness function against roughness Reynolds number for dimple-protrusion roughness surface. Here, the length parameter k is the height of the surface roughness such that k is the height of the dimple or protrusion, $k = 1$ mm. Although, the value of the friction similarity function is higher than the results obtained by Nikuradse et al. [1950], a trend similar to Figure 2.3a is noticed with the dimple-protrusion roughness.

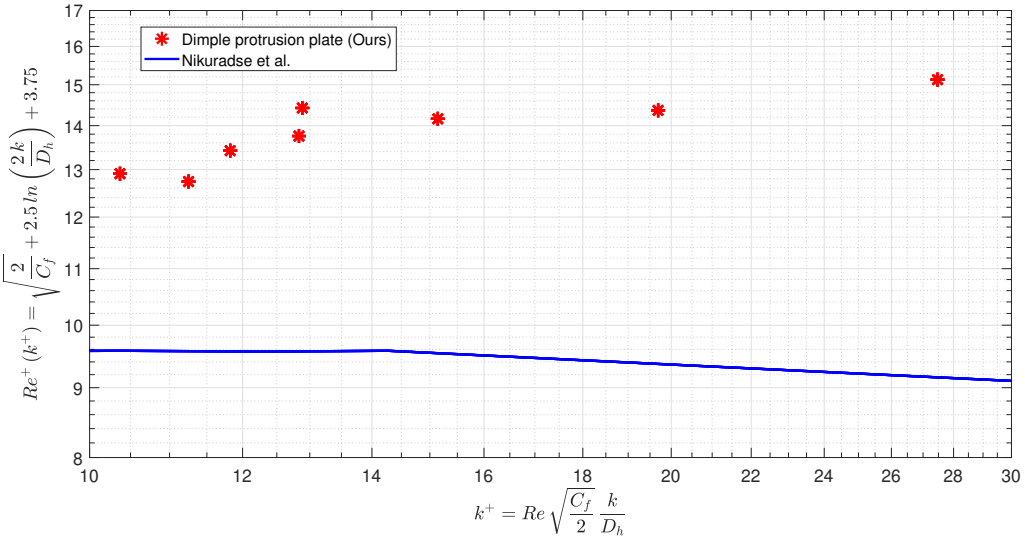

Figure 5.14: Comparison of friction similarity function versus roughness Reynolds number for surfaces with dimple-protrusion roughness with the data obtained by Nikuradse et al. [1950].

5.2.4. Average Nusselt number

Figure 5.15 presents the average Nusselt number for dimple-protrusion surfaces. It is observed that the average Nusselt number increases with an increase in the flow speed. It is also realized that the

introduction of dimple-protrusion surface improves the heat transfer due to the formation of secondary vortices as discussed in section 5.2.5.

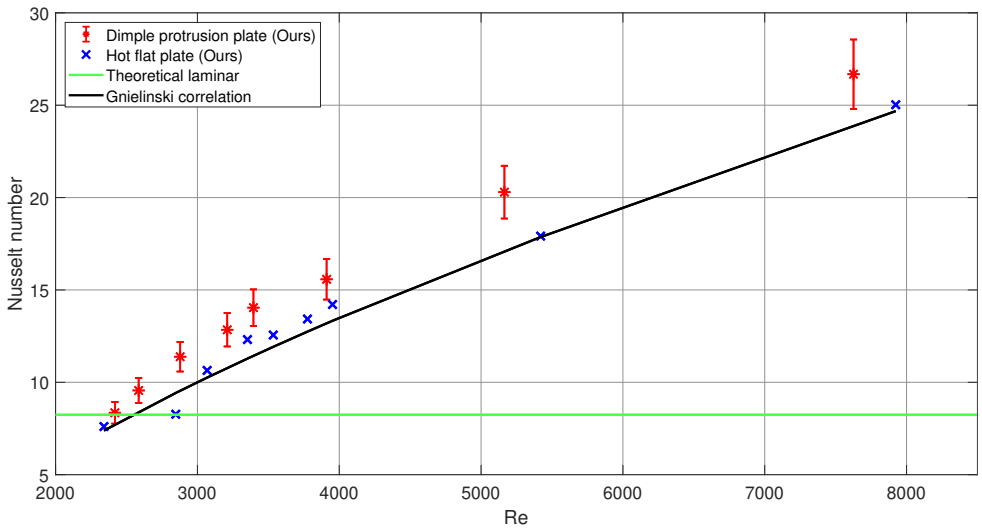

Figure 5.15: Nusselt number versus Reynolds number for smooth flat surface and dimple-protrusion surface.

Dipprey and Sabersky [1963] performed an experimental investigation for turbulent flow of water for a range of Prandtl number Pr = 1.2 - 5.94 and proposed the heat similarity law as discussed in section 2.24. The variation in heat transfer function with roughness Reynolds number for dimple-protrusion surfaces based on this analysis is shown in Figure 5.16. Although, the magnitude of the heat similarity function is higher than the results obtained by Dipprey and Sabersky [1963], a shape similar to Figure 2.5a is noticed for the dimple-protrusion roughness. The difference is explained from the fact that Dipprey and Sabersky [1963] developed the heat similarity function g for fully rough regime in a circular roughened pipe with water having Prandtl number almost twice as large as air. Whereas, the dimple-protrusion type roughness is investigated in a rectangular channel in the transitionally rough flow regime with air as the working medium.

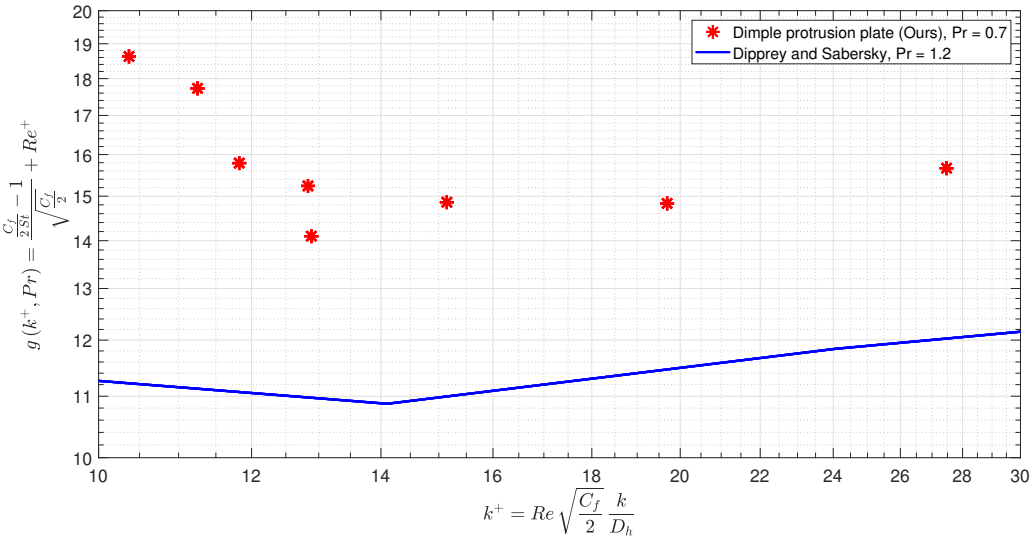

Figure 5.16: Comparison of heat transfer function versus roughness Reynolds number for surfaces with dimple-protrusion roughness with the data obtained by Dipprey and Sabersky [1963].

5.2.5. Local heat transfer characteristics

Figure 5.17 shows a section of the dimple protrusion surface to illustrate the distribution of the local Nusselt number for laminar, transitional and turbulent flow regime. The hot air in the centre channel flows from left to right. The dotted red circles indicate a dimple while the solid black circles refer to a protrusion. The temperature field explains the fact that various recirculation zones appear in the channel when the surface is introduced with dimple and protrusion roughness. These recirculation zones are responsible for the augmentation of the heat transfer coefficient.

It is seen from Figure 5.17 that in case of a dimple, the flow separates and a recirculation region is formed in the upstream half which leads to a region of low heat transfer as explained in section 1.2. In the downstream half of the dimple the heat transfer is enhanced due to flow impingement, reattachment and up wash flow. Whereas for a protrusion, a high heat transfer zone is formed at the upstream half due to the main flow impingement, thickening of boundary layer and formation of horse shoe vortices. The flow separates in the downstream half of the protrusion which creates a low heat transfer zone. Also, the interaction of the vortices from the opposite dimple-protrusion surface affects the enhancement of heat transfer. The intermediate region between the rear side of a protrusion and the front side of a dimple has relatively low heat transfer, due to separation of the flow by the protrusion and recirculation of the flow at the upstream of the dimple. The results obtained are found to be similar to the numerical study conducted by Chen et al. [2014] over periodically dimple-protrusion patterned wall as shown in Figure 1.3.

Figure 5.17a displays the variation of local Nusselt number in the laminar flow regime. It is found that a high heat transfer region exists on most part of the protrusion and the flow separation takes place towards the end of the rear side. While for the dimple, at low speeds the effect of flow impingement is weaker and the recirculation region is wider thereby reducing the Nusselt for most part of the dimple. On the other hand, in the turbulent flow regime, it can be seen from Figure 5.17c that for a protrusion the area of high heat transfer reduces and the flow separates earlier than that in the case of the laminar flow. At the same time, for the dimple the area of high heat transfer increases with an increase in flow speed due to an early impingement of flow near the centerline of the dimple.

Figure 5.18 displays the section and Figure 5.19 shows the variation in the local Nusselt number from the mean value in the stream-wise ($y/d = 0$) and span-wise ($x/d = 0$) direction for a pair of dimple and protrusion. It is observed from Figure 5.19 that the variations in the local Nusselt number from the mean is low for laminar flow regime and increases as the flow becomes turbulent. It is seen that due to the orientation of the dimples and protrusions, local peaks in Nusselt number are observed in the front section of a protrusion and rear section of a dimple in the stream-wise direction. Whereas in the span-wise direction, local peaks in Nusselt number are observed on the top side of a dimple and bottom side of a protrusion. A trend similar to the experimental results by Hwang et al. [2010] is observed in the stream-wise local Nusselt number distribution.

5.3. Comparison

This section compares the results obtained for dimple-protrusion surfaces with respect to smooth flat surface in heated conditions based on normalized friction factor, normalized Nusselt number, overall heat transfer coefficient and performance factor.

5.3.1. Normalized friction factor

Figure 5.20 displays the normalized friction factor versus Reynolds number for dimple-protrusion surfaces. The reference friction factor f_0 for normalization is obtained from the experiment with smooth flat surfaces. It is observed that the friction factor rises with respect to smooth surfaces. A larger impact is noticed in the transitional and laminar flow due to increase in the fluctuations and turbulence intensity. Thus, increasing the pressure loss at low Reynolds numbers.

5.3.2. Normalized Nusselt number

Figure 5.21 illustrates the normalized Nusselt number versus Reynolds number for dimple-protrusion surfaces. The reference Nusselt number Nu_0 for normalization is obtained from the experiment with smooth flat plates. It is seen that the performance increases with the introduction of dimple-protrusion

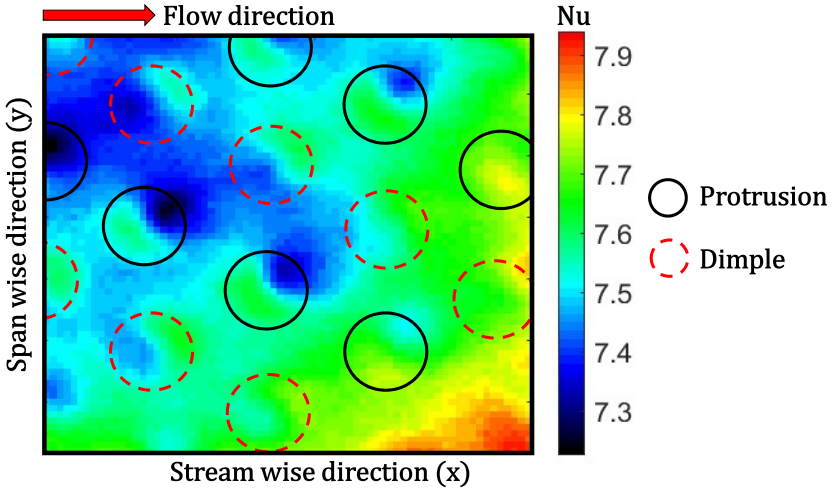

(a) Variations in the local Nusselt number for laminar flow regime at Re = 2418

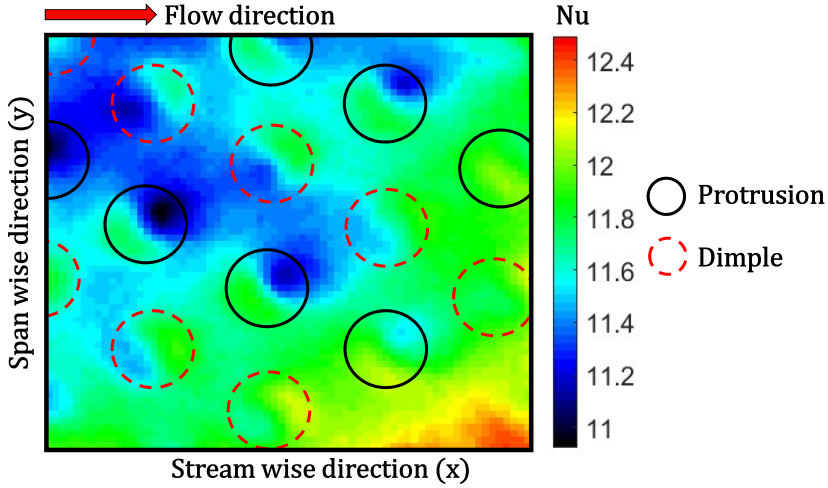

(b) Variations in the local Nusselt number for transitional flow regime at Re = 3210.

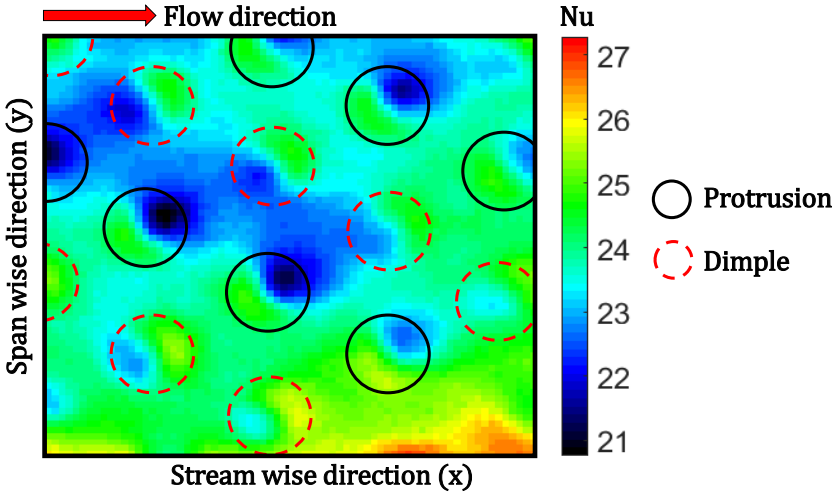

(c) Variations in the local Nusselt number for turbulent flow regime at Re = 7626.

Figure 5.17: Local Nusselt number distribution for dimple protrusion surface for laminar, transitional and turbulent flow regime. Dotted red circle refers to dimples and solid black circle refers to protrusions. The hot air flow direction is from left to right.

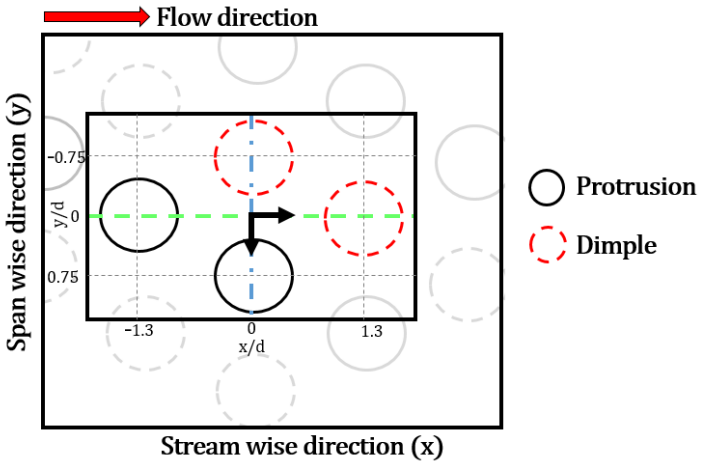

Figure 5.18: Location for measurement of local Nusselt number in stream-wise ($y/d = 0$) and span-wise ($x/d = 0$) direction.

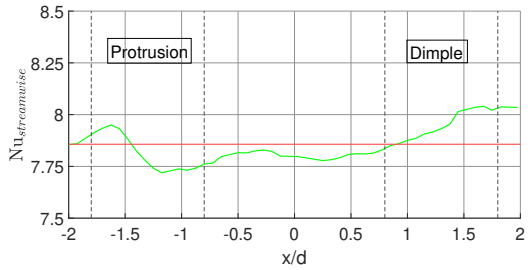

(a) Variation in local Nusselt number in the stream wise direction for laminar flow at Re = 2418.

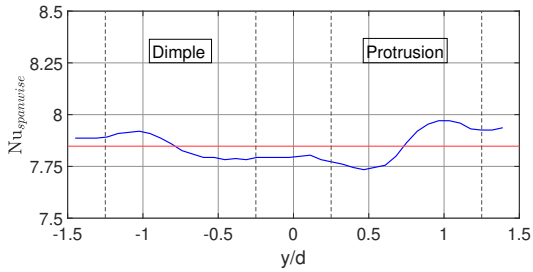

(b) Variation in local Nusselt number in the span wise direction for laminar flow at Re = 2418.

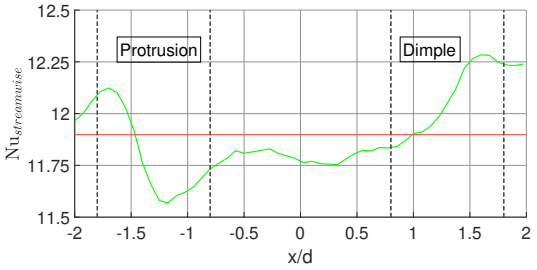

(c) Variation in local Nusselt number in the stream wise direction for transitional flow at Re = 3210.

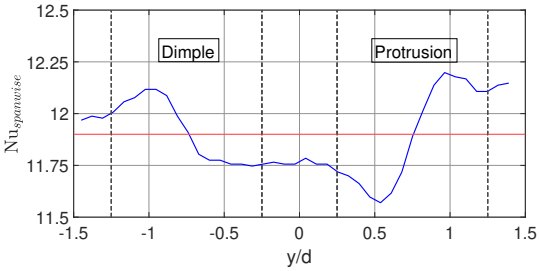

(d) Variation in local Nusselt number in the span wise direction for transitional flow at Re = 7626.

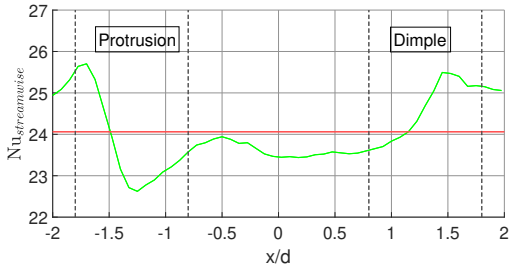

(e) Variation in local Nusselt number in the stream wise direction for turbulent flow at Re = 7626.

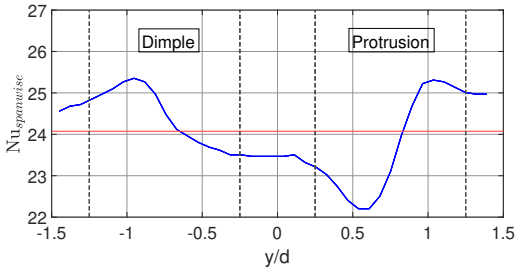

(f) Variation in local Nusselt number in the span wise direction for turbulent flow at Re = 7626.

Figure 5.19: Variation in local Nusselt number in the stream-wise ($y/d = 0$) and span-wise ($x/d = 0$) direction for a pair of dimple and protrusion. Red solid line represents the mean Nusselt number.

roughness. The highest enhancement in heat transfer relative to the smooth flat plates Nu/Nu_0 = 1.324 is observed in the transitional flow regime at a Reynolds number of 2878.

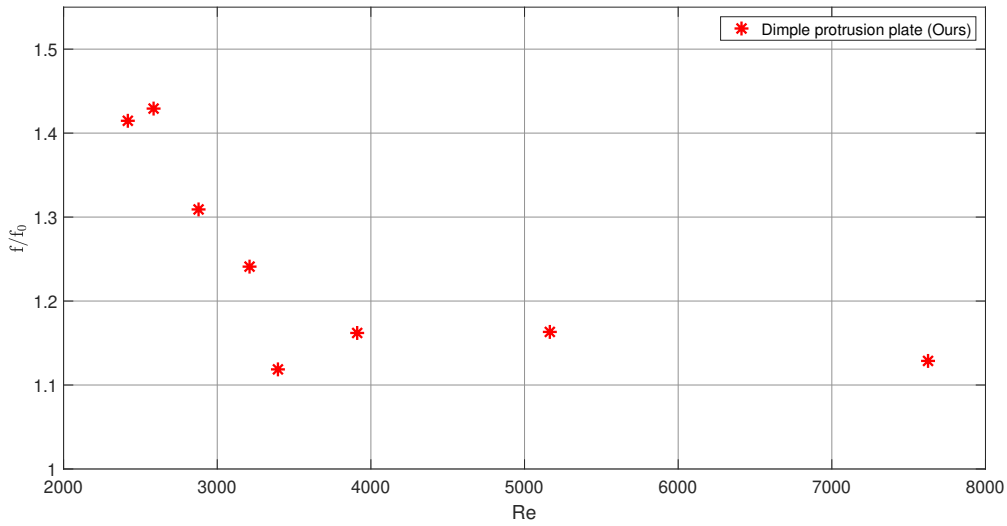

Figure 5.20: Normalized friction factor versus Reynolds number for dimple-protrusion surface.

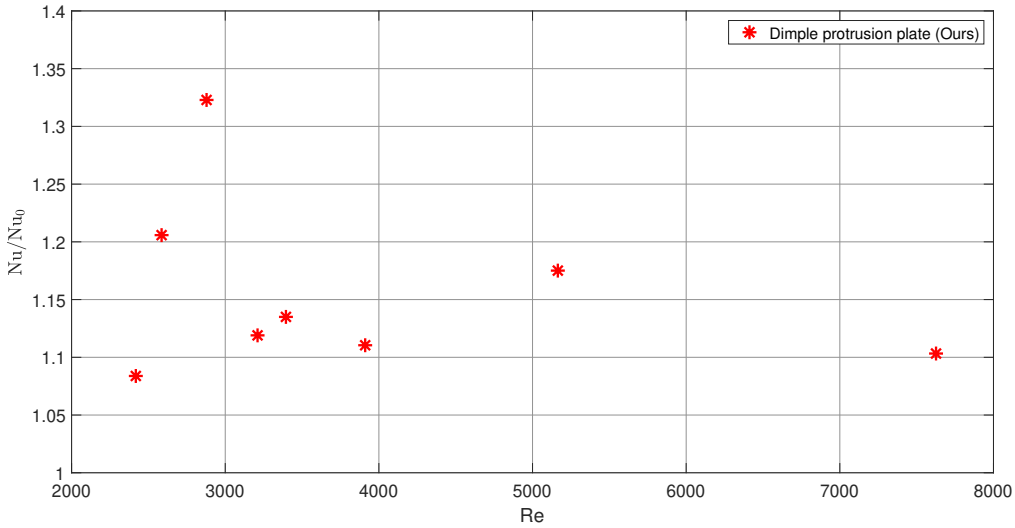

Figure 5.21: Normalized Nusselt number versus Reynolds number for dimple-protrusion surface.

5.3.3. Overall heat transfer coefficient

The overall heat transfer coefficient based on logarithmic mean temperature difference as discussed in section 4.1.5 is shown in Figure 5.22. The overall heat transfer coefficient increases with the increase in Reynolds number. The maximum enhancement of 31.75% is observed in the transitional flow regime for the Reynolds number of 2878 which is also seen in Figure 5.21.

5.3.4. Performance factor

Heat transfer rate and surface area are important to compare the performance of a heat exchanger. It is also necessary to account for pressure loss related to pumping power as pressure loss generally increases with the increase in heat transfer. Hence, the performance factor is a good measure to compare the efficacy of a heat exchanger as it considers both the heat transfer enhancement and the pressure loss increment.

Figure 5.23 shows the volume goodness factor and the performance factor versus Reynolds number for the flat surface and the dimple-protrusion surface. This improvement in performance is due to the

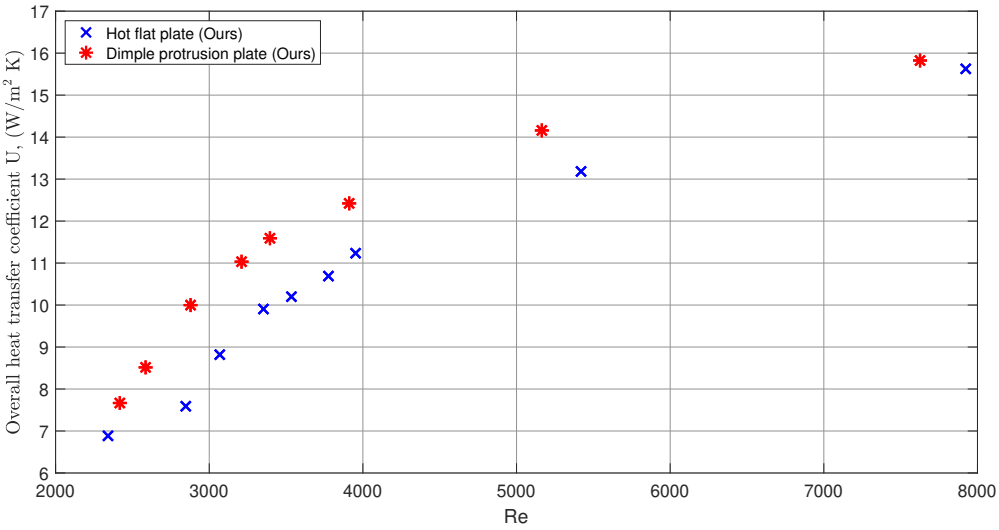

Figure 5.22: Comparison of the overall heat transfer coefficient with respect to Reynolds number for smooth flat surface and dimple-protrusion surface.

effect of induced vortices from the dimples and protrusions. For the dimple-protrusion surfaces, the highest volume goodness factor of 0.01625 is found to be at Re = 3395. However, the maximum improvement in performance of the heat exchanger is observed at Re = 2878 with η = 1.21.

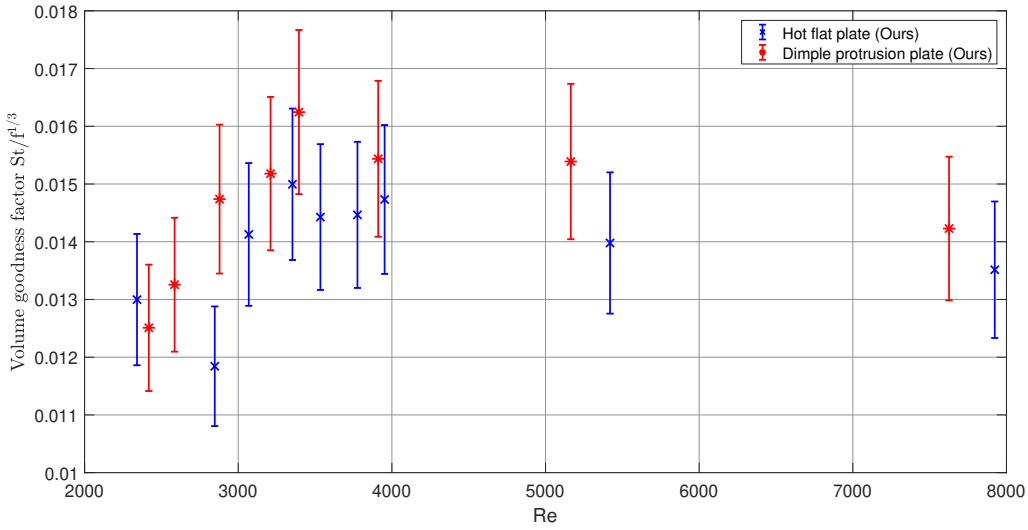

Figure 5.23: Volume goodness factor versus Reynolds number for flat surface and dimple-protrusion surface.

5.4. Discussion

Performing analysis on the measured data obtained for a counter flow smooth-flat plate and dimple-protrusion plate heat exchanger provide the following key results:

- For dimple-protrusion roughness surface the friction similarity law and the heat similarity law with respect to the roughness Reynolds number show a similar shape when compared to the results obtained by Nikuradse et al. [1950] and Dipprey and Sabersky [1963]. The results obtained in Figure 5.14 show that Re^+ is nearly constant in the range of 10 > k^+ > 30. However, the values obtained for the dimple-protrusion plate is almost 50 % higher than the values reported

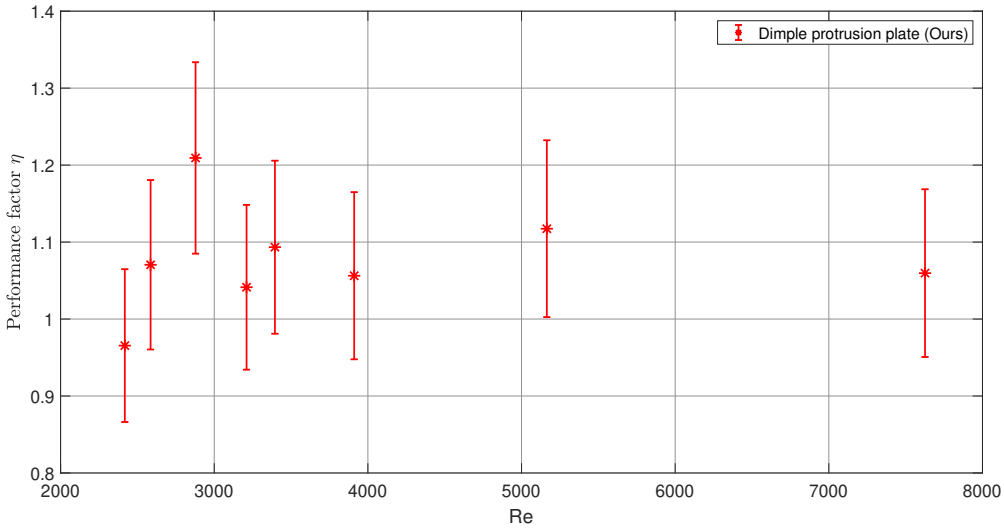

Figure 5.24: Performance factor number versus Reynolds number for dimple-protrusion surface.

by Nikuradse et al. [1950]. Similarly, from Figure 5.16 it is seen that the heat transfer function g has a similar shape with an increase in magnitude when compared to the results obtained by Dipprey and Sabersky [1963]. The difference can be due to the fact that the data obtained by Nikuradse et al. [1950] and Dipprey and Sabersky [1963] is for roughened circular tubes with water as operating fluid, with Prandtl number almost twice as that of air, in the fully rough regime ($k^+ > 60$). Whereas, the dimple-protrusion type of roughness is investigated in a rectangular channel, with air as the working medium, for the transitionally rough flow regime ($5 > k^+ > 60$). Thus, this shows that different correlations are necessary for the combination of low Reynolds numbers and transitionally rough flow regime.

- The variation in local Nusselt number is found to be similar to the experimental results obtained by Hwang et al. [2010] and numerical results obtained by Chen et al. [2014]. Peaks in Nusselt number are observed in the upstream half of a protrusion due to flow impingement and downstream half of a dimple due to flow reattachment. Whereas, valleys in Nusselt number are observed in the downstream half of the protrusion and upstream half of a dimple due to flow separation.
- For applications where the flow speed is critical and the heat exchanger is required to operate in the transitional or early turbulent flow regime, a dimple-protrusion plate type heat exchanger can provide higher heat transfer for the same volume when compared to flat plate type heat exchangers.
- The performance with the shallow dimple-protrusion plate heat exchanger is found to increase by 21 % at Re = 2878 and by almost 10 % in the turbulent regime when compared to the smooth flat plate heat exchanger. Therefore, to achieve the same heat transfer, the dimple-protrusion heat exchanger will be compact and smaller in size thereby reducing, the space occupied and the weight of the heat exchanger.

6

Conclusion

The goal of this study was to understand the behaviour of the flow when subjected to a surface with dimples and protrusions, with an intention of using this understanding to improve the performance of a plate type heat exchanger. We started this study as an endeavour to answer the following research questions:

1. How does the performance factor change due to the introduction of dimple and protrusion surfaces in a plate type heat exchanger?
2. Can the onset of transitional and turbulent flow be shifted to lower Reynolds number?

In order to throw light on future advancements in the field of passive enhancement techniques and answer the above mentioned research questions:

- A laboratory scale setup of a counter flow heat exchanger was designed and built.
- Quantitative visualization of the local surface temperature was obtained using Infrared thermography.
- Flow analyses were performed using Laser Doppler Anemometry for air as the working medium in a range of Re = 1500 - 9000.

The heat transfer characteristics on the dimple-protrusion patterned surfaces obtained in the present study are summarized as follows:

Heat transfer enhancements

Regions of high heat transfer appear on the front part of the protrusion and on the rear part for a dimple. The normalized Nusselt number is higher for low Reynolds numbers due to the stronger strength of the induced secondary vortices at low speeds. For the staggered dimple-protrusion plate the highest normalized Nusselt number of 1.32 is obtained at Re = 2878.

Pressure drop and performance factor

Introduction of dimple-protrusion roughness leads to a rise in the friction factor as compared with the flat plates. This results in an increased pressure drop. The performance factor is high at low Reynolds numbers in the transitional region due to the improvement in heat transfer. The maximum volume goodness factor of 0.01625 is found at Re = 3395 while the highest performance factor of η = 1.21, is obtained at Re = 2878.

Onset of transitional and turbulent flow

For the staggered orientation, the onset of transitional and turbulent flow shifts to lower Reynolds numbers when compared to smooth-flat surfaces. For smooth flat plate heat exchanger the flow enters transitional flow regime at Re = 2847 and turbulent flow regime at Re = 3953. While, the flow regime changes from laminar to transitional at Re = 2586 and to turbulent at Re = 3911 for dimple-protrusion plate heat exchanger.

7

Outlook

Due to the limited time frame and scope of the current study, we were unable to delve into many facets and interesting phenomena. In this chapter we briefly describe a few recommendations for future research.

- The present work focused on staggered orientation of spherical dimple-protrusions surfaces. However, it is also interesting to study the effect of inline orientation with change in the relative roughness height and pitch. Thus, helping in development of a good correlation to predict the Nusselt number and friction factor.
- Also, in the current study the shape of the dimple and protrusion is spherical. Nevertheless, different shapes and configurations such as tear drop, elliptical, oval etc. can be investigated with the existing set-up.
- For the experimentation, a constant air flow is maintained in the cold channel. However with further testing, the effect of different air speeds in the cold and hot channels can be investigated to determine the optimal operating range.
- The temperature inside the hot channel is measured with the help of K-type thermocouples at 5 locations across the height and a 4^{th} order interpolation curve fit is applied to estimate the temperature profile. Instead the temperature profile can be measured accurately by using cold wire probe measurement technique.
- In order to further investigate the uniformity of the flow in the transitional flow regime, instantaneous flow velocity and temperature measurements can be conducted using Thermographic Particle Image Velocimetry (TPIV).
- It is observed that the transmissivity of the FLIR inspection window changes with the change in surface temperature and can lead to measurement errors. Thus, germanium or zinc selenide optical window should be used to improve the quality of the measurements.

Bibliography

Abdulhameed, J. J., Saad, D., and S Kassim, M. (2019). Effect of baffles geometry on heat transfer enhancement inside corrugated duct. *International Journal of Mechanical Engineering and Technology*, 10(3).

Ahn, S. W. and Son, K. P. (2002). An investigation on friction factors and heat transfer coefficients in a rectangular duct with surface roughness. *KSME international journal*, 16(4):549–556.

Amalfi, R. L. and Thome, J. R. (2016a). High resolution infrared measurements of single-phase flow of r245fa and r236fa within a compact plate heat exchanger, part 1: Experimental setup and pressure drop results. *Applied Thermal Engineering*, 101:545–554.

Amalfi, R. L. and Thome, J. R. (2016b). High resolution infrared measurements of single-phase flow of r245fa and r236fa within a compact plate heat exchanger, part 2: Heat transfer results. *Applied Thermal Engineering*, 101:555–563.

Aupoix, B. (2015). Improved heat transfer predictions on rough surfaces. *International Journal of Heat and Fluid Flow*, 56:160–171.

Bhushan, B. and Singh, R. (2011). Nusselt number and friction factor correlations for solar air heater duct having artificially roughened absorber plate. *Solar energy*, 85(5):1109–1118.

Caliskan, S. (2014). Experimental investigation of heat transfer in a channel with new winglet-type vortex generators. *International Journal of Heat and Mass Transfer*, 78:604–614.

Caliskan, S., Dogan, A., and Kotcioglu, I. (2019). Experimental investigation of heat transfer from different pin fin in a rectangular channel. *Experimental Heat Transfer*, 32(4):376–392.

Chang, S., Cai, W.-L., and Wu, R.-J. (2018). Heat transfer enhancement by detached s-ribs for twin-pass parallelogram channel. *Inventions*, 3(3):50.

Chang, S. W., Chen, T. W., and Chen, Y. W. (2019). Detailed heat transfer and friction factor measurements for square channel enhanced by plate insert with inclined baffles and perforated slots. *Applied Thermal Engineering*, 159:113856.

Chedevergne, F. (2018). Analytical wall function including roughness corrections. *International Journal of Heat and Fluid Flow*, 73:258–269.

Chedevergne, F. and Aupoix, B. (2017). Accounting for wall roughness effects in turbulence models: a wall function approach. In *7th EUCASS conference*.

Chen, Y., Chew, Y., and Khoo, B. (2014). Heat transfer and flow structure on periodically dimple–protrusion patterned walls in turbulent channel flow. *International Journal of Heat and Mass Transfer*, 78:871–882.

Chen, Y., Chew, Y. T., and Khoo, B. C. (2012). Enhancement of heat transfer in turbulent channel flow over dimpled surface. *International Journal of Heat and Mass Transfer*, 55(25-26):8100–8121.

Dipprey, D. F. and Sabersky, R. H. (1963). Heat and momentum transfer in smooth and rough tubes at various prandtl numbers. *International Journal of Heat and Mass Transfer*, 6(5):329–353.

Figliola, R. S. and Beasley, D. E. (2001). Theory and design for mechanical measurements.

Flack, K. A., Schultz, M. P., Barros, J. M., and Kim, Y. C. (2016). Skin-friction behavior in the transitionally-rough regime. *International Journal of Heat and Fluid Flow*, 61:21–30.

Hwang, S. D., Kwon, H. G., and Cho, H. H. (2008). Heat transfer with dimple/protrusion arrays in a rectangular duct with a low reynolds number range. *International Journal of Heat and Fluid Flow*, 29(4):916–926.

Hwang, S. D., Kwon, H. G., and Cho, H. H. (2010). Local heat transfer and thermal performance on periodically dimple-protrusion patterned walls for compact heat exchangers. *Energy*, 35(12):5357–5364.

Incropera, F. P., Lavine, A. S., Bergman, T. L., and DeWitt, D. P. (2007). *Fundamentals of heat and mass transfer*. Wiley.

Ingole, N. W. and Shelke, P. R. S. (2016). Methods of heat transfer enhancement using different surfaces inserts : A review mr .

Johl, G., Passmore, M., and Render, P. (2007). Design and performance of thin, circular arc, wind-tunnel turning vanes. *The Aeronautical Journal*, 111(1116):115–118.

Kiran, K., Asalammaraja, M., and Umesh, C. (2014). A review on effect of various types of tube inserts on perfomance parameters of heat exchanger. *Int J Res Advent Technol E*, 2:127–32.

Kumar, A., Kumar, R., Maithani, R., Chauhan, R., Sethi, M., Kumari, A., Kumar, S., and Kumar, S. (2017a). Correlation development for nusselt number and friction factor of a multiple type v-pattern dimpled obstacles solar air passage. *Renewable Energy*, 109:461–479.

Kumar, R., Sethi, M., Chauhan, R., and Kumar, A. (2017b). Experimental study of enhancement of heat transfer and pressure drop in a solar air channel with discretized broken v-pattern baffle. *Renewable energy*, 101:856–872.

Ligrani, P., Mahmood, G., Harrison, J., Clayton, C., and Nelson, D. (2001). Flow structure and local nusselt number variations in a channel with dimples and protrusions on opposite walls. *International Journal of Heat and Mass Transfer*, 44(23):4413–4425.

Lindgren, B., Österlund, J., and Johansson, A. V. (1998). Measurement and calculation of guide vane performance in expanding bends for wind-tunnels. *Experiments in fluids*, 24(3):265–272.

Ma, J., Huang, Y. P., Huang, J., Wang, Y. L., and Wang, Q. W. (2010). Experimental investigations on single-phase heat transfer enhancement with longitudinal vortices in narrow rectangular channel. *Nuclear Engineering and Design*, 240(1):92–102.

MacDonald, M., Hutchins, N., and Chung, D. (2019). Roughness effects in turbulent forced convection. *Journal of Fluid Mechanics*, 861:138–162.

Mahmood, G., Hill, M., Nelson, D., Ligrani, P., Moon, H.-K., and Glezer, B. (2000). Local heat transfer and flow structure on and above a dimpled surface in a channel. *J. Turbomach.*, 123(1):115–123.

Mills, A. F. (1999). *Basic heat and mass transfer*. Prentice hall.

Moffat, R. J. (1988). Describing the uncertainties in experimental results. *Experimental thermal and fluid science*, 1(1):3–17.

Nazari, S., Zamani, M., and Moshizi, S. A. (2018). Comparative study on the influence of depth, number and arrangement of dimples on the flow and heat transfer characteristics at turbulent flow regimes. *Heat and Mass Transfer*, 54(9):2743–2760.

Nikuradse, J. et al. (1950). Laws of flow in rough pipes.

Peeters, J. and Sandham, N. (2019). Turbulent heat transfer in channels with irregular roughness. *International Journal of Heat and Mass Transfer*, 138:454–467.

Promvonge, P. and Skullong, S. (2019). Enhanced heat transfer in rectangular duct with punched winglets. *Chinese Journal of Chemical Engineering*.

Rao, Y., Feng, Y., Li, B., and Weigand, B. (2015). Experimental and numerical study of heat transfer and flow friction in channels with dimples of different shapes. *Journal of Heat Transfer*, 137(3):031901.

Rao, Y., Wan, C., and Xu, Y. (2012). An experimental study of pressure loss and heat transfer in the pin fin-dimple channels with various dimple depths. *International journal of heat and mass transfer*, 55(23-24):6723–6733.

Rao, Y. and Zhang, P. (2019). Experimental study of heat transfer and pressure loss in channels with miniature v rib-dimple hybrid structure. *Heat Transfer Engineering*, pages 1–11.

Rashidi, S., Hormozi, F., Sundén, B., and Mahian, O. (2019). Energy saving in thermal energy systems using dimpled surface technology–a review on mechanisms and applications. *Applied Energy*, 250:1491–1547.

Singh, P., Pandit, J., and Ekkad, S. V. (2017). Characterization of heat transfer enhancement and frictional losses in a two-pass square duct featuring unique combinations of rib turbulators and cylindrical dimples. *International Journal of Heat and Mass Transfer*, 106:629–647.

Tauscher, R. and Mayinger, F. (1999). Heat transfer enhancement in a plate heat exchanger with rib-roughened surfaces. In *Heat Transfer Enhancement of Heat Exchangers*, pages 207–221. Springer.

Thakkar, M., Busse, A., and Sandham, N. (2018). Direct numerical simulation of turbulent channel flow over a surrogate for nikuradse-type roughness. *Journal of Fluid Mechanics*, 837.

Troniewski, L. and Ulbrich, R. (1984). Two-phase gas-liquid flow in rectangular channels. *Chemical engineering science*, 39(4):751–765.

Won, S. and Ligrani, P. (2007). Flow characteristics along and above dimpled surfaces with three different dimple depths within a channel. *Journal of mechanical science and technology*, 21(11):1901.

Xie, G., Liu, J., Ligrani, P. M., and Zhang, W. (2013). Numerical analysis of flow structure and heat transfer characteristics in square channels with different internal-protruded dimple geometrics. *International journal of heat and mass transfer*, 67:81–97.

Yadav, S., Kaushal, M., et al. (2013). Nusselt number and friction factor correlations for solar air heater duct having protrusions as roughness elements on absorber plate. *Experimental Thermal and Fluid Science*, 44:34–41.

A

Calibration

A.1. Calibration curves of the pressure transducers

The procedure to calibrate the Omega PXM409 Pressure Transducers using Betz manometer is as follows:

1. Connect the pressure transducer cable to the data acquisition module which is connected to a computer with the software instruNet [1].
2. Connect the pressure transducer and the Betz manometer with rubber hoses to a T joint. The third end of the T joint is kept open to change the pressure.
3. Adjust the zero level of the Betz manometer using the screw above the optical display.
4. Zero calibrate the pressure transducers.
5. Set the sampling rate to 100 Hz and the measurement time period to 10 seconds.
6. Record the pressure readings at steady state for 0 mm of water column.
7. Increase the pressure in steps of 10 mm of water column by blowing air through the third end of the T joint and record the pressure in steady state till 240 mm of water column.

The post processing of the pressure data is carried out in MATLAB® version R2019b. The calibration curve for the pressure transducers is shown in Figure A.1

A.2. Calibration curves of the thermocouples

The calibration curves for the air thermocouples with respect to the temperature controlled water bath is shown in Figure A.2

A.3. Calibration of the FLIR inspection window

Figure A.3 shows the value of the transmissivity for the FLIR inspection window with respect to the surface temperature for the aluminium sheet fixed to the uniformly heated aluminium block. Figure A.4 and A.5 show the value of transmissivity of the inspection window versus surface temperature for the flat plate and dimple-protrusion plate while conducting the experiments.

[1] instruNET data acquisition:
http://www.gwinst.com/software/iw/index.html

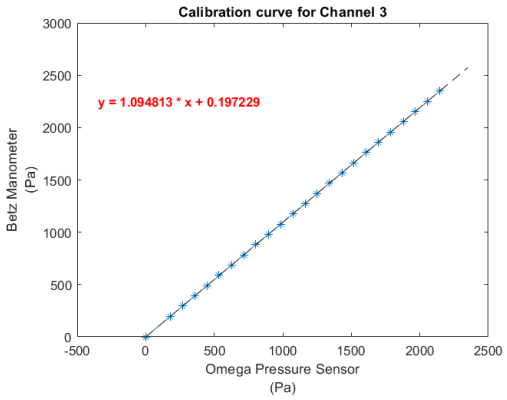

(a) Static Pressure calibration curve at location P1.

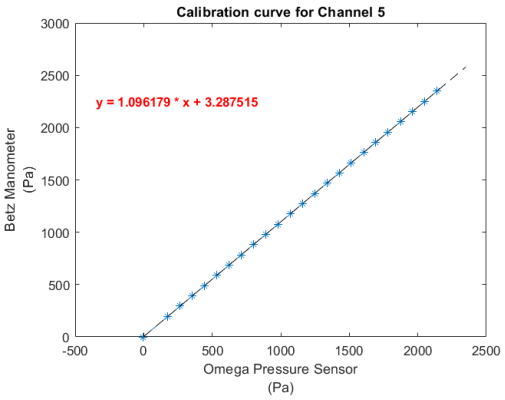

(b) Static Pressure calibration curve at location P2.

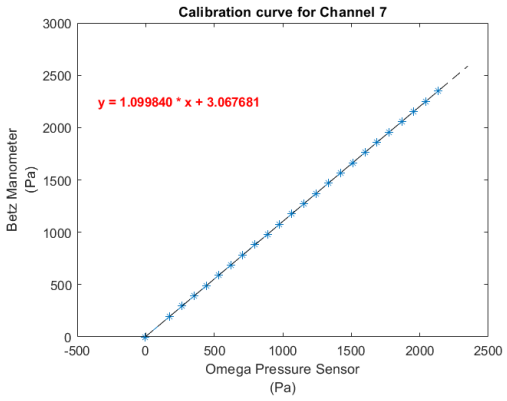

(c) Static Pressure calibration curve at location P3.

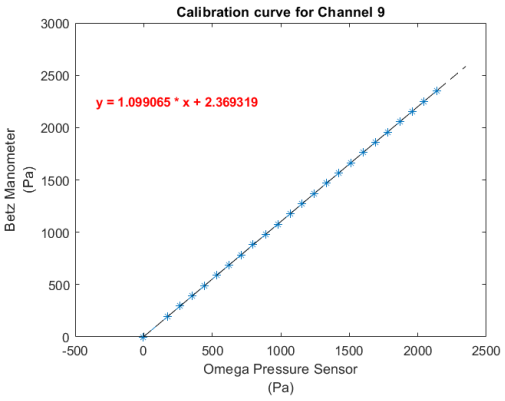

(d) Static Pressure calibration curve at location P4.

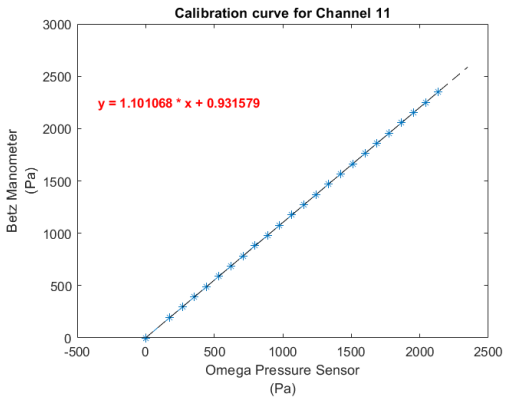

(e) Static Pressure calibration curve at location P5.

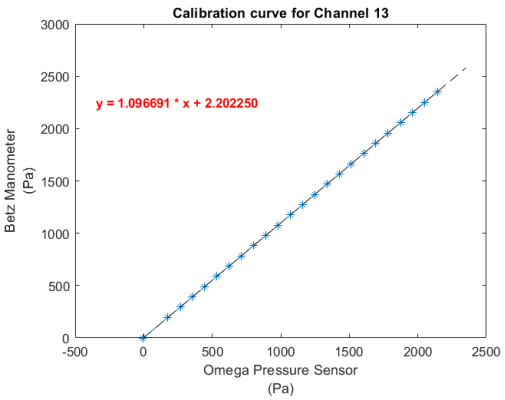

(f) Static Pressure calibration curve at location P6.

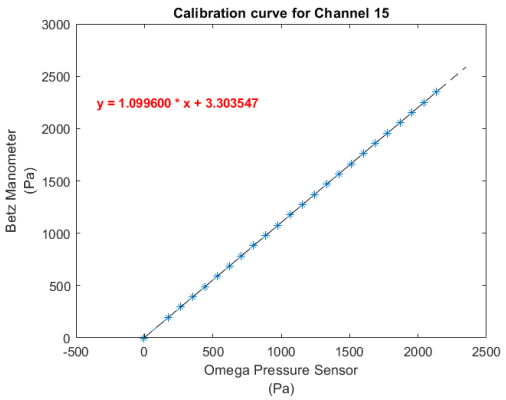

(g) Static Pressure calibration curve at location P7.

Figure A.1: Calibration curves for static pressure measurement.

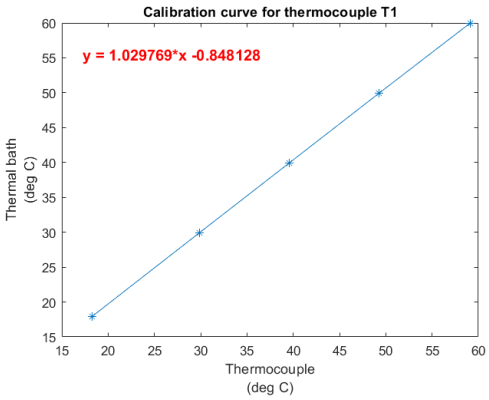

(a) Calibration curve for thermocouple T1.

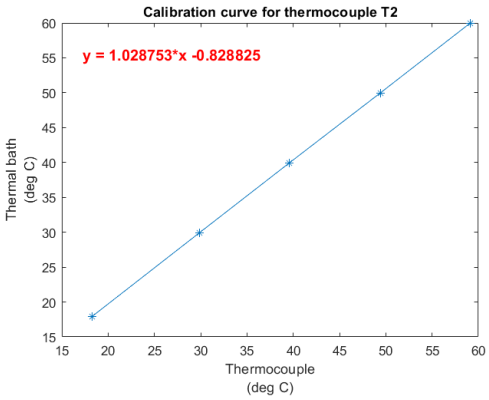

(b) Calibration curve for thermocouple T2.

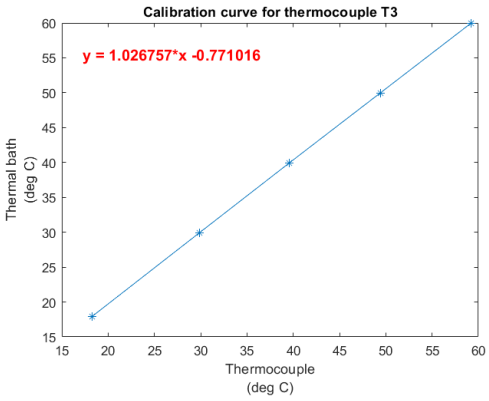

(c) Calibration curve for thermocouple T3.

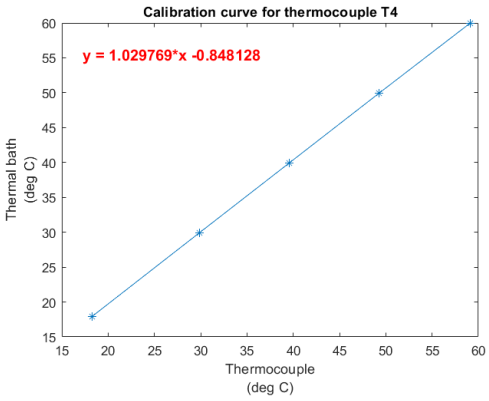

(d) Calibration curve for thermocouple T4.

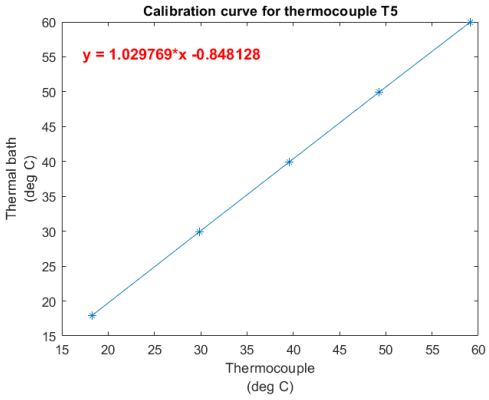

(e) Calibration curve for thermocouple T5.

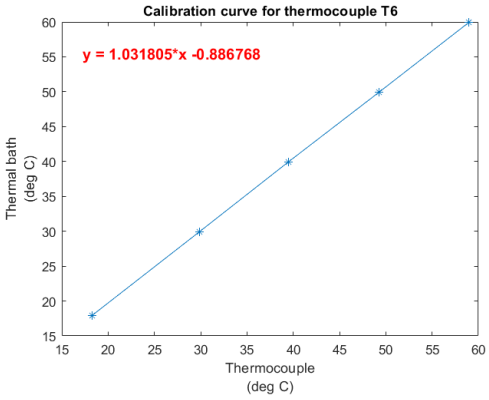

(f) Calibration curve for thermocouple T6.

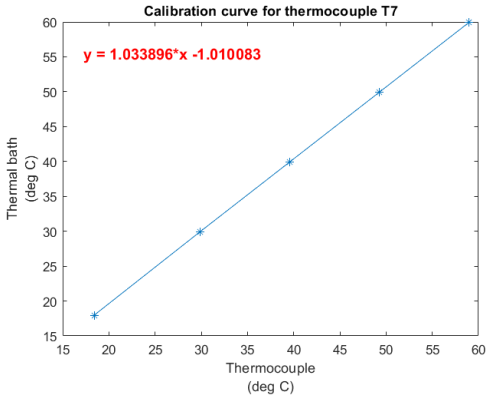

(g) Calibration curve for thermocouple T7.

Figure A.2: Calibration curves for temperature measurement.

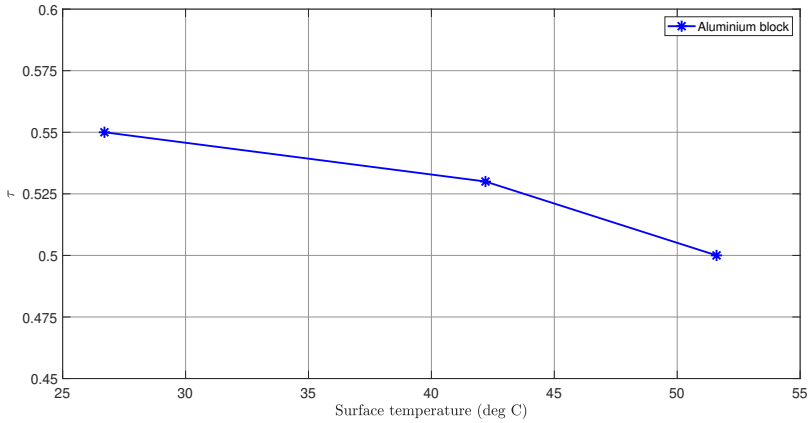

Figure A.3: Transmissivity of inspection window versus surface temperature for measurements with uniformly heated aluminium block.

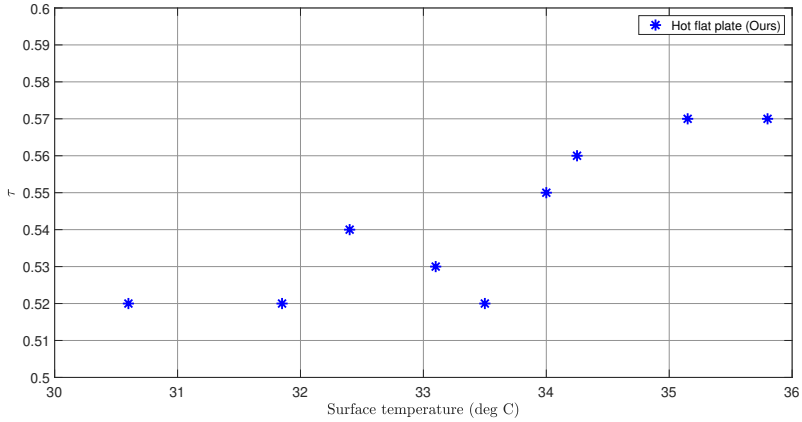

Figure A.4: Transmissivity of inspection window versus surface temperature for measurements with flat plate.

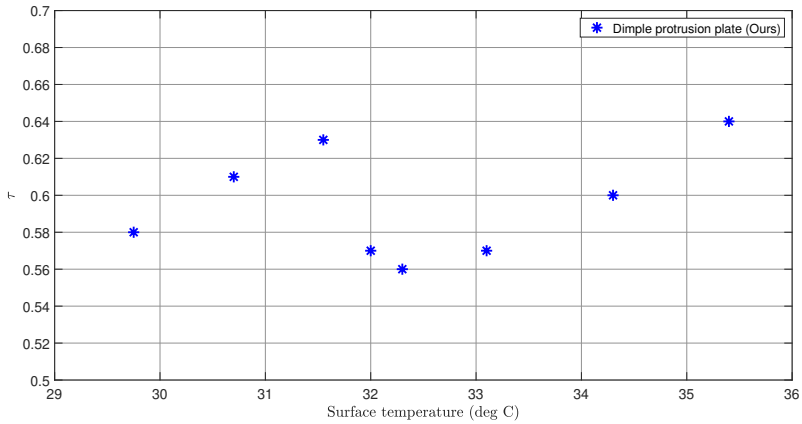

Figure A.5: Transmissivity of inspection window versus surface temperature for measurements with dimple-protrusion plate.

B

Measurement Uncertainty

The uncertainty of the instruments used for measurements can be determined at the design stage. The zero-order uncertainty is equal to 1/2 × instrument resolution. The uncertainty intervals associated with various measurements is shown in Table B.1

Table B.1: Uncertainty intervals of various measurements

Sr. No	Measurement	Instrument	Uncertainty
1	Dimension of the channel	Meter scale	±0.5 mm
2	Height of channel	Vernier caliper	±0.05 mm
3	Temperature measurements	K-type thermocouples	±0.05 °C
4	Surface temperature measurements (NETD)	IR camera	±30 mK
5	Pressure drop across the channel	Omega Pressure sensors	±0.1 Pa

Figliola and Beasley [2001] states that propagation of error into derived quantities can be calculated as follows:

$$\delta y = \left(\frac{dy}{dx}\right)_{x=\overline{x}} \delta x \tag{B.1}$$

Moffat [1988] states that whenever the equation describing the result is a pure product form then the relative uncertainty can be found as follows:

$$R = {X_1}^a {X_2}^b {X_3}^c \ldots\ldots {X_M}^m \tag{B.2}$$

then,

$$\frac{\delta R}{R} = \left[\left(a\frac{\delta X_1}{X_1}\right)^2 + \left(b\frac{\delta X_2}{X_2}\right)^2 + \ldots\ldots\ldots + \left(m\frac{\delta X_M}{X_M}\right)^2\right]^{\frac{1}{2}} \tag{B.3}$$

Using the above equation, the relative uncertainty for various parameters is calculated as shown below.

1. Uncertainty in Area of plate

$$A_p = W \times L$$

$$\frac{\delta A_p}{A_p} = \left[\left(\frac{\delta L}{L}\right)^2 + \left(\frac{\delta W}{W}\right)^2\right]^{\frac{1}{2}}$$

2. Uncertainty in Area of flow

$$A_f = W \times H$$

$$\frac{\delta A_f}{A_f} = \left[\left(\frac{\delta H}{H}\right)^2 + \left(\frac{\delta W}{W}\right)^2\right]^{\frac{1}{2}}$$

3. Uncertainty in measurement of Hydraulic diameter

$$D_h = \frac{4W \times H}{W + H}$$

$$\frac{\delta D_h}{D_h} = \frac{1}{W + H}\left[\left(W\frac{\delta H}{H}\right)^2 + \left(H\frac{\delta W}{W}\right)^2\right]^{\frac{1}{2}}$$

4. Uncertainty in density measurement

$$\rho = \frac{P_a}{R \times T_o}$$

$$\frac{\delta \rho}{\rho} = \left[\left(\frac{\delta P_a}{P_a}\right)^2 + \left(\frac{\delta T_o}{T_o}\right)^2\right]^{\frac{1}{2}}$$

5. Uncertainty in mass flow rate measurement

$$m = \rho A_f u$$

$$\frac{\delta m}{m} = \left[\left(\frac{\delta \rho}{\rho}\right)^2 + \left(\frac{\delta A_f}{A_f}\right)^2 + \left(\frac{\delta u}{u}\right)^2\right]^{\frac{1}{2}}$$

6. Uncertainty in Reynolds number

$$Re = \frac{u \times D_h}{\nu}$$

$$\frac{\delta Re}{Re} = \left[\left(\frac{\delta u}{u}\right)^2 + \left(\frac{\delta D_h}{D_h}\right)^2 + \left(\frac{\delta \nu}{\nu}\right)^2\right]^{\frac{1}{2}}$$

7. Uncertainty in useful heat loss

$$Q_u = mC_p(T_{in} - T_{out}) = mC_p\Delta T$$

$$\delta\Delta T = [(\delta T)^2 + (\delta T)^2]^{\frac{1}{2}}$$

$$\frac{\delta Q_u}{Q_u} = \left[\left(\frac{\delta m}{m}\right)^2 + \left(\frac{\delta C_p}{C_p}\right)^2 + \left(\frac{\delta \Delta T}{\Delta T}\right)^2\right]^{\frac{1}{2}}$$

8. Uncertainty in heat transfer coefficient

$$h = \frac{Q_u}{2A_p \times (T_p - T_b)} = \frac{Q_u}{2A_p \times \Delta T_b}$$

$$\delta T_b = [(\delta T)^2 + (\delta T)^2]^{\frac{1}{2}}$$

$$\delta\Delta T_b = [(\delta T_b)^2 + (\delta T_p)^2]^{\frac{1}{2}}$$

$$\frac{\delta h}{h} = \left[\left(\frac{\delta Q_u}{Q_u}\right)^2 + \left(\frac{\delta A_p}{A_p}\right)^2 + \left(\frac{\delta \Delta T_b}{\Delta T_b}\right)^2\right]^{\frac{1}{2}}$$

9. Uncertainty in Nusselt number

$$Nu = \frac{h \times D_h}{k_a}$$

$$\frac{\delta Nu}{Nu} = \left[\left(\frac{\delta h}{h}\right)^2 + \left(\frac{\delta D_h}{D_h}\right)^2 + \left(\frac{\delta k_a}{k_a}\right)^2\right]^{\frac{1}{2}}$$

10. Uncertainty in Stanton number

$$Nu = \frac{Nu}{Re \times Pr}$$

$$\frac{\delta St}{St} = \left[\left(\frac{\delta Nu}{Nu}\right)^2 + \left(\frac{\delta Re}{Re}\right)^2 + \left(\frac{\delta Pr}{Pr}\right)^2\right]^{\frac{1}{2}}$$

11. Uncertainty in Darcy friction factor

$$f = \frac{\Delta p}{L} \times \frac{2D_h}{\rho u^2}$$

$$\delta\Delta p = [(\delta p)^2 + (\delta p)^2]^{\frac{1}{2}}$$

$$\frac{\delta f}{f} = \left[\left(\frac{\delta \Delta p}{p_1 - p_2}\right)^2 + \left(\frac{\delta D_h}{D_h}\right)^2 + \left(\frac{\delta L}{L}\right)^2 + \left(\frac{\delta \rho}{\rho}\right)^2 + \left(2\frac{\delta u}{u}\right)^2\right]^{\frac{1}{2}}$$

12. Uncertainty in Volume goodness factor

$$VGF = \frac{St}{f^{1/3}}$$

$$\frac{\delta VGF}{VGF} = \left[\left(\frac{\delta St}{St}\right)^2 + \left(\frac{-1 \times \delta f}{3f}\right)^2\right]^{\frac{1}{2}}$$

13. Uncertainty in Performance factor

$$PF = \frac{VGF}{VGF_0}$$

$$\frac{\delta VGF}{VGF} = \left[\left(\frac{\delta VGF}{VGF}\right)^2 + \left(\frac{\delta VGF_0}{VGF_0}\right)^2\right]^{\frac{1}{2}}$$